



UNIVERSITÀ DEGLI STUDI DI TRIESTE

XXIX CICLO DEL DOTTORATO DI RICERCA IN
NANOTECNOLOGIE

**STRUCTURAL AND ELECTRONIC
COUPLING OF ORGANIC
HETEROAROMATIC MOLECULES ON
INORGANIC SURFACES OF OXIDES**

settore scientifico-disciplinare: FIS/03 – Fisica della Materia

DOTTORANDO

Marcos Domínguez Rivera

COORDINATOR

Prof.ssa Lucia Pasquato

SUPERVISORE

Prof. Alberto Morgante

TUTORE

Dr. Luca Floreano

ANNO ACCADEMICO 2015/2016

CONTENTS

1. INTRODUCTION	1
2. EXPERIMENTAL TECHNIQUES	3
2.1. THE ULTRA-HIGH VACUUM.....	3
2.2. SCANNING TUNNELING MICROSCOPY	4
2.3. ELECTRON SPECTROSCOPIES	10
2.3.1. Photoemission: XPS and UPS	10
2.3.2. Absorption: NEXAFS.....	13
2.4. ELECTRON DIFFRACTION	16
2.4.1. Reflection High Energy Electron Diffraction	18
3. EXPERIMENTAL APPARATUS	21
3.1. THE ALOISA BEAMLINE	21
3.1.1. ALOISA experimental chamber	23
3.1.2. HASPES experimental chamber	27
3.2. CFM EXPERIMENTAL CHAMBER	29
3.3. SUPPORTO DI SUPERFICI EXPERIMENTAL CHAMBER.....	31
4. HYBRID INTERFACES OF HETEROAROMATIC MOLECULES ON TiO₂.....	35
4.1. INTRODUCTION	35
4.2. THE RUTILE TITANIUM DIOXIDE SURFACE	36
4.2.1. Surface preparation and characterization.....	39
4.3. TETRAPYRROLE MACROCYCLES: PORPHYRINS	45
4.3.1. 2H-TPP Spectroscopy characterization: XPS	47
4.3.2. 2H-TPP Near-edge X-ray photoemission spectroscopy.....	53
4.3.2.1. COMPARISON WITH 2H-OEP and 2H-tbTPP	57
4.3.3. 2H-TPP film structure determination: STM and RHEED.....	60
4.3.3.1. COMPARISON WITH 2H-tbTPP	67
4.3.4. 2H-TPP theoretical approach.....	69
4.3.4.1. Low coverage films	69
4.3.4.2. High coverage films	75

4.4.	PHthalocyanines: 2H-PC AND TiO-PC	81
4.4.1.	<i>Spectroscopy characterization: XPS and NEXAFS</i>	<i>82</i>
4.4.2.	<i>Film structure determination: STM.....</i>	<i>86</i>
4.4.3.	<i>2H-Pc theoretical approach</i>	<i>88</i>
5.	INTERMOLECULAR COUPLING. DONOR/ACCEPTOR STACKING ON TiO₂	90
5.1.	FULLERENE: C60.....	90
5.2.	TiO-PC, 2H-TBTPP AND C60 INTERACTION	92
6.	CONCLUSIONS	100

1. INTRODUCTION

Organic heteroaromatic compounds present nice capabilities that are attractive from the scientific and technological points of view. The transporting charge and the photoabsorption properties in the solar radiation spectrum make them interesting for organic electronics and photovoltaics applications. Several advantages over the inorganic competitors must be taken in count: i) device fabrication is less complex due to the low vacuum and temperature deposition or solution processing, with direct benefits into production costs and environmental impact, ii) functionality would be enhanced due to their chemical tailoring potential, through molecular functionalization, iii) the weak intermolecular interaction due to van der Waals forces makes organic films flexible and compatible with plastic substrates, opening the way towards the fabrication of soft, large-area bio-sensors.

The study of the structural, electronic and chemical properties of adsorbed organic films becomes an open issue, where most modern surface studies tried to understand and control these properties mainly focusing on the interaction of organics with single crystal surfaces of coinage metals (Au, Ag, Cu), since they can be easily obtained and prepared in ultra high vacuum (UHV).

A limited amount of publications deal with the interface between organics and dielectric single crystals, in confrontation with its relevance for organic devices: i) thanks to the photoexcitation behaviour of dye molecules known as sensitizers, attached to a nanoporous or nanospheres of titanium dioxide, organic dye-sensitized solar cells collect sunlight and convert it into electricity, ii) the reversible switching of conformational or electronic configurations on insulating layers, like the isomerization [1] in molecules or the charging of individual atoms [2], are nice base to perform nanomemories with high information storage capabilities, iii) the architecture of field effect transistors [3], that are the pillar of amplifiers and logic circuits, consists of a charge transporting material in contact with an insulator where the voltage to switch on the current flow is applied.

From the basic surface science point of view, semiconductors and insulators presents a depleted electronic density region between valence bands and conduction bands allowing the molecular states to remain unperturbed by the interaction with electrons populating the half-filled bands of metals at the Fermi edge. Scanning probe techniques on these systems produced images of molecular orbitals with sub-molecular resolution, and details of the intramolecular distribution of charge [4]. In addition, the nanomanipulation with the scanning probe tip, enabled the observation of orbital hybridization when metal-organic bond is formed [5], opening the in situ real-time study of on-surface chemistry catalysed by active substrate.

Despite the evolution on the field, a lot of difficulties like poor self-assembly properties for bi-dimensional and three-dimensional structures, and the impurities on the surface, must be overhaul to the real technological application in the design and production of systematic and reliable nanodevices.

The present work is focused in the self-assembly and electronic and chemical properties of different organic units, and the influence and interaction with the rutile-TiO₂ surface along the (110) plane, that is one of the most famous transition metal oxides. The work is divided in two parts: i) the study of chemical and structural properties of heteroaromatic molecules: phthalocyanine (2H-Pc), tetraphenyl porphyrin (2H-TPP), tert-butyl tetraphenyl porphyrin (2H-tbTPP) and octaethyl porphyrin (2H-OEP) through microscopic and spectroscopic characterization and theoretic simulations, anchoring their main chemical reactions under the rutile-TiO₂(110) presence as source of atoms and as catalytic surface, focusing into 2H-TPP that has demonstrated an exceptionally high thermal stability for its monolayer that presents phase transitions, keeping the coordination of the macrocycle central pocket to the oxygen atoms beneath throughout the self-metalation and flattening reactions and ii) the interface study of some of them (i.e. 2H-tbTPP and TiO-Pc) taking advantage of their donor behaviour with acceptor units (fullerene C₆₀), by means of valence band measurements to understand the influence of the molecule-molecule and molecule-substrate interactions in the molecular HOMOs and their capabilities as another way to tune the energy levels alignment.

2. EXPERIMENTAL TECHNIQUES

2.1. THE ULTRA-HIGH VACUUM

The ultra-high vacuum (UHV) is defined as the vacuum region below 10^{-9} mbar, and it is the only that allow to prepare and keep atomically clean surfaces long enough to carry out experiments on them.

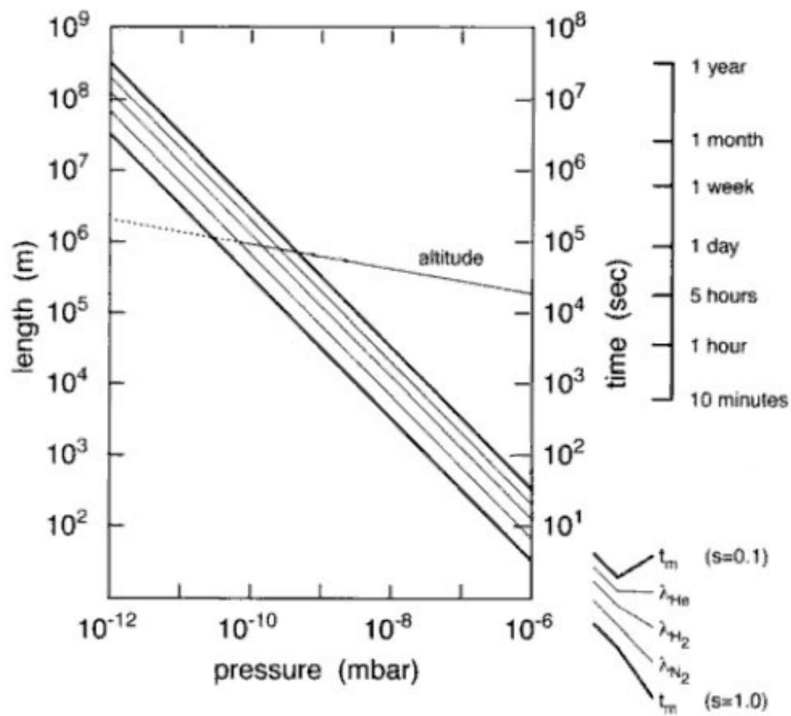


Fig. 2.1. Relationship between gas pressure, surface contamination and mean free path lengths. In the right down corner is shown the legend for time contamination (t_m), using sticking factor 0.1 and 1, where λ_x is the mean free path of the standard X molecules [6].

The experiments and techniques performed during this thesis were done under UHV conditions. Techniques based on particle beams, require UHV that allows them to travel undisturbed to interact with the sample surface, or the detector [6].

The kinetic theory of gases gives us an estimate contamination time, depending on molecular weight, temperature, pressure and sticking coefficient (probability that one molecule arrived on the surface remains on it, $0 \leq s \leq 1$). As simplified rule, at typical UHV pressure 10^{-10} mbar if every gas molecule hitting the surface sticks on it, the complete coverage will take place in 10^5 secs, enough time to perform an experiment in clean conditions. In the Fig 2.1. is shown the relationship between gas pressure, surface contamination time and mean free path length.

The chamber is constructed mainly with a μ -metal shielded stainless steel, glass and ceramic for electrical contact and insulation. It needs to remain leak free, for this reason the flanges present steel knife edges in both sides (chamber and flange) that compress softer copper gaskets, creating a leak proof seal [6].

The UHV regime is reached by multistage pumping systems. First a scroll pump gives us a background pressure of 10^{-2} mbar inside the chamber, then a turbo molecular pump gives us 10^{-6} mbar pressure. At this pressure, the air and water adsorbed on the walls of the chamber act as virtual leak, slowly desorbing. To improve the vacuum to reach 10^{-10} mbar and so on, the chamber is heated to 150°C for at least 24 hours, removing the adsorbates over the walls that can be at this point easily pumped out. Once cooled down the chamber reaches 10^{-10} mbar and still needs to be pumped to keep UHV conditions. The residual gas remaining as this point is basically composed by H_2O , N_2 , CO .

2.2. SCANNING TUNNELING MICROSCOPY

The Scanning probe methods' principle of operation is conceptually simple: a metallic sharp

tip is placed in the proximity of a sample surface, close enough to generate a finite tunneling conductance. If a voltage V is applied, an electron tunneling current I is generated and once amplified can be easily measured. This current depends exponentially on the distance between sample and tip. The tip is at this point made to scan the surface, applying a feedback loop to keep tunneling current or height constant.

The Scanning Tunneling Microscope (STM) samples in real space the atomic geometry through the local density of states. Fig. 2.2. shows the schematic STM's operation principle.

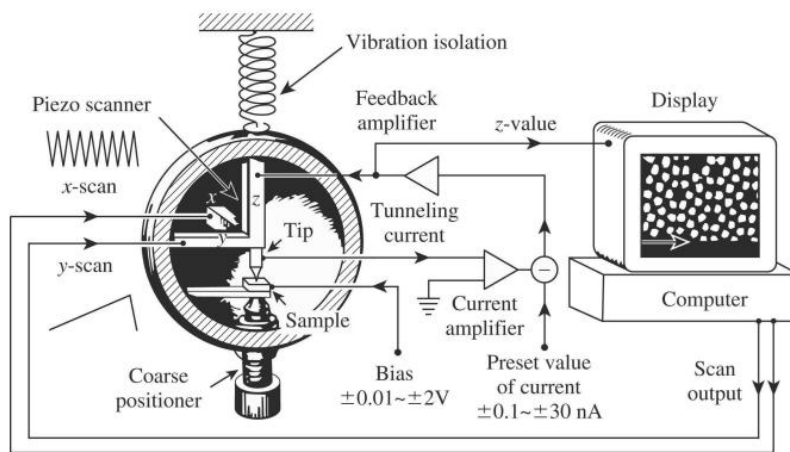


Fig. 2.2. Schematic diagram of an STM, showing the feedback controlled piezo scanning the tip over the surface, and the z values obtained as a topographical image on the computer [7].

Since the development ascribed to Binnig et al. [8], it has become a well-established technique, improving the vibration isolation of the probe and the sample, from the primitive version of superconducting levitation system to the actual suspension springs and damping mechanisms using eddy currents; the scan speed with an appropriate sinusoidal signal applied to the tip movement, can achieve the range of hundreds of frames per second.

The STM is a quantum mechanics empirical demonstration by itself: an incident particle upon

a potential barrier higher than the particle's kinetic energy has no zero-probability of traversing the forbidden region and reappearing on the other barrier side. This is the phenomenon of tunneling and is a consequence of the wavelike properties of electrons, and its wave function $\psi(z)$ satisfies the Schrödinger equation

$$-\frac{\hbar}{2m} \frac{d^2}{dz^2} \psi(z) + U(z)\psi(z) = E\psi(z) \quad (2.1)$$

where m is the electron mass, z and E are its position and energy. Considering the case of a piecewise-constant potential U in the classical allowed region $E > U$, generates a plane wave solution

$$\psi(z) = \psi(0)e^{\pm i\kappa z} \quad (2.2)$$

where κ is the wave vector

$$\kappa = \frac{\sqrt{2m(E-U)}}{\hbar} \quad (2.3)$$

The electron moves with constant momentum $p_z = \hbar\kappa = \sqrt{2m(E-U)}$. However there is a solution to eq. 2.2. in the $E < U$ region

$$\psi(z) = \psi(0)e^{-\kappa z} \quad (2.4)$$

where the decaying

$$\kappa = \frac{\sqrt{2m(U-E)}}{\hbar} \quad (2.5)$$

The electron then has a finite probability proportional to $|\psi(0)|^2 e^{-2\kappa z}$ of penetrating the barrier and being detected at a point z .

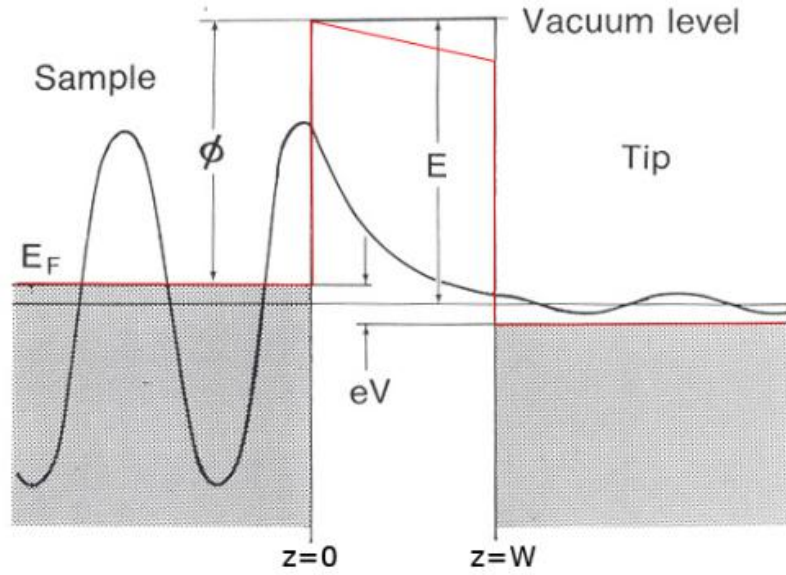


Fig. 2.3. One-dimensional sample-vacuum-tip square barrier model as semi-infinite pieces of free-electron metal. The height of the barrier is the work function ϕ and the width of the barrier W represents the distance to the tip. [8].

Applying it to the Fig. 2.3. model, the electrons at the sample's Fermi level, that is the upper limit of the occupied states in a metal, have an energy E_f and the energy required to extract one electron to the vacuum level and escape with zero kinetic energy is the work function ϕ

that depends on the materials and the crystallographic orientation of the surface. When a voltage V is applied, the electrons in the sample lying between E_f and $E_f - eV$ have a finite probability to tunneling the tip. If the voltage is smaller $eV \ll \phi$, the energy levels of the tunneling electrons are very close to E_f , and the probability ω of an electron in the state ψ_n occupying the n th sample state to tunnel to the tip surface ($z = W$) is

$$\omega \propto |\psi_n(0)|^2 e^{-2\kappa W} \quad (2.6)$$

considering $\psi_n(0)$ the wave function goes the n th sample state at the surface ($z = 0$) and κ the decay constant of a sample state near the Fermi level in the barrier region

$$\kappa = \frac{\sqrt{2m\phi}}{\hbar} \quad (2.7)$$

As long as the condition of the tip is stable in time, the electron flow is stationary. Then the tunneling current is proportional to the sample density of electronic states inside the energy interval eV below the Fermi energy. We can write

$$I \propto \sum_{E_n=E_f-eV}^{E_f} |\psi_n(0)|^2 e^{-2\kappa W} \quad (2.8)$$

If the voltage is small enough, then we can represent eq. 2.8. in terms of the local density of states (LDOS), corresponding to the number of electrons per unit volume per unit energy at a given point in space and at a given energy, at the Fermi level of the sample surface

$$I \propto V \rho_S(0, E_f) e^{-2\kappa W} \quad (2.9)$$

and that value of the surface LDOS near the Fermi is an indicator of the surface conductivity (metallic or insulating).

A more accurate treatment of tunneling junction was given by Bardeen in 1961 [9], starting from two free subsystems (tip and sample) and calculating the tunneling current from the overlap of their wave functions using time-dependent first-order perturbation theory [10]. On this way, the tunneling current can be obtained by summing all the states in the interval eV involved in the process

$$I = \frac{4\pi e}{\hbar} \int_{-\infty}^{+\infty} \left[f\left(E_f + \frac{1}{2}eV + \epsilon\right) - f\left(E_f - \frac{1}{2}eV + \epsilon\right) \right] \times \\ \rho_S\left(E_f + \frac{1}{2}eV + \epsilon\right) \rho_T\left(E_f - \frac{1}{2}eV + \epsilon\right) |M(\epsilon)|^2 d\epsilon \quad (2.10)$$

at low temperature, i.e. when limit $k_B T \ll eV$, the Fermi distribution $f(E)$ can be approximated by a step function

$$I = \frac{4\pi e}{\hbar} \int_{-\frac{1}{2}eV}^{+\frac{1}{2}eV} \rho_S\left(E_f + \frac{1}{2}eV + \epsilon\right) \rho_T\left(E_f - \frac{1}{2}eV + \epsilon\right) |M(\epsilon)|^2 d\epsilon \quad (2.11)$$

demonstrating that an STM image is a convolution of sample and tip DOS, and as consequence of Bardeen's theory the reciprocity principle: if the electronic state of the tip and the sample are interchanged, the image should remain the same.

2.3. ELECTRON SPECTROSCOPIES

The phenomena in which an energetic enough, incident light ejects electrons from matter is known as the photoelectric effect and was discovered by Hertz (1887) and theorized by Einstein (1905): an electron in a state with binding energy E_B absorbs a photon with energy $h\nu$ and can get over the material's work function ϕ , escaping with a kinetic energy E_{Kin}

$$E_{Kin} = h\nu - E_B - \phi \quad (2.12)$$

Due to the attractiveness of the electrons as experimental probes (i.e. with electrostatic fields, the electrons' energy and momentum can be easily focused and analysed; electrons are easy to count and vanish after being detected; as shown in the Fig. 2.4., the escape depth of electrons is small enough to keep the surface sensitivity of the techniques; electrons provide direct information on the electronic structure of the matter, etc.), this effect is the base of many spectroscopic techniques, in particular for this thesis: x-ray (XPS) and ultraviolet (UPS) photoemission spectroscopy to study occupied electronic states by direct photoionization [11] and near-edge x-ray absorption fine structure (NEXAFS) that gives information on unoccupied states in the presence of a core hole [12].

2.3.1. PHOTOEMISSION: XPS AND UPS

Depending on where are the electrons in the atom they can display core- (i.e. closed to the atom cores) or valence- (i.e. delocalized to participate to interatomic bounds) like character.

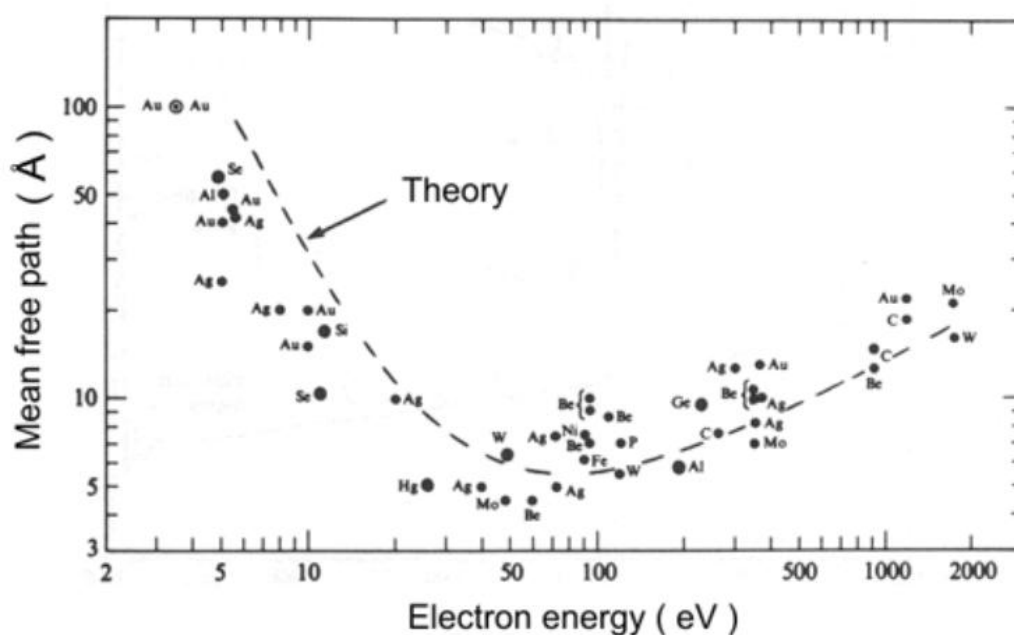


Fig 2.4. Mean free path of electrons in solids as a function of their energy and its theoretical approach. [12]

In XPS, usually *soft* x-ray photons ($h\nu = 100 \text{ eV} - 1 \text{ keV}$) are used to probe the sample. This energy is enough to eject the electrons most tightly bound from the core-levels, showing in the energy vs. photoemission intensity spectra sharp peaks at well define energies corresponding with the electron binding energies that are characteristic of each atomic species, giving us an XPS fingerprint to identify the elements present in the sample. Several factors influence the exact location of core level peaks, that are usually classified as *initial state* effects, originating from the environment before the excitation, i.e. the changes in the chemical environment can lead to variations in the position of the core level, known as *chemical shifts*. Its origin could be due to either the formation of chemical bonds that are involved in the electron transfer and change the charge density of the atom or the electron charge transfer to a given atom that enhances the electron screening of the nucleus, decreasing the electron binding energy, or the electron charge transfer from a given atom that weakens the screening, thus increasing the electron binding energies [12]. *Final state*

effects take place after the creation of a core hole, (i.e. core-hole screening effects in conductors and polarization of dielectrics).

The peaks shape also gives us information about the lifetime of the core hole state created in the photoemission process. Its Lorentzian width is intrinsic and its Gaussian broadening is due to the resolution limit of the analyser. Moreover, the integrated peak area gives us information about the amount of deposited material or the surface reactions' rate.

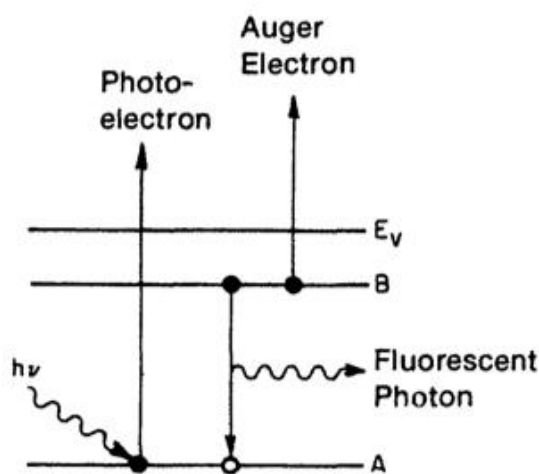


Fig. 2.5. Diagram of a photon absorption process resulting in a photoelectron and a core-hole. The hole is filled by an electron radiatively by the emission of a fluorescent photon or non-radiatively by emission of an Auger electron [13].

In UPS, ultraviolet light ($h\nu = 10 \text{ eV} - 100 \text{ eV}$) is used to probe states near the Fermi energy, as the substrates' valence band, surface states and low energy occupied molecular orbitals (HOMO) of adsorbates.

2.3.2. ABSORPTION: NEXAFS

In the previous techniques, we described the photoemission by direct excitation of the photo-emitted electrons from the occupied states of matter to the vacuum level, but a photo-emitted electron encounters empty states before the continuum states above the vacuum level. The near-edge X-ray absorption fine structure (NEXAFS), is used to probe these unoccupied states. In this two-stages process, when the photon energy matches the energy between a core state and an empty state, the electron is excited to this unoccupied state, generation a hole, and the consequent decay would be by the emission of a photon (florescence) or the emission of an Auger electron (Fig. 2.5.). So, if the sample is irradiated with monochromatic x-rays of variable energy around an ionization edge, the subsequent relaxation of the system either by Auger or florescence channels is going to be a measure of the absorption cross-section. The detection of electrons is more common for organic thin films due to its larger surface sensitivity, and the strong predominance of Auger emission over florescence for light elements ($Z < 35$) [13].

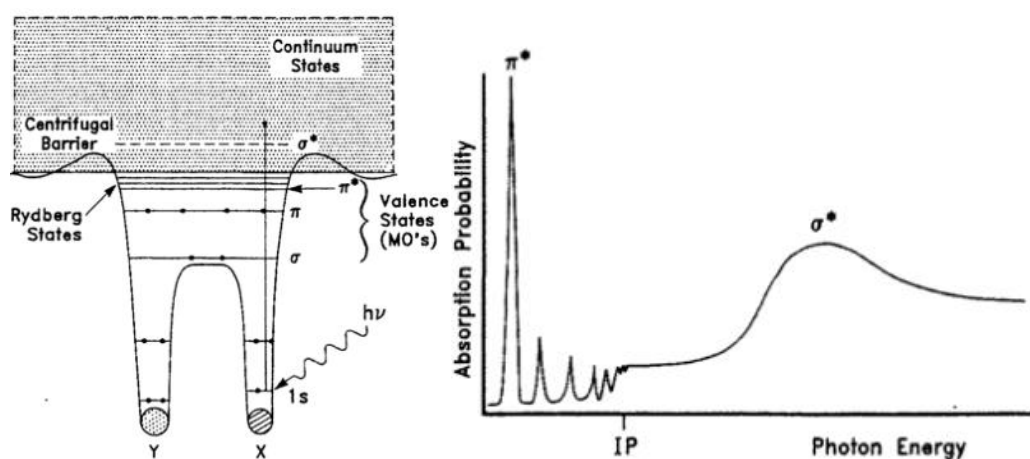


Fig. 2.6. Schematic potential (left) and K-shell spectra (right) of diatomic molecules. [13]

In Fig. 2.6. for diatomic molecules, there are in addition to the empty atomic states, empty molecular orbitals (MOs) that are named as σ and π symmetries and with * if they are unfilled. In π -conjugated molecules the lower unoccupied molecular orbital is usually a π^* -orbital, with the σ^* -orbitals at higher energies. These states are usually above the vacuum level in neutral molecules but pulled below by electron-hole Coulomb interaction in the ionized molecules. The NEXAFS doesn't ionize the atom or molecule, but creates a hole and excites an electron that will therefore interact.

The natural linewidth of the resonances (as dictated by the corresponding lifetime) is broadened by the instrumental resolution which eventually swears the splitting of resonances due to the molecular vibrational states. Since σ^* orbitals are found above the vacuum level and at higher photon energies they can overlap with the continuum that provides a larger number of decay channels, so no resonances are expected and they have lower life-time and appear significantly broader.

NEXAFS spectra can give us information about the structural organization of an overlayer, its magnetic properties and bonding. Bond lengths in a molecule can be estimated analysing the energy position of σ^* resonances, and since this length is sensitive with the oxidation state of an atom, chemical reaction can be monitored. Moreover, the chemisorption of a molecule is often accompanied by a charge transfer between molecule and substrate, that quenches the NEXAFS peak associated with the lowest unoccupied molecular orbital (LUMO) or generates a new state close to it.

The intensity of an absorption is proportional to the probability that an electron in an initial state, occupies a higher energy final state when the sample is illuminated by a photon beam. This transition probability is described by the Fermi's golden rule [14] that links the resonance intensity I to the matrix element

$$I \propto |\langle f | \vec{e} \cdot \vec{p} | i \rangle|^2 \quad (2.13)$$

where \vec{e} is the electric field direction and \vec{p} the momentum operator. For linearly polarized light (as the produced in a synchrotron) and a $1s$ initial state, we can obtain the simple form

$$I \propto |\vec{e}\langle f|\vec{p}|i\rangle|^2 \propto \cos^2 \delta \quad (2.14)$$

with δ the angle between the electric field vector and the direction of the final state orbital, that presents a maximum when the electric field direction is aligned along a direction of maximum electron density. This polarization dependence of the resonances intensity allows the molecular orientation determination. Because of the spatial localization of the $1s$ electrons, only p-like final states from the atoms whose absorption is probed by the selected photon energy will appear in the spectrum. This is known as the dipole selection rule.

Considering a final π^* -plane molecular orbital, linearly polarized photon beam and the two-fold symmetry of the (110) face of rutile-TiO₂ the ratio between the intensity of a $1s \rightarrow \pi^*$ transition in S- and P-polarized light becomes

$$I_s/I_p = 1 - \cos^2 \theta \cos^2 \gamma - \sin^2 \theta \sin^2 \gamma \quad (2.15)$$

and due to the small incident angle θ about 4°

$$I_s/I_p = \tan^2 \gamma \quad (2.16)$$

The resonances seen at the NEXAFS spectra for large molecules belongs to different submolecular units as the building block principle approaches. If these subunits may adapt

different azimuthal orientations respect to the molecular plane, the tilt angle must be calculated with a formula for threefold or higher substrate symmetry

$$I_s/I_p = \frac{3}{2} \tan^2 \gamma \quad (2.17)$$

2.4. ELECTRON DIFFRACTION

As shown in Fig. 2.7. when any incident beam (i.e. photons, ions, electrons, neutrons or protons) with a wavelength comparable to the periodical spacing between the structures of interest is scattered from these structure planes it produces an interference. This interference will be constructive if the path difference between two waves is equal to the multiple of their wavelength, so if the planes distance is d , and the beam collides with an angle θ the interference will be constructive if

$$n\lambda = 2d \sin \theta \quad (2.18)$$

this equation is known as the Bragg's law.

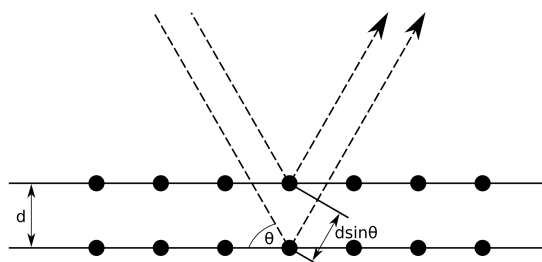


Fig. 2.7. Waves reflecting from two parallel lattice planes.

If we describe the waves by the incident (k_i) and diffracted (k_o) vectors, assuming the process is elastic, the lengths of the wave vectors are the same during all the process

$$|k_i| = |k_o| = \frac{2\pi}{\lambda} \quad (2.19)$$

By taking in account the trigonometric relation between these vectors, we can finally obtain, that for a constructive interference the difference between the wave vectors of the incident and diffracted waves must be equal to the vector from the reciprocal lattice $|G|$

$$|G| = \frac{2\pi}{d} \quad (2.20)$$

or in vector form as Laue interpreted it

$$k_i - k_o = G \quad (2.21)$$

It's a more general interpretation that doesn't requires the Bragg assumptions that reflection is mirror-like and coming from the parallel planes of atoms.

In a geometric approach the Ewald sphere shown in Fig. 2.8. is a construction that combines the wavelength of the incident and diffracted waves, the diffraction angle for a specific reflection and the reciprocal lattice of the sample. Considering the sphere radius

$$r = \frac{2\pi}{\lambda} = |k| \quad (2.22)$$

when the sphere intercepts with a reciprocal lattice point, the Laue condition is satisfied, giving a constructive interference of the diffracted waves.

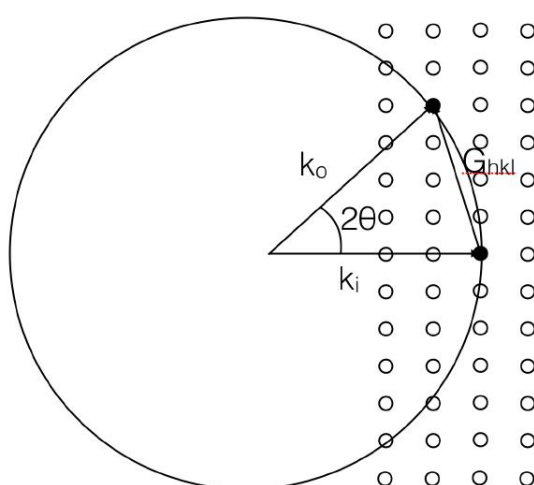


Fig. 2.8. Ewald sphere where the dark spots are the reciprocal lattice points that fulfil the Laue condition.

2.4.1. REFLECTION HIGH ENERGY ELECTRON DIFFRACTION

If we do reflection with high energy electrons beam (5 – 100keV) (i.e. provide large elastic scattering cross-section for forward-scattered electrons), we need to keep the penetration depth of the technique small using a reflection geometry in which the beam is incident at very grazing angle (1-4°) as seen on Fig. 2.9., thus remaining a surface sensitive technique. Only the electrons which interact with the most superficial layers experiment elastic collisions originating a diffraction pattern. Other electrons suffer inelastic scattering transforming the parallel and monokinetic beam in a divergent, quasi-monokinetic beam and

increasing the probed depth. The scattering of these electrons give rise to the lines of Kikuchi if the material is well-crystallized (i.e. single crystal).

In the case of LEED, the relation between a diffraction pattern and the reciprocal lattice is easily understood, but RHEED patterns are not so intuitive. This technique enable us to know the intensity distributions along the reciprocal lattice rods only changing the crystal orientation. In the LEED, the acceleration voltage is changed to record the intensity distributions along them, but this change in the wavelength gives change in the magnitude of the strong dynamical effect essentially accompanied with LEED, making difficult to analyse the surface structure.

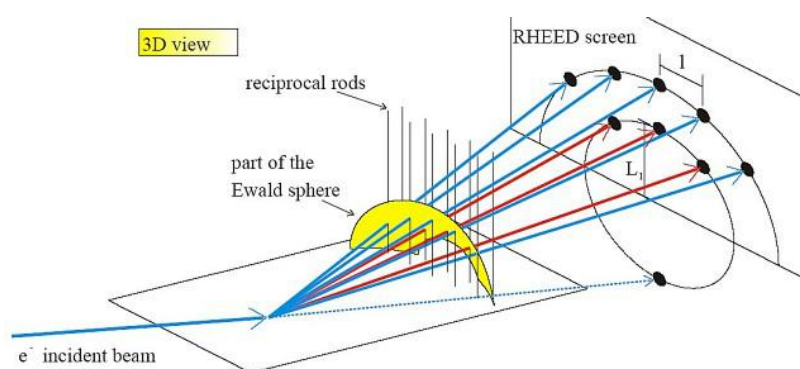


Fig. 2.9 3D view of the Ewald sphere for reflection high energy electron diffraction [15].

Theoretically, the intersection of streaks with the Ewald Sphere should form points. However, the radius of this one is too large for the energy considered during RHEED measurements compared with the reverse of the interatomic distances, doing the Ewald sphere to cross along many lattice rods but only few near grazing exit angles, and looking the surface as a continuous along the incidence direction (without diffraction), thus detecting only the perpendicular periodicities (i.e. usually we only see (00) and $(\bar{1}0)$ components) that combined with the dispersion angle and energy of the electrons beam and the imperfect

crystalline quality of the surface, make the diffraction pattern to appear also in the form of streaks.

This peculiar geometry allows to perform measurements during growth of surface films, been possible to monitor the layer-by-layer growth of epitaxial films by monitoring the oscillations in intensity of the diffracted beams in the RHEED pattern, doing possible to control the growth rate in Molecular Beam Epitaxy (MBE) [16].

The RHEED pattern also can be used to measure periodicities transverse to the incidence plane measuring the separation between streaks [17, 18], and comparing the heights of the peaks (i.e. Intensity) in the rocking curves to extract detailed atomic spacing by quantitative analysis [19], that doesn't concern to this thesis.

3. EXPERIMENTAL APPARATUS

3.1. THE ALOISA BEAMLINE

ALOISA (Advanced Line for Overlayer, Interface and Surface Analysis) is a multitask beamline for surface science experiments, it is designed to work in a wide spectral range (100-8000eV) and hosts three experimental chambers; the main setup ALOISA dedicated to X-Ray diffraction and spectroscopy experiments, the end-station ANCHOR (AmiNo –Carboxyl Hetero-Organic aRchitectures) equipped with an independent monochromatic X-ray source and a helium lamp to perform off-line experiments and the end-station HASPES for helium atom scattering that can perform real time He diffraction and XPS.

ELETTRA Synchrotron is a 3rd generation light source, operating a storage ring energy of 2 or 2.4GeV in top-up mode, and providing photon beams in the range of 10-30000eV with high spectral brilliance.

The ALOISA photon beam is produced by a U7.2 wiggler/undulator insertion device (ID) of the ELETTRA Synchrotron, that consists in a spatially periodic magnetic field produced by two alternative oriented magnets superimposed in a face-to-face configuration and separated by a user-tuneable gap that allows two operation modes. When the gap is large in comparison with the distance of two magnet series (~40-80mm) with low critical beam energies (130-2000eV) the ID operates in the undulator regime. When the gap is lower (~20mm), i.e. the magnetic field is stronger, the amplitude of the sinusoidal path increases and the ID operates in the wiggler regime. In the Fig. 3.1. we can see the intensity of the photon beam as a function of the photon energy for different ID gap values.

The planar undulator is composed by an array of 19 periods of permanent magnets 80.36 mm long, with a total length of 1527 mm. The light once produced is selected in angle by a pinhole

and collimated by a paraboloidal mirror in sagittal configuration. This parallel light beam can impinge on two different dispersion devices; a Plane Mirror/Grating Monochromator (PMGM), for the 120-2000 EV range, and a Si(111) channel-cut crystal for the 2.8-8 keV range with a photon flux at the substrate of about 1×10^{12} in the low energy range and $1-2 \times 10^{11}$ in the higher range. The spot size in the centre of the experimental chamber is about $40 \times 200 \mu\text{m}^2$ with an energy resolving power ($E/\Delta E$) between 2000 and 7500. The light is linearly polarized in the plane of the electron beam orbit.

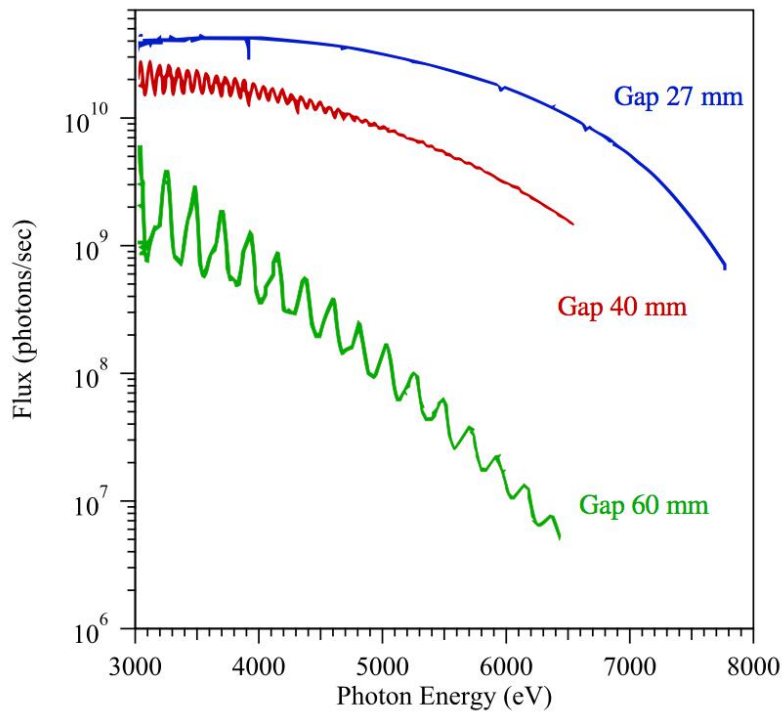


Fig. 3.1. Intensity of the photon beam at the exit of the ALOISA wiggler/undulator ID as a function of the gap. [20]

As shown in the Fig. 3.2. the light is collected from the entry pinhole by a paraboloidal mirror (Parabol-1) and collimated to the dispersing system. The monochromatic beam is focused at the exit slits (ES) by a second paraboloidal mirror (Parabol-2). This exit divergent beam is

finally focused on the sample at the centre of the chamber by a toroidal mirror (cylindrical). Even if the system hasn't an entrance slit, the optics are used in the sagittal focusing configuration to minimize the aberrations in the dispersive plane. All the optics have a gold coating to increase the reflectivity of X-rays thanks to its large critical angle, and they are operated grazing incidence with a deflection angle of 1° .

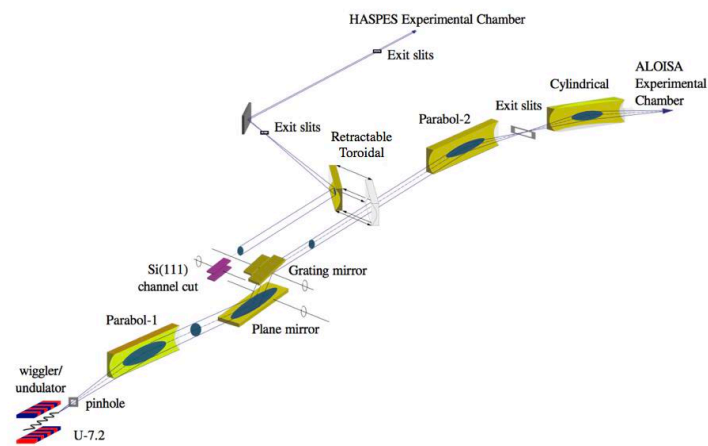


Fig. 3.2. Optical system of the ALOISA beamline and HASPES branchline.

The beam is switched to the HASPES branchline by a third mirror (Toroidal shape) and due to the large distance of the chamber (14 m), no additional refocusing mirrors are used.

The optical elements movement is automatized via TCP-IP connection as a service of the Beamline Control System (BCS), developed by ELETTRA technical team.

3.1.1. ALOISA EXPERIMENTAL CHAMBER

The ALOISA experimental chamber, shown in the Fig. 3.3., is composed by two differentiated parts: a hemispherical chamber, dedicated to the sample preparation (called preparation

chamber) and a cylindrical chamber hosting the electron analysers and photon detectors (called main chamber).

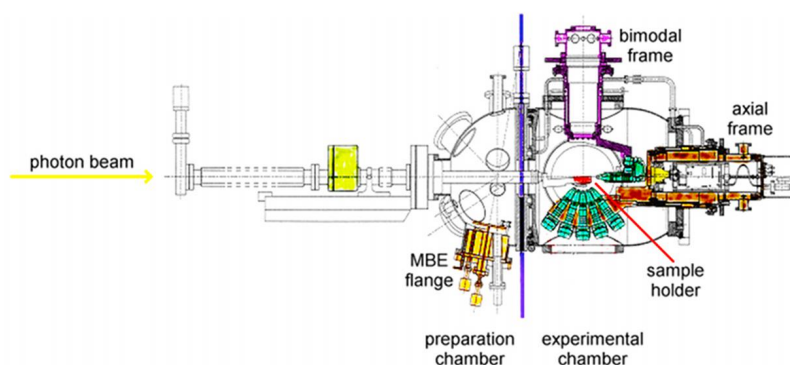


Fig. 3.3. Cross-section of the ALOISA chamber. The main experimental apparatus are highlighted.

The preparation and main chamber are coupled with large bronze ball bearing and sliding O-rings' system that allows the complete rotation of the main chamber (including the detectors) around the synchrotron radiation (SR) beam axis.

The system is pumped by two pumping stages that maintain a constant base pressure of 10^{-11} mbar inside the main chamber.

The preparation chamber is equipped with a molecular beam epitaxy (MBE) cryopanel that hosts four evaporation cells, usually Knudsen cells or electron bombardment evaporators, and can calibrate the deposition flux with two microbalances. There are also gas lines that allows high purity gases to be bled into the chamber. The ion gun for the Ar^+ bombardment allows an ion energy of 3 keV and an emission current over $25\mu\text{A}$. A Reflection High Energy Electron Diffraction (RHEED) apparatus with electron energy of 15 keV and able to impinge on the surface at grazing angle is available for checking the surface in-situ during the deposition. In the preparation chamber, there is also the sample transfer system and fast

entry-lock allowing quick sample exchange. There is also a quadrupole mass spectrometer (QMS) to check the evaporation and the cleanliness of our vacuum and for leak test porpoise.

Rotating element	Rotation axis	Extension	Resolution
Experimental chamber	SR beam	$\pm 120^\circ$	0.00015°
Axial frame	SR beam	$\pm 120^\circ$	0.0002°
Bi-modal frame	Perpendicular to SR beam	$\pm 100^\circ$	0.0002°
Sample Holder	SR beam	$-90^\circ; +185^\circ$	0.001°
Sample Holder	Grazing angle	$-2^\circ; +15^\circ$	0.001°
Sample Holder	Surface normal	$\pm 95^\circ$	0.001°

Table. 3.1. Rotations of the ALOISA main chamber and manipulator holder.

Inside the main chamber the detectors are mounted in two independent frames. The axial one is hosted at the end of the main chamber and rotates around the SR beam axis independently with the chamber and the sample. It hosts five 35mm electron analysers with low resolution of 500 meV and acceptance angle of 5° . They are mainly dedicated to Auger Photoelectron Coincidence Spectroscopy (APECS). The bimodal frame is mounted on the side of the cylindrical main chamber and rotates perpendicular to the SR beam and around the SR beam together with the main chamber. It hosts a 66 mm hemispherical electron analyser with 2° of angular acceptance for X-ray Photoemission (XPS) and photoelectron diffraction (PED). There is also one energy resolved photodiode for measuring the total current for X-ray diffraction (XRD) and reflectivity (XRR). The bimodal frame additional hosts two energy resolved (Peltier-cooled) photodiodes operating in single-photon counting mode for X-ray diffraction. There is also a phosphorous plate with a CCD camera mounted on the axial frame

for 2D X-ray reflectivity measurements that allows the alignment of the beam and the sample.

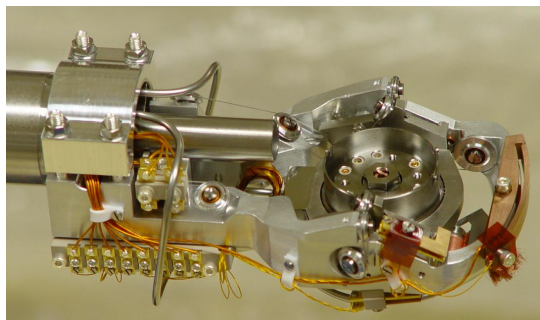


Fig. 3.4. ALOISA manipulator arm without sample holder. The light flux arrives from the cylindrical hose on the left side over the sample that faces up inside the circular holder.

A wide-angle acceptance channeltron is mounted on the axis of the bimodal frame, used to measure the partial electron yield in NEXAFS experiments. This channeltron is mounted in front of its apex with an additional grid to repel the low-energy multiple-scattered electrons, acting as a high-pass filter, where only higher-energy Auger electrons contribute to the partial-yield signal.

The manipulator shown in Fig. 3.4. that hosts the sample has six-degree of freedom and is mounted horizontally into the preparation chamber and can translate the sample between preparation and main chamber. Since the SR beam passes through the whole manipulator arm and impinges at grazing incidence into the sample surface, three rotations with some limitations as shown in Fig 3.5. are allowed; around the synchrotron beam (R1) to select the surface orientation with respect to the polarization, the grazing angle (R3) and the azimuthal orientation for the surface symmetry axis (R2). Also, the displacement in the three axes (X, Y, Z) are allowed. Their limits are exhibit in the Table 3.1.

The sample holder is a variable temperature system equipped with two tungsten filaments and electrical insulation, which enables applying high voltage the electron bombardment heating of the sample over 1100K, and a gas pipeline with a cold-finger contact on the sample holder which enables the cooling down with liquid Nitrogen until 150K.

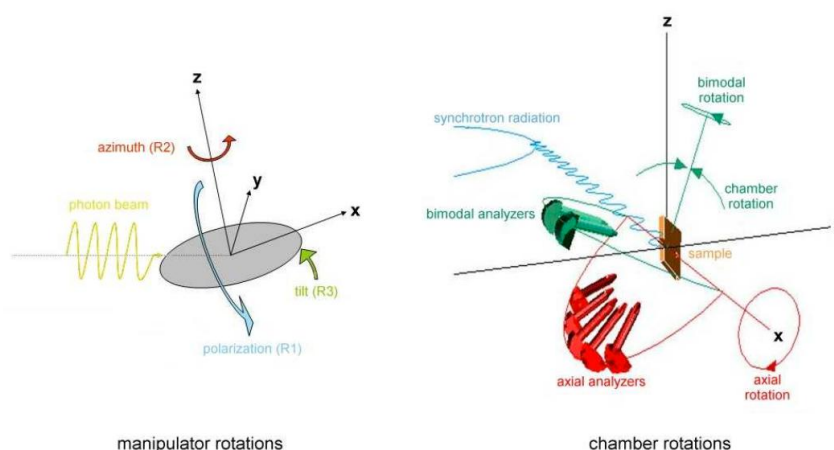


Fig. 3.5. Sketch of the angular movements available by the manipulator (left) and the experimental chamber (right).

The data acquisition and movements are automatized with a LabVIEW homemade program developed by the ALOISA team.

3.1.2. HASPES EXPERIMENTAL CHAMBER

The Helium Atom Scattering and Photoelectron Spectroscopy (HASPES) chamber is composed, as seen in Fig. 3.6., by a main upstanding cylindrical vacuum chamber, a pre-chamber with a helium atom source and a chamber for helium detection with a QMS.

HASPES take advantage of the low-energy monochromatic SR beam that enters through the He detection system coincident with the He scattered beam but in the opposite direction.

The sample holder compatible with ALOISA chamber is mounted in a vertical VG CTPO manipulator with six degrees of freedom and a high-precision movement set by harmonic drives. The system is also equipped with a thermal link to a cryostat for liquid nitrogen or liquid helium cooling and tungsten filaments, that allows a variable temperature between 100-1100K range.

The detectors angle is fixed at 110° for HAS and 55° for XPS. There are three possible sample rotations; changing the incident angle of helium atoms and SR beam (R1), changing the surface symmetry axis respect to the scattering plane (R2) and tilt rotation (R3).

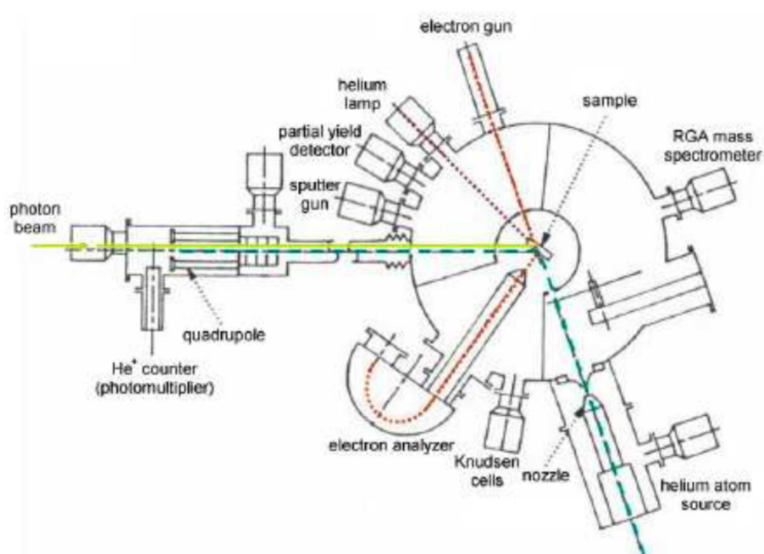


Fig. 3.6. HASPES chamber and its equipment.

The chamber displays a pumping system that controls the smooth transition for the He to pass from continuum to free-molecular flow inside a nozzle which pressure ratio between the stagnation pressure and the background pressure in the beam chamber is about 10^7 , so

no shock structures appears in the expansion region, allowing a He pressure in the stagnation chamber of 10-100 bar range to tune the flux and monochromaticity of the He beam.

This nozzle has a skimmer that defines the angular divergence of the beam and a chopper that select the pulses for inelastic scattering measurements, and another collimator to enter in the experimental chamber with a cross section of about 0.7 mm. The beam energy can be set between 18.6 and 100meV with the temperature inside the stagnation chamber.

At this point the neutral atoms are ionized by an electronic beam (the electrons have a $E_{kin} = 100\text{eV}$ that is the maximum cross-section to ionize He atoms) and filtered with a QMS with a charge to mass ratio accuracy of 0.05 e.m.u.

The supplementary equipment includes a helium lamp that provides ultraviolet radiation, a 150mm high resolution hemispherical electron analyser, an electron gun in the scattering plane that offers angularly well resolved electron detection, a channeltron at an angle of 50° for the partial electron yield detection in NEXAFS experiments, an ion gun for Ar⁺ sputtering, a cryopanel with three Knudsen evaporation cells and a fast entry lock for quick sample exchange.

3.2. CFM EXPERIMENTAL CHAMBER

The main STM experimental chamber shown in the Fig. 3.7. used during this thesis belongs to the *NanoPhysics Lab* at the “Centro de Física de Materiales” in San Sebastián, Spain, and is handled by Dr. Celia Rogero.

This chamber is composed by two parts: a cylindrical chamber dedicated to the sample preparation and the spectroscopic analysis (chamber 1), and a spherical chamber hosting the STM head and with sample’s preparation capabilities (chamber 2).

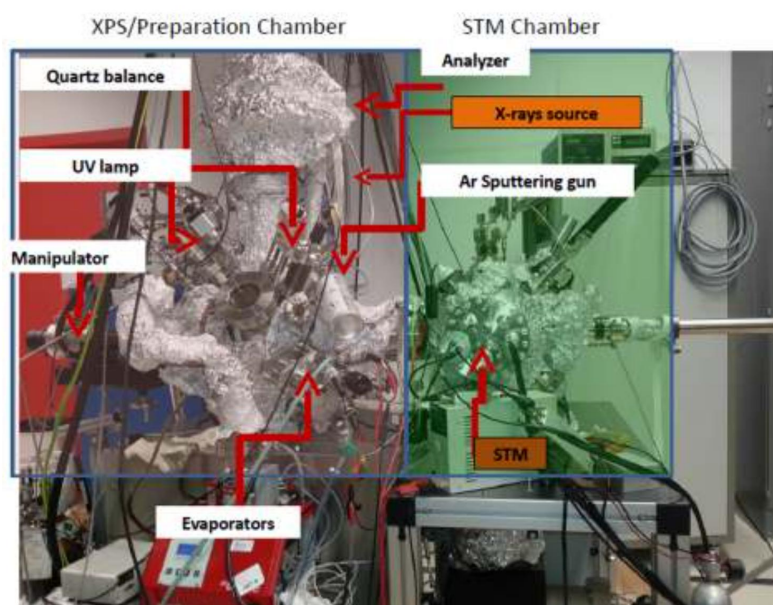


Fig. 3.7. Experimental setup for preparation and STM measurements (courtesy of C. Rogero, Nanophysics Lab, Centro de Física de Materiales, Donostia/San Sebastián, Spain).

Both chambers are communicating in vacuum by a transfer arm and separated with gate valves to preserve the vacuum cleanliness and isolation during the experiments. The vacuum reaches 10^{-10} mbar in both chambers thanks to the scroll and turbo pumping systems, and the ion pump of the chamber 1 and the getter pump of the chamber 2 during the STM operation to avoid to the maximum the mechanical noises.

The chamber 1 is equipped with: an horizontal four degrees of freedom manipulator that hosts the sample, allowing its movement in x, y, z coordinates and the axial rotation in the sample's plane, R1, and hosts a filament that allows the sample heating by electron bombardment up to 1100K; one X-ray source of Al K- α radiation, with an energy of 1486.6 eV and one He I UV lamp (21.2 eV) associated with a spherical electron energy analyser for photoemission spectroscopy; a fast entry system that allows the sample exchange in a few hours; one ion gun for sputtering the sample; a quartz microbalance to tune the molecules

deposition and a set of commercial filament-heated evaporators pointing to the centre of the chamber.

The chamber 2 hosts the commercial variable temperature STM head (SPM 150 Aarhus from SPECS Surface Nano Analysis GmbH), that includes a Liquid Nitrogen cooling system and a Zener diodes heating system, allowing to experiment in the range of 150K-400K. The SPM 150 Aarhus performs scanning tunnel microscopy in both modes constant height and constant current, and atomic force microscopy (AFM) thanks to the patented KolibriSensor®. Its noise isolation is due to a springs and Viton system that allows different levels of damping and working without disconnecting the turbo pumping system.

On this chamber there is also an Ion gun for tip cleaning and normal incidence sample sputtering; a manipulator with a filament for the sample electron bombardment; a parking system to keep samples under UHV conditions for a long period; a fast entry with a gate valve that allows the installation of an additional evaporation cell pointing to the centre of the sample during the scanning, to perform in-situ experiments; a long transfer arm to translate the sample from chamber 1 to chamber 2 and a wobble-stick to manipulate the sample plate inside the chamber.

3.3. SUPPORTO DI SUPERFICI EXPERIMENTAL CHAMBER

Due to the good STM results obtained at the “Centro de Física de Materiales”, the group decided to buy a new STM head from SPECS in collaboration with the group of the micro-nano-carbon laboratory (MNC-lab) managed by Dr. Andrea Goldoni.

After its commissioning the experimental chamber is composed by three parts as seen in Fig. 3.8.: a spherical chamber dedicated to the preparation and alignment of the sample (preparation chamber), a spherical chamber hosting mainly the STM and availability for

sample preparation in-situ (STM chamber) and a large vertical cylindrical chamber hosting a complete ARPES system for spectroscopy experiments (ARPES chamber).

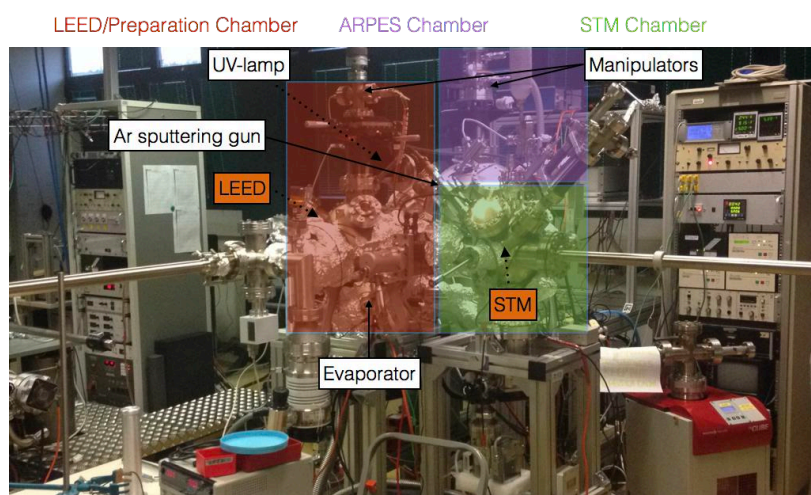


Fig. 3.8. Experimental setup for preparation, STM and ARPES measurements.

The preparation chamber is composed by a fast entry to insert and extract new samples in a few hours that includes a long transfer arm to shift the sample from the preparation chamber to the ARPES chamber, a wobble stick to manipulate the sample inside the preparation chamber, a four degrees of freedom manipulator that holds two filaments for heating and electron bombardment, a LEED (light energy electron diffraction) for alignment and detection of the symmetry of the surface with and without adsorbates, an ion gun for Ar^+ sputtering, two evaporator's entries that point directly to the centre of the chamber and the sample when it's in the manipulator, a quartz microbalance to tune the deposition mounted directly on the manipulator on the back of the sample holder.

The STM chamber holds the STM head (SPM 150 Aarhus) described in the previous chapter, an ion gun for Ar^+ sputtering to clean the tip and the sample in normal incidence if necessary, a manipulator that holds a heater composed by two filaments and electron bombardment capabilities, one wobble stick to transfer and manipulate the sample inside the chamber, one

transfer arm to move the sample from the STM chamber to the preparation chamber that, likewise the other transfer arm, includes a homemade sample holder shown in the Fig. 3.9. This sample holder smartly solves the problem with the angular limitations to transfer the sample between chambers due to the “L” configuration of the chambers.



Fig. 3.9. Sample holder for SPECS and Omicron symmetries sample plates that allows the sample plane translation in seven circular positions (from -135° to 135° by 45°).

The ARPES chamber is supplied by a VUV5k series UV source from GAMMADATA. This photon source is based on a He plasma generated by electron cyclotron resonance (ECR) technique. A microwave generator is coupled to a discharge cavity inside a magnetic field tuned to the microwave frequency to find the ECR condition, providing concentrated radiation at 21, 23 eV (He I) and 41 eV (He II). The flux density is comparable with the obtained from a beamline undulator and about 500 times higher than the one from other conventional discharge VUV sources. Its stability and bandwidth (1 meV) make it excellent for studies and measurements that require high intensity, long measurement times and high resolution (i.e. gas phase). It's supplied with a monochromator that achieved complete separation of He α and He β . The manipulator that holds the sample is a Johnsen Ultravac model 3000, with an XY stage, a Z drive of 0.01 mm of precision and a polar rotation of 360 degrees attached to a cryostat from Advanced Research Systems (ARS) with a base temperature lower than 9 K and incredible cooling power (10 W @ 77 K). The electron spectrometer is a SCIENTA R3000 that provides fast band mapping, a lens acceptance angle of $\pm 15^\circ$ and angular resolved range of $\pm 10^\circ$ and variable dispersion. The energy resolution is 3.0 meV, the angular resolution is of 0.1° for a

0.1 mm emission spot and the kinetic energy range is from 0.5 to 1500 eV with a pass energy between 2 and 200 eV. A QMS completes the chamber.

The entire system is pumped in several stages mainly by scroll, and diaphragm pump for the pre-pumping and turbo pumps to reach and preserve the UHV in the 10^{-10} mbar range.

4. HYBRID INTERFACES OF HETEROAROMATIC MOLECULES ON TiO_2

4.1. INTRODUCTION

Tetrapyrrole macrocycles, specifically the porphyrins, are very stable and versatile molecules. Due to their capabilities, they are involved in the main life processes and present large number of technological applications [21] from photocatalysis to dye-sensitized solar cells [22]. Basically, their rigid core becomes a building block unit that allows the molecular assembling in complex architectures, by tuning the strength and nature of the adsorption interaction and molecule-molecule interaction by functionalization with peripheral ligands. Free base porphyrins or metalloporphyrins can be used, where the optical, electronic, magnetic and catalytic properties depend on the specific metallic nucleus. This tuneable assembling over solid surfaces allows the designing and fabrication of hybrid surfaces engineered at the nanoscale [23]. By assembling porphyrins at solid surfaces, it's possible to design and fabricate hybrid systems with properties engineered at the nanoscale. On surface modification of metal-free porphyrins, is a viable route to achieve chemical and structural control of molecular overlayers.

Thanks to the Rutile- $\text{TiO}_2(110)$ characteristics, adsorbed on such as its large and anisotropic surface corrugation, where molecular films are expected to grow with the macrocycle parallel to the substrate, [24] and the possibility of charge injection into the oxide, [25] this substrate becomes a suitable playground for the characterization of archetypal organic dye molecules.

4.2. THE RUTILE TITANIUM DIOXIDE SURFACE

The interest on surface science of metal oxides has been rapidly increasing in the last years, since oxide surfaces have a lot of applications and are present in most metals that are oxidized immediately under ambient conditions. Due to its properties, titanium dioxide, TiO_2 , has a lot of technological applications as a photocatalyst, as gas sensor, as white pigment, as a corrosion-protective coating, in ceramics, in varistors, as optical coating, and in solar cells to produce hydrogen and electric energy.

In nature, the titanium dioxide is a polymorph and presents three crystal structures: Anatase, Rutile and Brookite, being from the scientific and technological point of view the Anatase and Rutile structures the most interesting ones. They are semiconductors with energy gap ~ 3 eV [26], that matches the gap of many light-harvesting compounds. Applying synthetic chemistry these compounds known as organic dyes that are photosensitive can be functionalized with anchoring groups to attach to TiO_2 surfaces, that added to the capabilities of TiO_2 as electron acceptor to be growth in transparent nanostructures with large surface to volume ratio, is fundamental in one of the most extended applications, dye-sensitized solar cells [27]. These prototypal dye-sensitized solar cells are composed by a mixture of mostly Anatase that favours the efficiency and minority Rutile crystals. The average surface energy of an equilibrium-shape crystal for Anatase is less than for rutile [28], that is why nanoscopic particles are less stable in rutile phase. In other hand, the photocatalyst activity of the chemically active faces as Anatase-(101) or Rutile-(110) could be induced with ultraviolet light, converting toxic compounds and molecules into basic constituents [29]. In its stoichiometric form the titanium dioxide can be use as gate layer in transistors due to its high dielectric constant. At the nanoscale, the high surface corrugation of Rutile-(110) could be exploited as a template for the growth of the organic molecule layers in an organized structure increasing their electron mobility.

Since large and pure rutile crystals are commercially available with the desired facet, and the (110) surface is the most stable face, the rutile-(110) can be considered an archetypal metal oxide surface to model the absorption of organic molecules.

Bulk rutile-TiO₂ as shown in the Fig 4.1. has a body-centred tetragonal unit cell with the Ti atoms at the body-centre and corner positions in each one. Each Ti atom, with formal charge +4, is coordinated to six O ions with formal charge -2 at the vertices of a distorted octahedron. At the same time, each O atom is coordinated with three Ti atoms with all the O-Ti bonds lying in one plane.

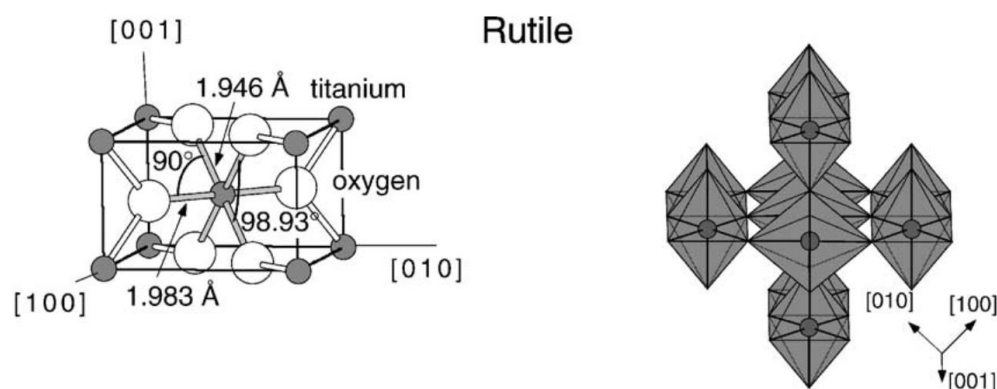


Fig. 4.1. Bulk structure of Rutile. The tetragonal bulk unit cell of Rutile has the dimensions $a = b = 4.587\text{\AA}$, $c = 2.953\text{\AA}$. Slightly distorted octahedra are the basic building units. The bond lengths and angles of the octahedrally coordinated Ti atoms are indicated and the stacking of the octahedral in both structures is shown on the right image [30].

The unreconstructed (110) surface is a simple truncation across the (110) plane as shown in Fig 4.2. and the one with lowest formation energy [30]. Two kinds of Ti atoms are present on the surface along the $[1\bar{1}0]$ where six-fold coordinated Ti atoms alternate with five-fold coordinated atoms with one dangling bond perpendicular to the surface. Two kind of O atoms are created as well. The so-called “bridging O atoms” forming rows parallel to the

[001] direction of O atoms two-fold coordinated protruding approximately 1.2 Å and rows of three-fold coordinated atoms lying in the plane of the Ti atoms and connecting the six-fold and five-fold coordinated Ti atoms' rows. The dangling bonds of the bridging O ions are compensated by the five-fold Ti ones, that according with the autocompensation criterion explains the surface stability [31].

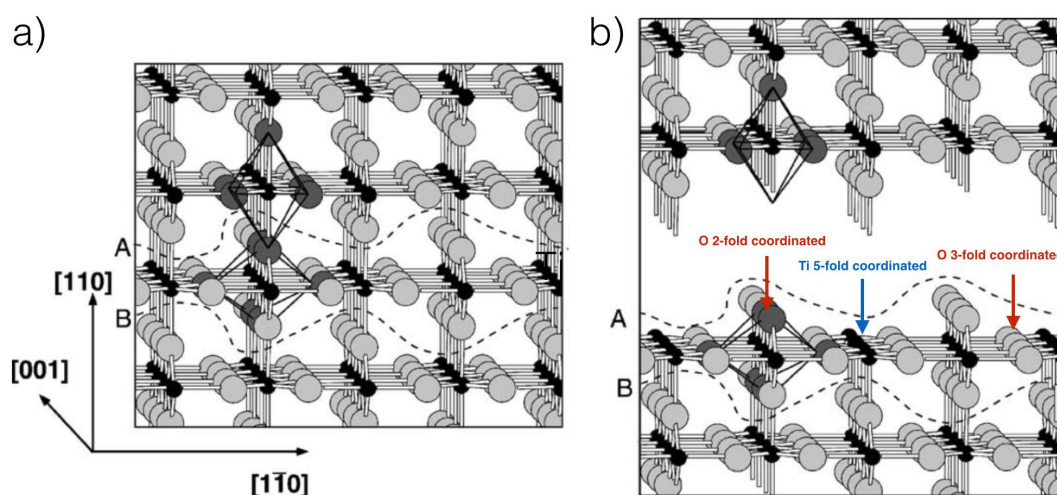


Fig. 4.2. a) Ball-and-stick model of the Rutile crystal structure emphasizing two distorted octahedrons that compose the unit cell. A and B lines surround a charge neutral repeat unit without dipole momentum perpendicular to the [001] direction. b) The crystal is truncated along line A and the resulting (110) surfaces are stable and the experimental evidence for the (1x1) surface reconstruction. [30]

Only minor relaxations occur mainly perpendicular to the surface [32] with an outward relaxation relative to the bulk position of the bridging O rows (~ 0.2 Å) and an inward displacement of the five-fold Ti (~ 0.1 Å) in the hollows. The resultant surface unit cell is characterized by a rectangular unit cell measuring 2.959×6.495 Å along the high-symmetry directions [001] and $[1\bar{1}0]$ respectively.

4.2.1. SURFACE PREPARATION AND CHARACTERIZATION

In our experiments, we have used several samples of rutile TiO₂(110) from Mateck with thickness ranging about 1mm. The preparation procedure to get a clean surface under UHV conditions is composed by two steps that can be repeated until getting the desired surface; 20 minutes of grazing angle Ar⁺ sputtering at typically 1.0 keV ion energy and 10⁻⁶ mbar Ar pressure depending on the chamber geometry and the distance and focus between the ion gun and the sample surface and an annealing cycle by electron bombardment to restore the (1x1) structure, applying a voltage of 800V to the sample and stabilizing the emission current at 10 mA for 4 min, 20 mA for 2 min and 40 mA for 1 min, not exceeding 10⁻⁸ mbar of pressure inside the chamber.

Since the annealing temperature during the last step reaches more than 750°C, the lost oxygen makes the sample conductive enough to be probed with STM and photoelectron spectroscopies avoiding charging effects, but it also increases the defects density that may condition the molecules' adsorption. Particularly the oxygen vacancies and even a perfect surface [33] under good vacuum conditions would be exposed to residual water molecules, taking place a water-splitting reaction and converting them into hydroxyl groups due to their dissociation.

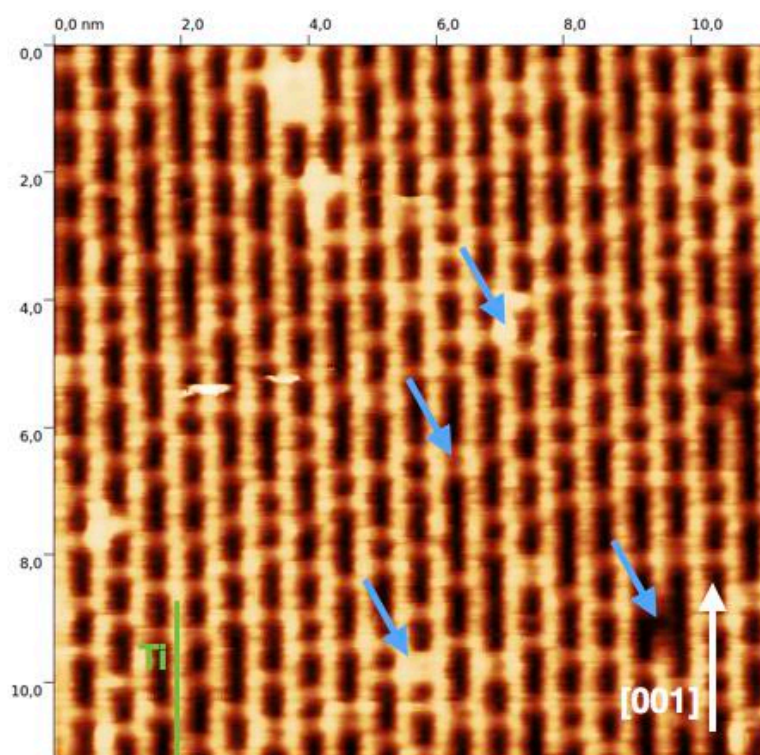


Fig. 4.3. STM constant current image of clean rutile- $\text{TiO}_2(110)$ surface with a (1×1) reconstruction. The different defects are marked by blue arrows (i.e. vacancies, hydroxyl-groups and water).

As explained with the STM we can easily probe filled and empty surface states depending if the applied bias voltage to the sample is negative or positive respectively. For $\text{TiO}_2(110)$ surface the optimal bias voltage to sample empty states are usually in the range of 1.0-1.5 V, and low tunneling current values (80-100 pA). This empty states electronic picture of a stoichiometric surface with a Ti-O in a perfect 1:2 ratio shows two features: dark and bright rows. The consensus is that the dark rows are the bridging O ions while the bright rows correspond to the five-fold Ti ions [34], considering that the large density of states in the unfilled band spatially confined on the five-fold Ti ions prevail over the surface topography and defects, oxygen vacancies and hydroxyl groups are easily recognizable in an empty-state STM image, as shown in Fig 4.3. The oxygen vacancies appear as scattered bright “bridges”,

occupying one bridging O site and connecting two five-fold Ti rows; OH groups instead share the same appearance and position but the relative height is approximately double.



Fig. 4.4. Colour centres associated with bulk defects formed upon reduction of the titanium dioxide single crystals cause a change in colour. a) Single crystal reoxidized in air at 1450 K, b) 1h 10min at 1350 K and c) 4h 55min at 1450 K. [30]

As seen in the Fig. 4.4. pristine TiO₂ crystal display a faint transparent yellow colour which exchanges to dark transparent blue and finally into a reflective, metallic-like appearance, the more the crystal is heated in UHV conditions. The reason is the progressive reduction of the material, due the lower energy barrier for their thermal desorption of the bridging O ions. Each bridging O lost generates two excess electrons that must go into the conduction band, the bottom of which is formed by Ti 3d states that are rather localized [35], changing the formal oxidation state from Ti⁺⁴ to Ti⁺³ with two consequences shown in Fig 4.5.; a shift in the 2p core level binding energy of the Ti atoms, and the presence of a new electronic state slightly below the conduction band minimum, in the band gap region. In fact, since the excess charge in Rutile form polarons, the Ti ions reduced by this excess of electrons rise an extra 2p core level peak at lower binding energy.

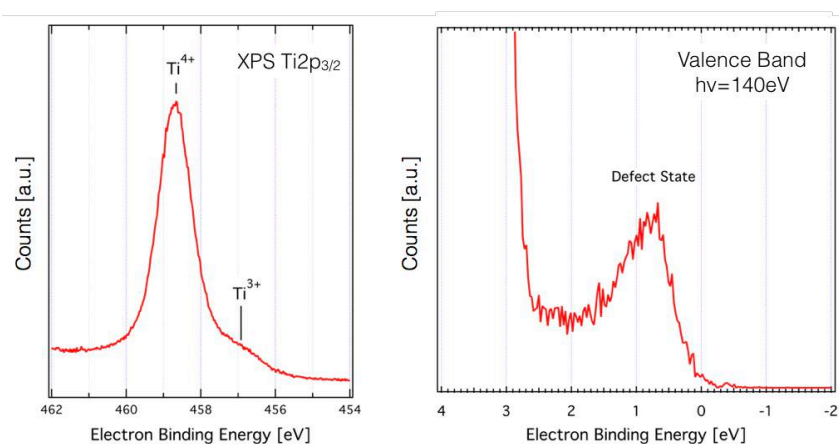


Fig 4.5. Experimental evidence of the change in oxidation state of TiO_2 upon removal of O atoms. (Right) $Ti\ 2p_{3/2}$ core level photoemission shows a shoulder corresponding to Ti^{3+} . (Left) Band gap region where new electronic state at $\sim 0.9\text{ eV}$ below the Fermi level is seen.

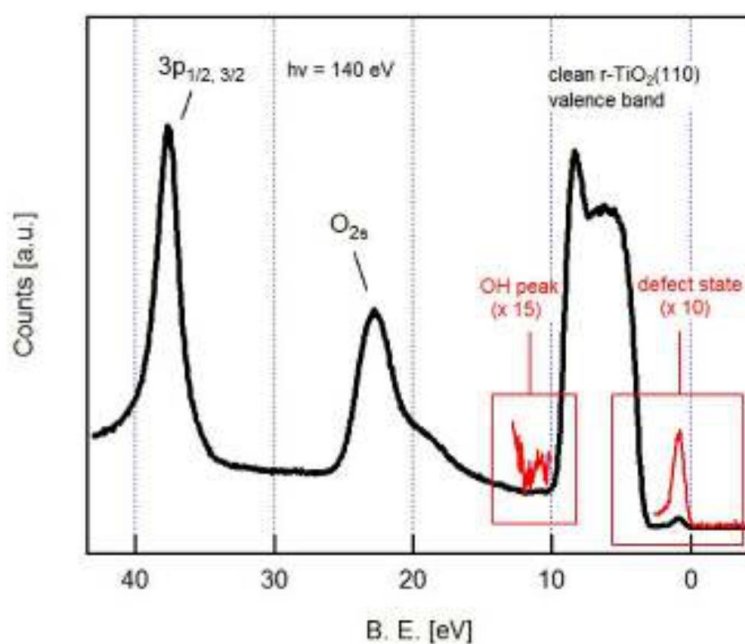


Fig. 4.6. XPS valence band spectra of rutile- $TiO_2(110)\ 1\times 1$. Two features associated with the hydroxyl presence (11 eV) and the oxygen vacancies (0.9 eV) are highlighted. The spectra is aligned according with $Ti\ 3p$ binding energy.

The OH defects can be easily recognized in the STM images, but more important in the spectroscopy spectra. The valence band spectrum presents two electronic features that can help to discriminate between oxygen vacancies and hydroxyl groups. The first peak close to the Fermi level is associated with defect electrons. As seen in the Fig. 4.6., if some charge is statically transfer to the surface by an oxygen vacancy creation or the adsorption of electron-donating molecules, the excess of electrons fill this trap state. The replacement of oxygen vacancies with hydroxyl groups takes place naturally in about 10-20 minutes as soon as the surface is cooling down. This process doesn't quench this defect peak [36], but a new feature is observed at higher binding energies. This peak can at this point be easily quenched by a calibrated exposure to O₂ at room temperature, avoiding the dissociation of O₂ molecules on the Ti 5-fold rows that would change the surface properties.

A thermal treatment in air for drying the silver paste used to attach the samples, might favour either native hydrogen diffusion from the bulk to the subsurface layers or TiO₂ hydrogenation in ambient conditions (especially at defects and sample edges) [37].

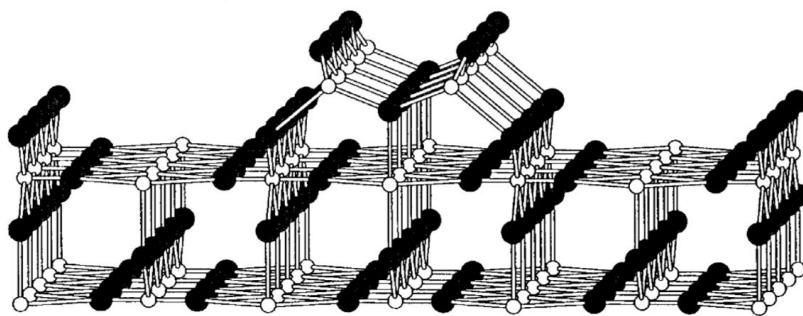


Fig. 4.7. The TiO₂ (110)-(1x2) surface "added-row model" [25].

The TiO₂ crystal can be strongly reduced by a long annealing, until the sample becomes dark blue and the oxygen vacancies density overtakes the limit of 10%. This situation causes a new

surface reconstruction (1×2), where the periodicity of the pristine TiO_2 (110) doubles across the surface rows. This reconstruction is formed by the oxygen-deficient strands that grow over the Ti five-fold rows until they form a complete (1×2) terrace [21]. The surface geometry for a simple, defect-free $\text{TiO}_2(110)-(1 \times 2)$ reconstruction is predicted by Onishi and Iwasawa [33]: Ti_2O_3 rows made of three O and two Ti ions per unit cell length along the [001] direction added on top of a Ti five-fold row each two bridging O rows in Fig 4.7..

The $\text{Ti}5f$ rows are easily identified on the (1×1) surface as bright rows as explained. In the Fig. 4.8. one can appreciate the 1×2 reconstruction, and the $\text{Ti}5f$ rows of the (1×1) surface corresponding alternatively to the middle of the (1×2) dark rows and bright paired rows, that becomes a way to distinguish the molecular alignment when molecules doesn't adsorb on the (1×2) reconstruction. The surface also presents defects that tend to aggregate into linear chains as single or cross links that are commonly observed in excessively reduced crystals [38].

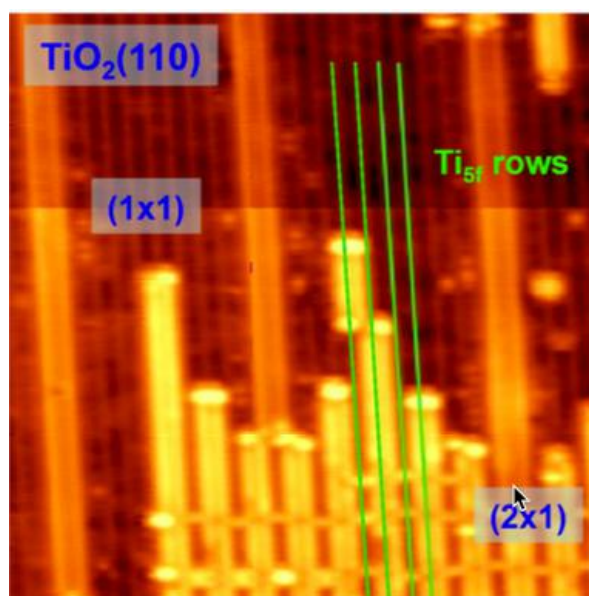


Fig. 4.8. STM detail image from clean rutile- $\text{TiO}_2(110)$ surface with (1×1) and (1×2) reconstructions. The extrapolation of the $\text{Ti}5f$ rows from the (1×1) region to the (1×2) region is shown.

4.3. TETRAPYRROLE MACROCYCLES: PORPHYRINS

One molecule has been selected as representative of porphyrins: tetraphenyl-porphyrin, 2H-TPP. Other two units, octaethyl-porphyrin, 2H-OEP and tert-butyl tetraphenyl-porphyrin, 2H-tbTPP, have been probed along the experiments, to contrast results and obtain a larger picture when necessary about the molecule-substrate interactions underneath. All of them, illustrated in the Fig. 4.9, are constituted by central sp^2 hybridized tetra-pyrrolic structure with different peripheral functionalization. Their macrocycles can incorporate almost every element of the periodic table for tuning the molecule optical properties. Their functional groups represent a nice playground with different anchoring possibilities between the molecules and the oxide surface that eventually can favoured the charge injection, the main bottleneck in the light harvesting process in dye-sensitized solar cells [39]. The 2H-TPP and 2H-tbTPP present four phenyl rings that are not co-planar with the macrocycle due to the interaction with the hydrogen atoms in the ortho- positions of the phenyl rings and the adjacent atoms at the porphyrin core. In addition, 2H-tbTPP carries additional tertiary butyl groups at the two meta- positions of each phenyl leg. The 2H-OEP presents very flexible ethyl substituents attached to the β - positions of the pyrrole moieties that doesn't induce significant adsorption-induced deformations.

From the chemical point of view, an interesting point is that porphyrins can be metalated, in situ by allowing to react with deposited metal atoms (i.e. already on the surface or directly evaporating over the molecular layer, or predeposited metal clusters) [38] but also self-metalated by incorporation of substrate metal atoms under thermal treatment [40]. This implies as third channel, the possibility of trans-metalation, where the metalloporphyrins exchange its core metal atom by a more reactive substrate atom. Self-metalation has been successfully achieved on metal substrates as Cu, Ni or Fe but much less is known about metalation reactions of tetrapyrrole macrocycles at metal oxide surfaces. Despite the expected lower flexibility of covalent bonding compared to metal bonding, there is evidence suggesting that metalation on metal oxide surfaces could be even faster than that on metal

surfaces. First, the kinetics of metalation on metal surfaces is strongly influenced by porphyrin-surface H exchange [41] where it has been demonstrated that porphyrins with various functional terminations are able to pick up H atoms from the surface already at room temperature [42]. Second, self-metalation at metal surfaces are favoured in the presence of oxygen [43, 44]. Schneider et al. demonstrated that 2H-TPP is converted into Mg-TPP when adsorbed on MgO substrates. Another interesting point is that hydrogen by itself can also be exploited in free base porphyrins to modify the local molecular conductance by selective cleavage of one pyrrolic NH bond [45], on metal surfaces to influence in the kinetics of metalation [46] as well as in metalloporphyrins to tune the chirality by selective absorption [47].

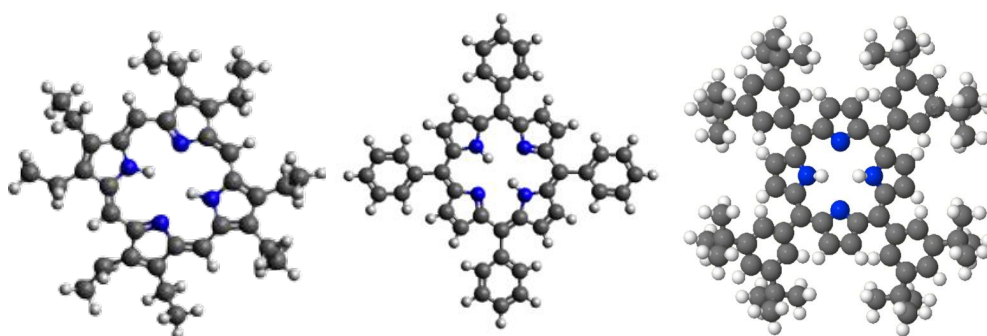


Fig. 4.9. Ball-and-Stick molecular structure of free-base octaethyl porphyrin (2H-OEP), tetraphenyl porphyrin (2H-TPP) and tert-butyl tetraphenyl porphyrin (2H-tbTPP). These molecules are characterized by their central ring of atoms known as macrocycle with two types of N atoms, iminic and pyrrolic. Gray = carbon, blue = Nitrogen, white = hydrogen.

A few investigations have been performed to study the metalation of tetrapyrrole molecules at metal oxide surfaces, like the investigation about the conversion of 2H-TPP to NiTPP at the $\text{TiO}_2(110)$ surface [38] that was reported to take place at room temperature when 2H-TPP is deposited first, whereas a temperature of 550K is required when Ni is predeposited, or the

2H-TPP metalation to MgTPP adsorbed on MgO nanocubes where the driving force of the process has been attributed to the high affinity of step and corner oxygens at the oxide surface with the hydrogens of the molecule, indicating the importance of the molecule-surface hydrogen exchange [49].

4.3.1. 2H-TPP SPECTROSCOPY CHARACTERIZATION: XPS

As starting point for the characterization of the in situ evaporated 2H-TPP molecules layer on a surface at room temperature, the ligand state of nitrogen was probed by X-ray photoemission of the N1s core level. Although metal-free porphyrins are characterized by two well defined N1s peaks of equal intensity (separation of ~ 2 eV) stemming from the molecules' pair of hydrogenated (pyrrolic) nitrogen atoms and the pair of aza- (iminic) nitrogen atoms [50], the first layer of molecules always displays a dominant component in the N1s photoemission spectra corresponding to an energy of $\sim 400.2 - 400.5$ eV as shown in the Fig. 4.10. 2H-OEP and 2H-tbTPP (Fig. 4.10) were also evaporated in the same experimental conditions on rutile-TiO₂(110)-(1x1) obtaining the same behavior.

This binding energy corresponds to the expected one for pyrrolic nitrogen. This "pyrrolization" has been reported in free-base phthalocyanine on rutile-TiO₂(110) with contradictory explanations [51]. Increasing the deposition beyond the monolayer to the thick film formation, a new peak grows at ~ 398 eV binding energy, that corresponds to the expected iminic nitrogen component, that reaches and preserves the intensity parity with the pyrrolic one after 4-5 layers. The comparison of N1s XPS between the monolayer and multilayer is also shown for all the three species as reference.

Taking into account that these three molecules are essentially different into their macrocycle height with respect to the substrate (that is increased $\sim 0.5\text{\AA}$ from one variety to the next due to simple steric arguments without considering minor relaxation effects), the absence of the iminic component cannot be simply attributed to a strong core level shift of aza-nitrogen originated by local screening.

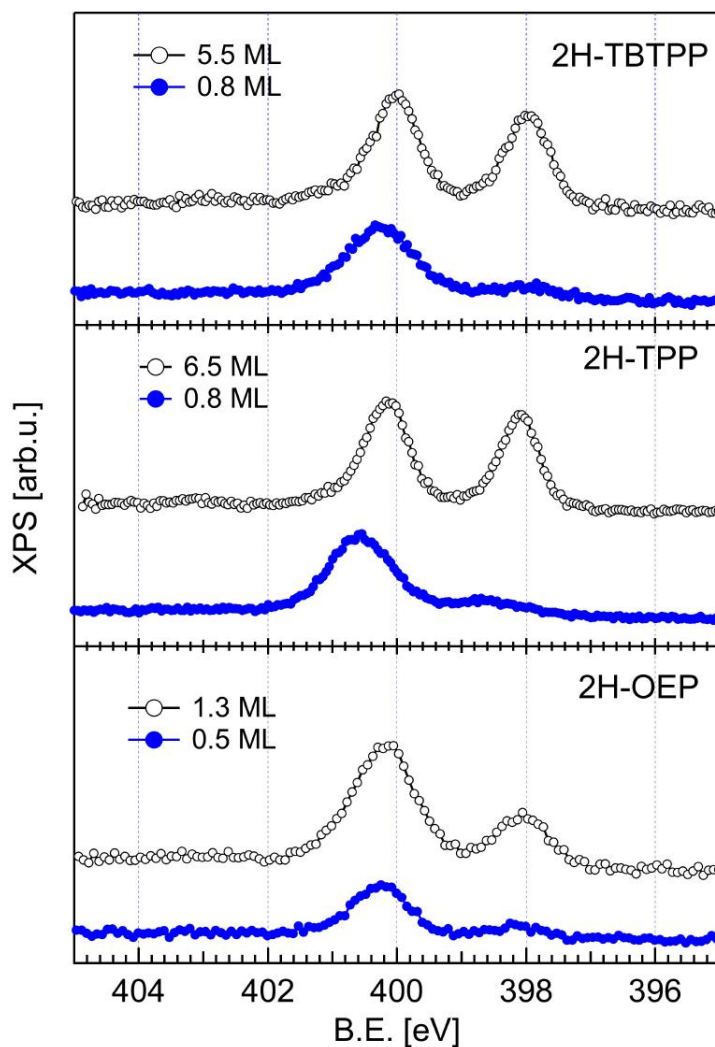


Fig. 4.10. XPS from N1s comparison between monolayer and multilayer form by deposition for 2H-OEP, 2H-TPP and 2H-tbTPP. The absence of iminic (right peak) component is clearly observed in the monolayer regime.

The 2H-TPP monolayer presents also a larger binding energy (shift of 0.2-0.3 eV) with respect to the 2H-OEP and 2H-tbTPP, which we tentatively assign to the local relaxation of the phenyl rings that fit the substrate corrugation, thanks to their angular flexibility (i.e. dihedral angle

between the phenyl plane and the macrocycle plane). When in ground state conformation of crystalline 2H-TPP, the phenyls remain tilted by 60° out of plane for steric repulsion effects between the phenyl and pyrrole C-H terminations facing one each other, whereas NEXAFS data indicate a ~30° tilt off the surface for the first layer 2H-TPP. Therefore, the only plausible remaining hypothesis is the hydrogen uptake.

The hydrogen may be present in two main coordination, as molecular hydrogen from the residual gas inside the vacuum or as atomic hydrogen from the sample. According to the literature, the hydrogen dissolution in the TiO₂ bulk would be favoured by thermal treatment, metal contaminants (acceptor nature) or electron irradiation. [52]

XPS by itself demonstrates not to be a convenient probe technique for bulk-diluted species due to its surface sensitivity (i.e. the escape depth of photoelectrons is about 5-10 Å), whereas it is a suitable probe of the small concentration of hydrogen confined into the surface by water dissociation at reduced TiO₂(110) surfaces [53] These hydrogen atoms are present in the form of hydroxyl species and they can be monitored by photoemission in the valence band energy range where a new characteristic satellite of the O 2p band surges at ~ 11 eV. [54]

In the Fig. 4.11. we show the valence band spectra of a clean but slightly hydrogenated surface with an estimated OH concentration of 4-5%), and the same surface after the deposition of a monolayer of 2H-TPP and its analogous for 2H-OEP, corresponding with the two molecules with the macrocycle close to the surface.

As can be seen, the peak associated with the OH contribution is quenched in agreement with the hypothesis of the hydrogen uptake. We must take into account that the complete hydrogenation of the nitrogen present in the first molecules layer cannot be obtained only with the hydrogen present in the surface, and more important if possible, that the hydrogenation is accomplished even on surfaces without OH contribution (i.e. free of defects surface). We are then left with the hypothesis that additional hydrogen atoms may be extracted from the subsurface layers.

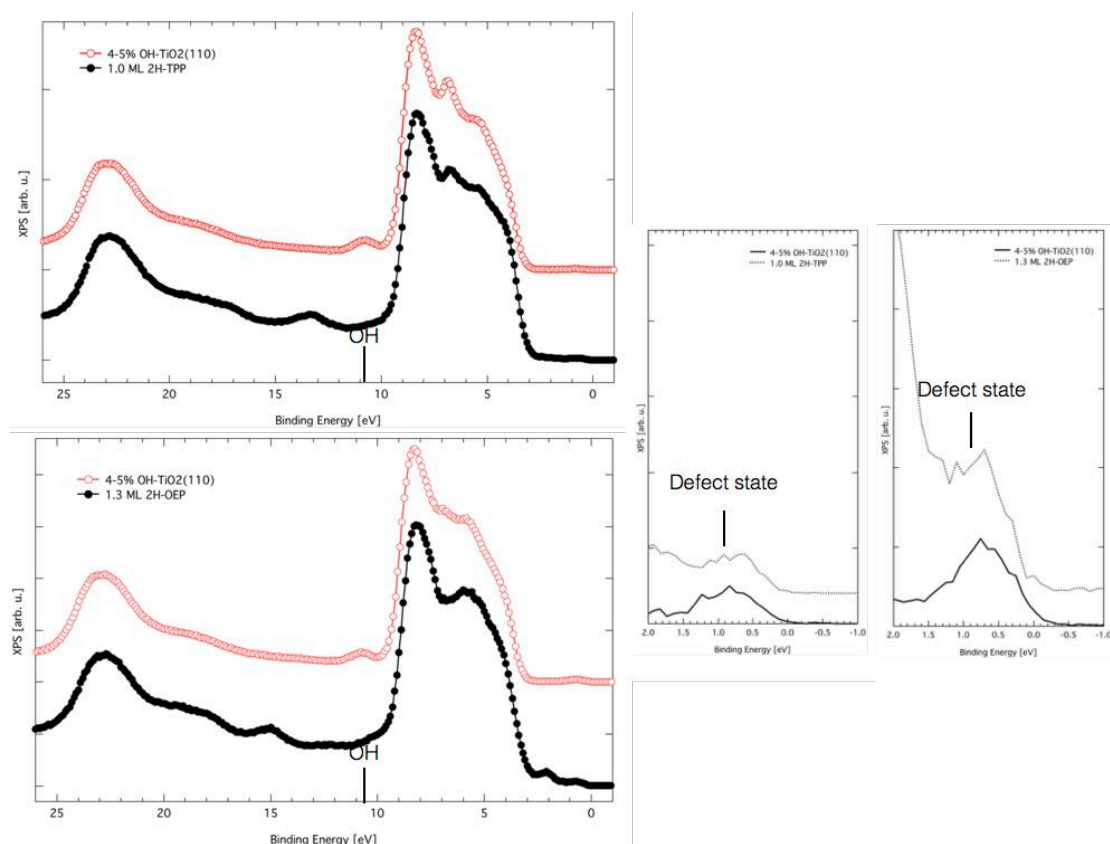


Fig. 4.11. (left) Valence band spectra take at 140 eV photon energy. The OH peak at 11eV is quenched upon deposition of a molecules monolayer of (up left) 2H-TPP and (down left) 2H-OEP. (Right) Detail from the defect states (x20) that remains invariable in both depositions.

Is expected that the annealing of the monolayer at some point should present some chemical and conformational changes before thermal desorption or molecular fragmentation. The N1s photoemission spectra measured during a temperature ramp is shown in Fig. 4.12. The main issue is the gradual switch of the pyrrolic component to a new energy slightly higher than the iminic one, that starts below 100°C for 2H-TPP as reference molecule for the porphyrin repertory.

This new energy corresponds to the one found in films of metal porphyrins, and is coincident in B.E. with the N1s peak obtained by evaporation of Ti atoms over a porphyrin layer, with the advantage that the fully conversion of the pyrrolic component into the metallic one can be achieved by annealing at about 200°C, whereas the metal atoms deposition cannot fully convert a compact layer due to the limited metal diffusion when the surface is completely covered and Ti atoms aggregate into clusters.

It's important to remark that the low onset temperature of the chemical reaction can easily be reached by Dye-sensitized solar cells operative, and due to this low self-metalation temperature and the high Ti atoms reactivity, the trans-metalation can take place in the dye metalloporphyrins.

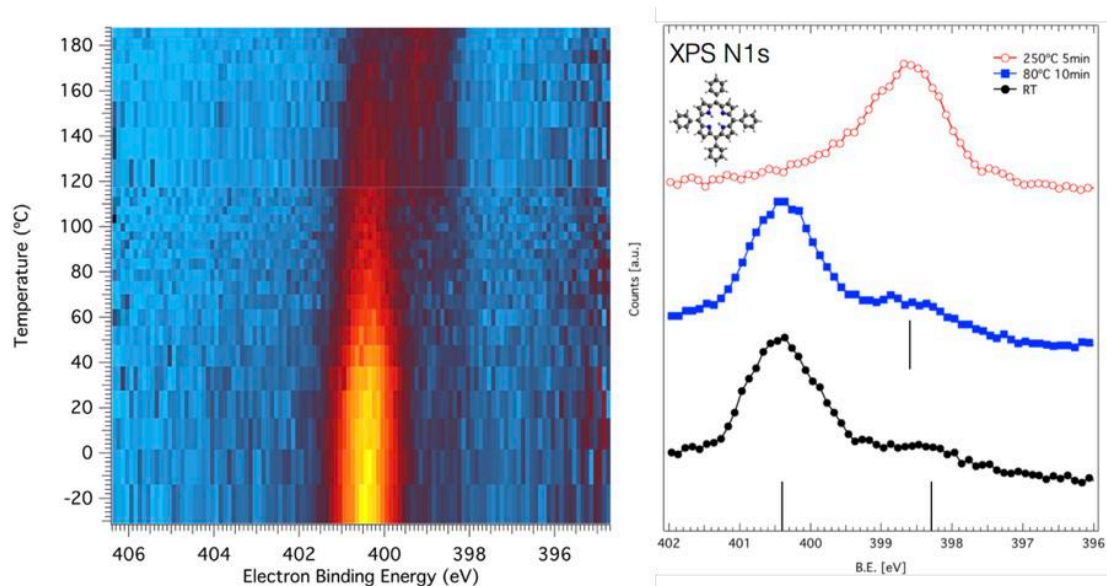


Fig. 4.12 (Left) 2D representation of the intensity of the N1s peak during a continuous scan under controlled annealing of a 2H-TPP monolayer. The binding energy and the temperature are shown in the X and Y axis respectively. (Right) two cuts at RT and 80°C respectively from the left panel, and a last scan taken at the maximum temperature reached during the experiment where the Nitrogen permutes into its metalated energy.

Comparing the C1s and N1s intensity normalizing to the Ti2p intensity of the spectra under further annealing beyond 400°C, a decrease about 20% is noticed, corresponding to a decrease of the molecular density (Fig. 4.13).

The perfect overlap of the Ti 2p spectra (in particular, the low energy tail) seen in Fig. 4.13, with and without molecular overlayer, and before and after annealing, indicates that no change of the amount of Ti3+ and Ti2+ ions is observed upon self metalation. We can conclude that Ti atom incorporated in the macrocycle must have the same oxidation state of the substrate atoms.

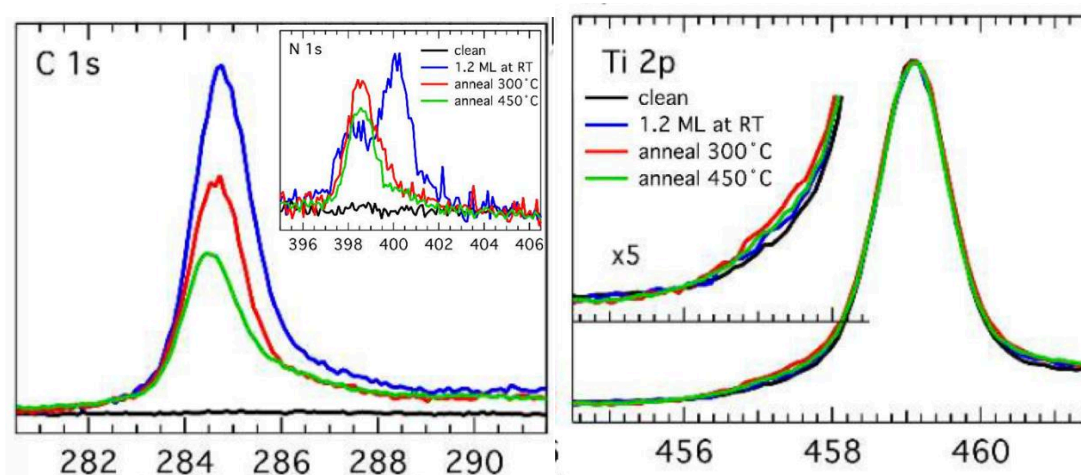


Fig. 4.13 (Left) Photoemission of N1s and C1s peaks from room temperature to annealed molecules monolayer measured with photon energy of 650eV and normalized in intensity to the Ti2p peak. (Right) Photoemission of Ti2p peaks from clean substrate to annealed molecules monolayer measured with photon energy of 650eV and normalized in intensity.

Performing the annealing for the other two species (2H-OEP and 2H-tbTPP), the results are consistent with the self-metalation of the molecule, with a minor difference with respect to

the peripheral substituents, reaching the complete switch of the pyrrolic component into the metallic one at 200°C for the 2H-tbTPP and at 250°C for the 2H-OEP as seen in Fig 4.14.

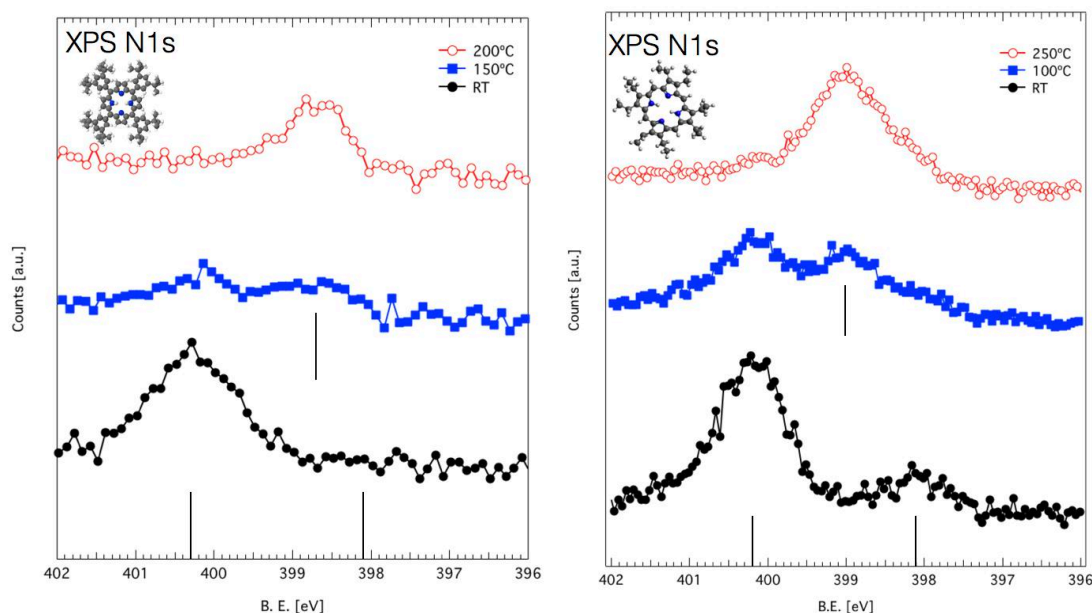


Fig. 4.14. (Left) N1s XPS spectra from 0.8 monolayer of 2H-tbTPP as deposited, and under thermal treatment. The metalation of the molecule is reached and the N1s peak shifts to ~ 398.8 eV. (Right) XPS for N1s during the metalation by thermal treatment of 0.5 monolayer of 2H-OEP. The behaviour is similar to the other porphyrins, and when the metalation is completed the N1s is completely shifted to a binding energy about 398.8 eV.

4.3.2. 2H-TPP NEAR-EDGE X-RAY PHOTOEMISSION SPECTROSCOPY

The proximity of the macrocycle to the substrate governs the conformation of the molecule, mainly the concavity or convexity of the four pyrrole moieties that can be strongly distorted by the incorporation of a metal atom, and the tilt angle and rotations of the peripheral substituents.

To study the correlation of the different molecular conformations and the different thermal treatments which undergo the chemical reaction (i.e. metalation of the macrocycle) near-edge X-ray absorption spectroscopy (NEXAFS) is one of the best complementary techniques.

NEXAFS probes the unoccupied electronic states upon adsorption, providing also an estimation of the charge transfer in the bonding between adsorbate and substrate. The molecular orientation with respect to the surface can also be estimated by analysing the dichroism in the spectra when using linearly polarized photon source [55]. To this aim measurements at the C1s K-edge for the three porphyrins, at room temperature and after annealing are presented in this chapter, with special consideration in the 2H-TPP study. All the measurements have been performed with linearly polarized X-rays with its electric field orthogonal (P polarization) or parallel (S polarization) to the surface plane, and the scattering plane along the [001] symmetry direction.

In the Fig. 4.15. the 2H-TPP carbon K-edge NEXAFS spectra displays a near edge structure with a peak assigned to a LUMO dominated by $1s \rightarrow \pi^*$ transitions into the macrocycle and an intense resonance corresponding to transitions localized mainly on the phenyl rings [56]. Following the procedure discussed in [57] and exposed in 2.3.2. the macrocycle and phenyl contributions can be separated to extract the tilt angle with respect to the surface. The peaks were fitted with low accuracy applying a Fermi step and a Gaussian/Lorentzian fit approximation using XPSmania.

The phenyls tilt angle value is 33.98° for the molecules in the as-grown monolayer at room temperature, presenting a rotation much lower than the 2H-TPP condensed crystal's one [58]. This phenyl tilting is accompanied by a small out-of-plane distortion of the macrocycle, as revealed by the dichroism in the macrocycle peak, with a calculated angle of 14.29° which is consistent with the saddle-shape distortion of the pristine pyrrolic moiety. After annealing to the metalation (250°C), the dichroism of the macrocycle peak is only slightly affected, while the phenyl peak dichroism decreases, giving a calculated tilt angle of 42.2° , as due to an increased rigidity acquired by the entire macrocycle. Further annealing below the decomposition limit (400°C) exhibits an almost complete dichroism of both, macrocycle and

phenyl peaks, corresponding to a strong planarity of the molecule usually seen in the aromatization of carbon compounds, with a tilt angle calculated for the macrocycle pyrroles of 11.9° and a tilt angle for the phenyls about 10.4°, that would be ascribed to a cyclo-dehydrogenation of the metalated-porphyrin.

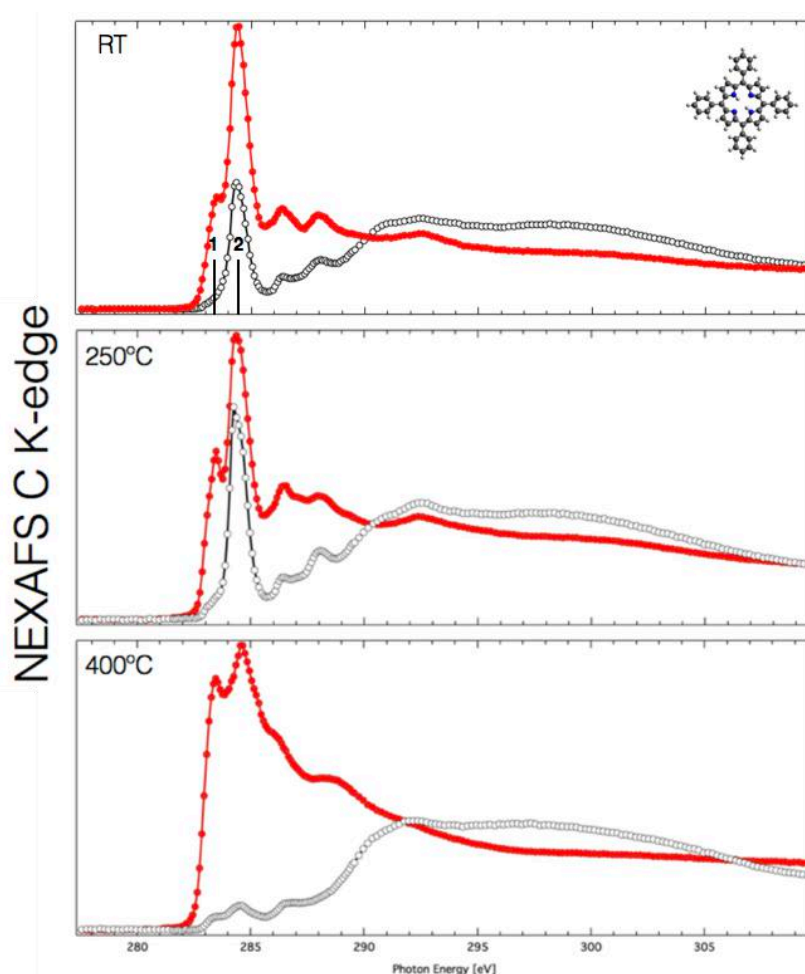


Fig. 4.15. 2H-TTP monolayer over rutile-TiO₂(110) 1x1 Carbon K-edge polarized NEXAFS. The spectra have been normalized to the absorption measured on the clean TiO₂(110) surface. Displaying (up) 1ML at RT and (middle) formation of metalated monolayer after annealing at 250°C and (down) the strong dichroism after annealing over 400°C. The two black bars indicate the LUMO and LUMO + 1 $1s \rightarrow \pi^*$ transitions ascribed to (1) C-macrocycle and (2) C-phenyl.

NEXAFS from Nitrogen K-edge at RT shown in the Fig. 4.16. instead present three peaks corresponding to the π -symmetry unoccupied states localized on the iminic (LUMO) at 397.7 eV and the pyrrolic (LUMO+1) nitrogen at 400.1 eV and another resonance at 402.0 eV. The residual iminic contribution can be associated with the residual iminic intensity observed in the photoemission spectra, since the surface is mostly covered by acidic 4H-TPP molecules at RT, and the third one would be ascribed to the metalloporphyrin phase. Both, the iminic and the pyrrolic peaks display a strong dichroism, where the residual intensity of the pyrrolic peak in S polarization may be equally contributed by a bending of the macrocycle and by the rehybridization of MO following the NH bonding to the O_{br} atoms. A dip would be seen due to the normalization.

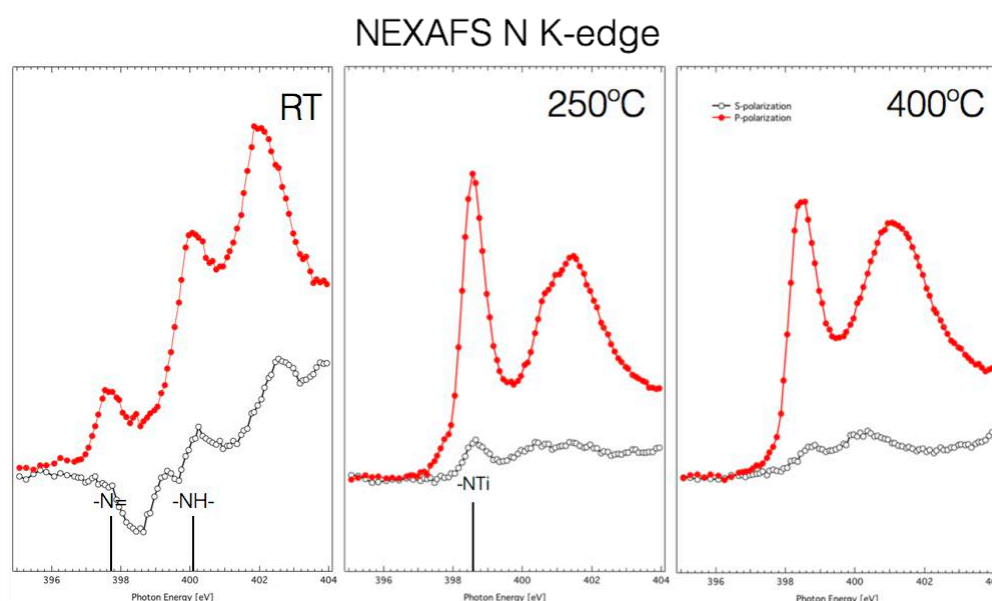


Fig. 4.16. 2H-TPP monolayer over rutile-TiO₂(110) (1x1) Nitrogen K-edge polarized NEXAFS. The spectra have been normalized to the absorption measured on the clean TiO₂(110) surface. From left to right we can follow the evolution of the LUMOs after and before metalation, and their strong dichroism.

Under annealing both components, iminic and pyrrolic, converge into a single π^* symmetry LUMO corresponding to the metalated macrocycle (NTi). This peak presents a large dichroism, in agreement with the metalation of the macrocycle units.

4.3.2.1. COMPARISON WITH 2H-OEP AND 2H-TBTPP

NEXAFS from Carbon K-edge of the 2H-OEP are reported in the Fig. 4.17. there is still present the macrocycle LUMO (284.3 eV) with a high dichroism at room temperature and at the self-metalated monolayer and a second component that can be attributed to the LUMO +1 (285.1 eV) of the pyrrolic rings presenting a dichroism following that from LUMO counterparts. The tilt angle of the pyrrole units in the macrocycle is about 8.3°.

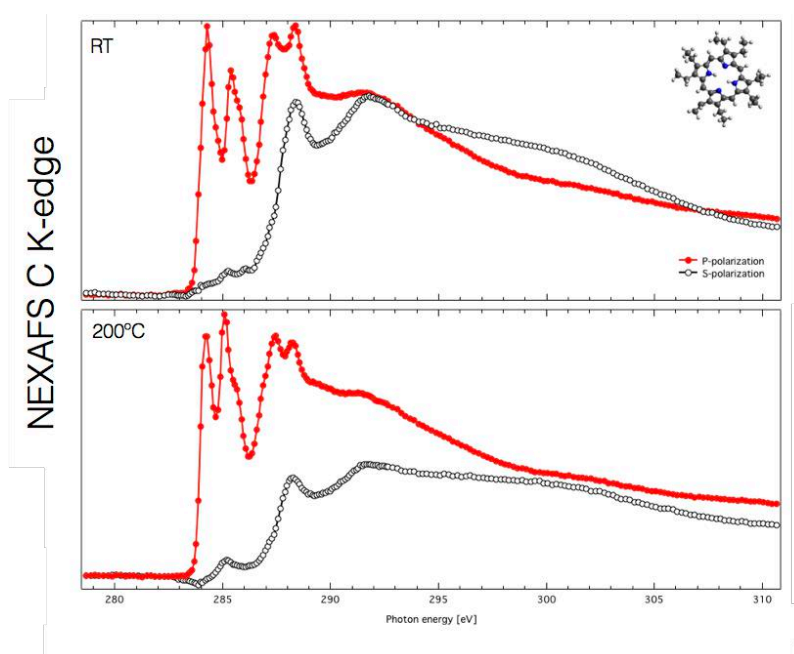


Fig. 4.17. 2H-OEP 1.3 monolayer over rutile-TiO₂(110) 1x1 Carbon K-edge polarized NEXAFS. The spectra have been normalized to the absorption measured on the clean TiO₂(110) surface. (up) 1ML at RT and (down) formation of metalated monolayer annealing at 200°C.

After annealing only minor changes in the peaks ratio are detected due to the metalation relaxation of the porphyrins with an increment of the macrocycle tilt angle to 12.4°.

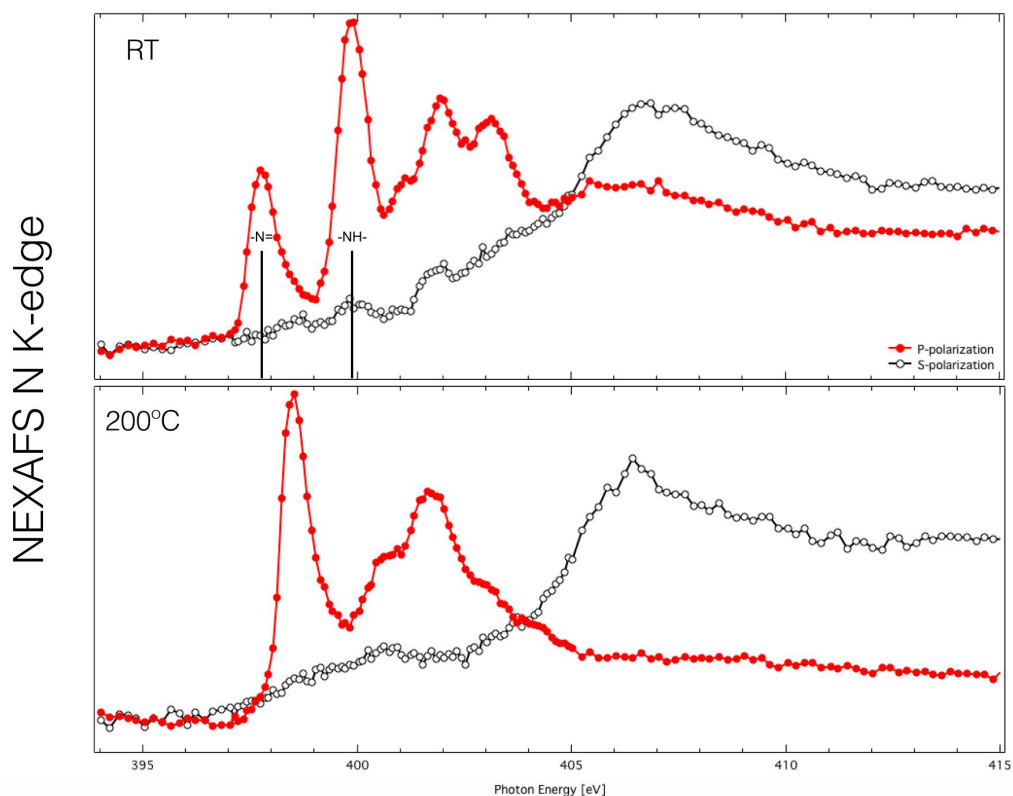


Fig 4.18. 2H-OEP 1.3 monolayer over rutile- $\text{TiO}_2(110)$ 1x1 N K-edge polarized spectra normalized to the absorption measured on a clean rutile- $\text{TiO}_2(110)$ surface. Displaying (up) 1ML at RT and (down) formation of metalated monolayer annealing at 200°C. The iminic and pyrrolic N contribution can be easily ascribed to the LUMO and LUMO+1.

NEXAFS from Nitrogen K-edge shown in the Fig. 4.18. instead presents two peaks corresponding to the π -symmetry unoccupied states localized on the iminic (LUMO) at 397.8 eV and the pyrrolic (LUMO+1) nitrogen at 399.9 eV. The residual iminic contribution can be again originated by the residual iminic intensity observed in the photoemission spectra and

the fact that the measurement is performed for a thickness of 1.3 monolayer. The iminic component presents a larger dichroism with respect to the pyrrolic one, suggesting that the macrocycle of the doubly hydrogenated 4H-OEP porphyrin has a larger saddle-shape distortion with respect to the 2H-OEP bare porphyrin. After annealing, the resonances from the inequivalent Nitrogen converge into a single peak at 398.6 eV that is in good agreement with that reported for metalloporphyrins (i.e. primarily Fe-OEP) [59]. This peak presents a large dichroism and there is no contribution from the pristine nitrogen resonances, according with a complete metalation of the layer.

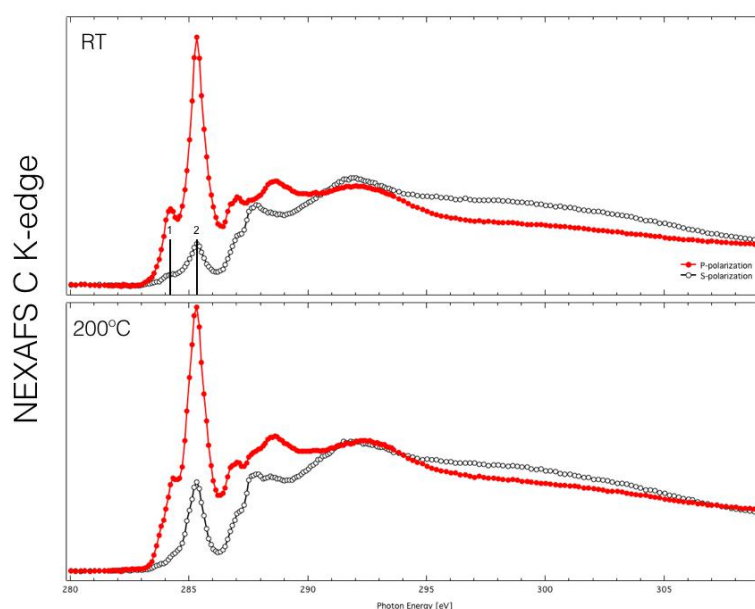


Fig. 4.19. 2H-tbTPP monolayer over rutile-TiO₂(110) (1x1), C k-edge polarized NEXAFS normalized to the absorption measured on a clean rutile-TiO₂(110) surface. Displaying (up) 1ML at RT and (down) formation of metalated monolayer by 2 layers' desorption after annealing at 200°C.

For the Carbon K-edge of 2H-tbTPP, again the two main resonances LUMO (284.1 eV) and LUMO+1 (285.3 eV) stem from the macrocycle and the phenyl rings as seen on Fig. 4.19. The

dichroism at room temperature give us a tilt angle 22° for the phenyl rings, and 16.9° for the macrocycle, indicating an even larger flexibility and relaxation than for TPP. After annealing the phenyl rings LUMO+1 present a smaller dichroism that can be assigned to an increased tilting off the surface by 31° of the phenyls after metalation, in qualitative agreement with the case of TPP.

The rotation of the pyrrole and the phenyl components from each species are summarized in the Table 4.1.

MOLECULE/TEMPERATURE	PYRROLE	PHENYL
2H-TPP / RT	14.29°	33.98°
2H-TPP / 250°C	13.6°	42.2°
2H-TPP / 400°C	11.9°	10.4°
2H-TBTPP / RT	16.9°	22.0°
2H-TBTPP / 200°C	17.1°	31.1°
2H-OEP / RT	8.3° (1^{st} peak)	***
2H-OEP / 200°C	12.4° (1^{st} peak)	***

Table 4.1. Calculated tilt angles with respect to the substrate plane by fitting the peaks from the C K-edge polarized NEXAFS associated with excitations localized in the macrocycle pyrroles or in the phenyl rings, after different thermal treatments.

4.3.3. 2H-TPP FILM STRUCTURE DETERMINATION: STM AND RHEED

At room temperature, individual 2H-TPP molecules, as shown in the Fig. 4.20. appear as an isolated monomer displaying six lobes, with the typical saddle-shape observed on metal

surfaces [60]. The two main lobes are ascribed to the pristine pyrroles over the O(2c) rows that point down, while the other four lobes correspond to the tilted phenyl rings.

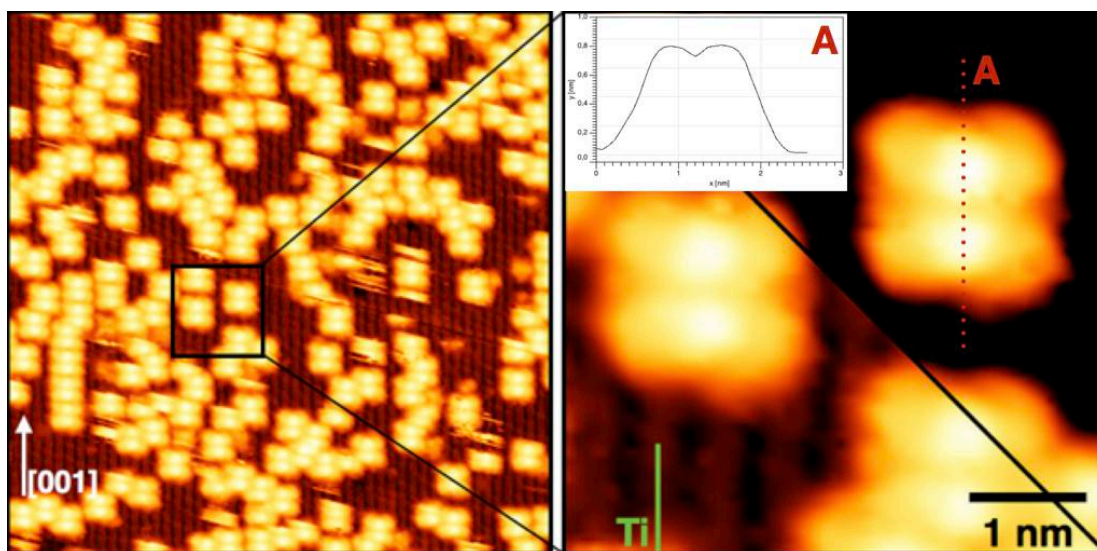


Fig. 4.20. (left) STM image 24.7x24.7nm from a 2H-TPP sub-monolayer as deposited and (right) a cut showing the single molecule profile and relative height respect to the substrate. (Bias=-1.4V Tunneling Current=6pA)

All the molecules are aligned along the [001] direction above the oxygen rows. The observed presence of spikes and scratches in the scan direction in correspondence of isolated molecules is indicative of relatively high mobility along the rows at room temperature.

After thermal treatment above the complete metalation temperature $> 100^{\circ}\text{C}$, the situation is more complex with several new species. In the Fig. 4.21. we can distinguish at least four kind of monomers: i) most of them display the same saddle-shape structure aligned to the O(2c) rows, like those observed at room temperature, ii) some of them still have a dominant saddle-shape, but display an uniaxial asymmetry along the row direction, iii) a few of them display a rectangular structure, centred on Ti(5c) rows and an azimuthal rotation by 60° , and iv) the last one.

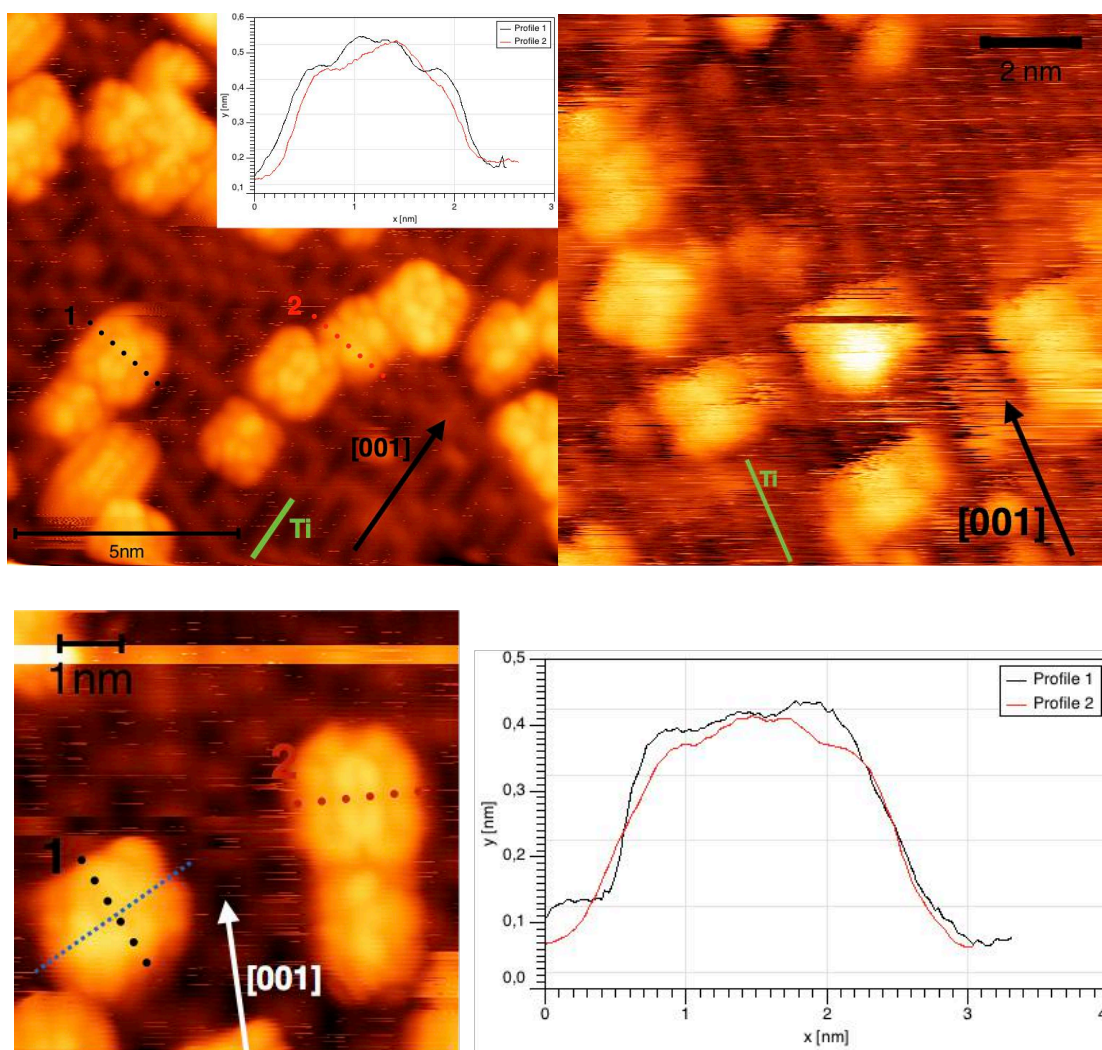


Fig. 4.21. Different molecular conformation of 2H-TPP after thermal treatment over metalation temperature. (Up left) Image showing molecules with saddle-shape aligned over $O(2c)$ rows, and molecules with uniaxial asymmetry along the rows direction and its profiles. Bias=1.2V Tunneling Current=5pA 15x15nm. (Up right) Molecules with saddle-shape aligned over the $O(2c)$ rows and molecules rotated by 45° aligned over the $Ti(5f)$ rows. Bias=1.48V tunneling current=4.5pA 13x13 nm. (Down left) Molecule with characteristic saddle shape over $O(2c)$ row and its profile, and rectangular shape molecule over $Ti(5f)$ row and (down right) its profile along the short axis, the 60° rotated axis is marked in blue. Bias=1.4V Tunneling current=5pA 7x7nm.

Raising the temperature to 400°C, where the NEXAFS presents the larger dichroism the monomers again adopt a predominant configuration, with a flat rectangular shape centred on Ti(5c) rows and majority rotated by 30° with respect to the [001] direction as seen in Fig. 4.22. This can be ascribed to a cyclodehydrogenation reaction [61] like the one seen in the Fig. 4.23, where the molecule loses eight Hydrogens corresponding to the ortho-positions of the phenyl rings and the adjacent hydrogens at the porphyrin core.

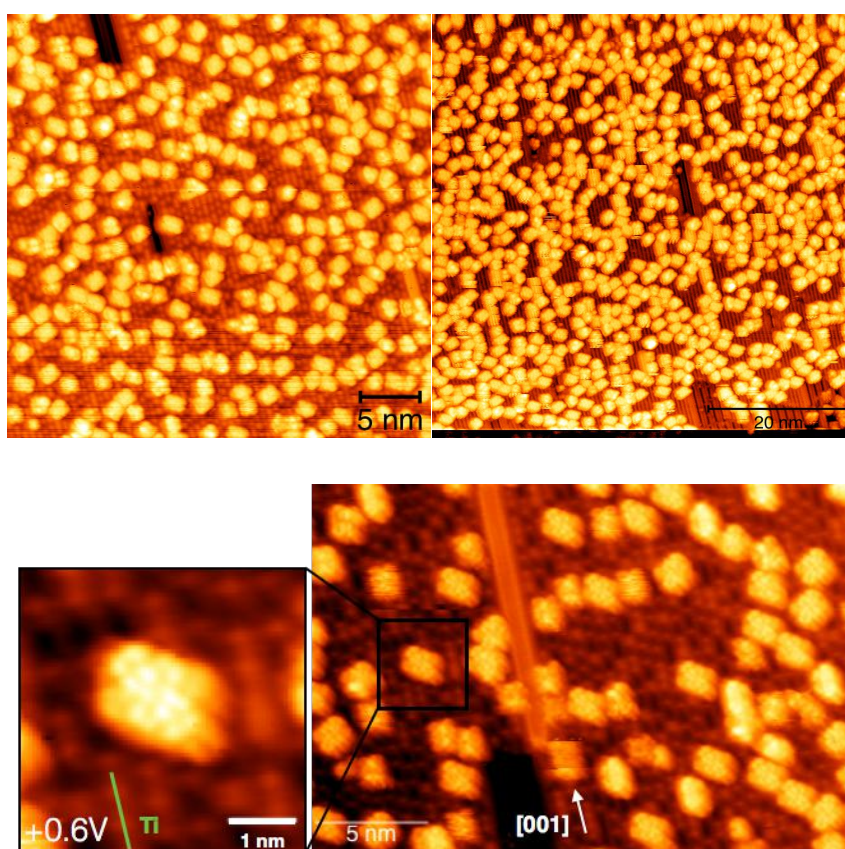


Fig. 4.22. (Left) STM image from self-metalated sub-monolayer of 2H-TPP over rutile-TiO₂(110) with predominance of rectangular shape molecules. Bias= 1.4V, Tunneling current= 4pA, 35x35nm. (Right) Same phase STM image at negative bias showing similar behaviour. Bias=-1.6V, tunneling current=4pA, 60x60nm. (Down right) STM image with (down left) detailed molecule topography where its characteristic DOS distribution is recognizable. Bias=0.6V, tunneling current=4pA.

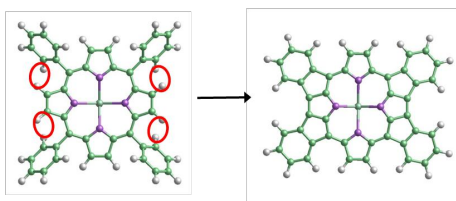


Fig. 4.23. Cyclodehydrogenation sketched in ball-and-stick model. Green = Carbon, Purple = Nitrogen, White = Hydrogen. Metalated molecule with a green core atom.

The high coverage range presents a different behaviour due to the molecule-molecule interaction. Initially the molecules don't aggregate into islands due to small van der Waal's intermolecular interaction. As the coverage increases and molecules along O(2c) rows enter in contact, their phenyl rings start to arrange the molecules into an ordered scheme corresponding to a commensurate oblique-(2x4) phase displaying slanting rows of molecules with respect to the [001] direction as seen in the Fig. 4.24. This phase is recognizable in RHEED patterns taken along the $[1\bar{1}1]$ to highlight the fractional spots along this direction, as seen in Fig 4.25.

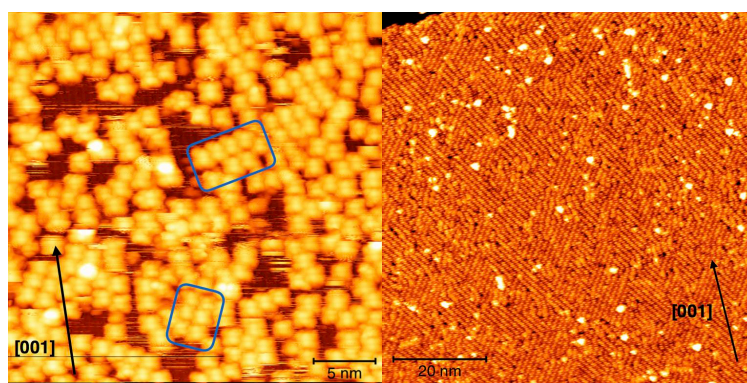


Fig. 4.24. (Left) Growing of the high density phase at RT. Bias= -1.299V, Tunneling Current=4pA, 30x30 nm. (Right) STM image from high coverage 2H-TPP obtained by multilayer desorption with a thermal treatment over the metalation temperature (300°C). Bias= 2.5V, tunneling current = 10pA.

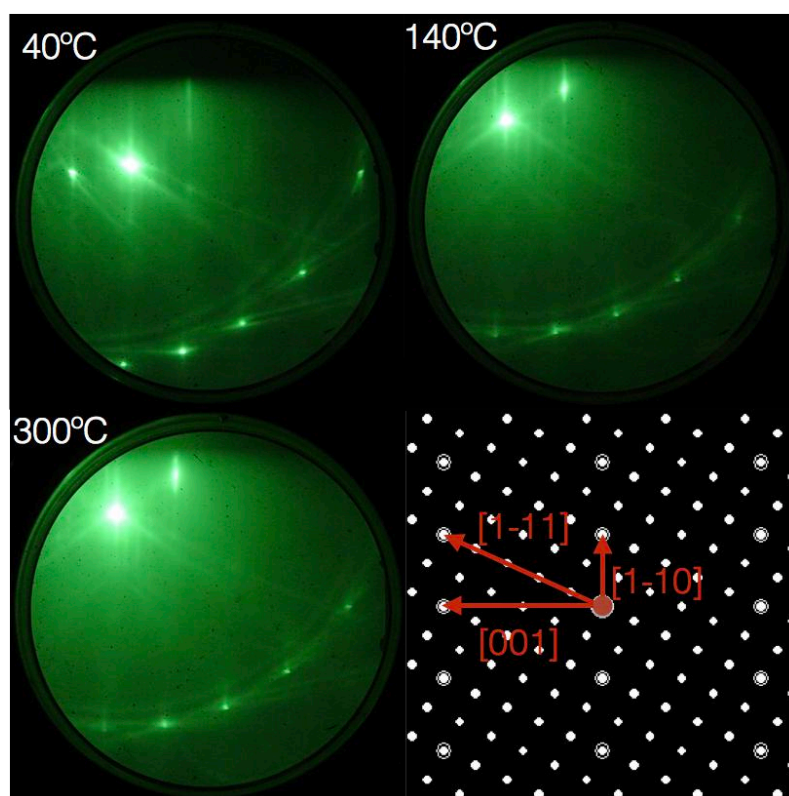


Fig. 4.25. The RHEED images are taken from a 0.9ML in the $[1-11]$ direction to highlight the characteristic five-fold diffraction pattern, under different temperatures (up left) RT, (up right) 140°C and (down left) 300°C, for thermal treatment. (Down right) The calculated LEED pattern of the oblique-(2x4) phase with a single domain is shown for comparison.

Under thermal treatment the phase remains unchanged as seen in the until reaching the cyclodehydrogenation temperature (about 400°C), when a new phase r-(2x6) is seen according with RHEED pattern and the image analysis as seen on Fig. 4.26. In fact, further annealing to 350°C yields the coexistence of extended domains with oblique-(2x4) and rect-(2x6) symmetry. This new phase starts in the middle of the o-(2x4) domains by formation of molecular rows along the $[001]$ direction, being fully converted at about 400°C, where the molecules line up in perfectly parallel linear rows with a rectangular superlattice that is collinear to the substrate primitive lattice (Fig. 4.26). Upon further heating to 450°C and higher, the molecular rows still preserve their sharp straightness, but local domains are

formed with $\begin{pmatrix} 1 & 2 \\ 6 & 0 \end{pmatrix}$ symmetry, here after called oblique-(2x6), together with the rect-(2x6) (Fig. 4.27).

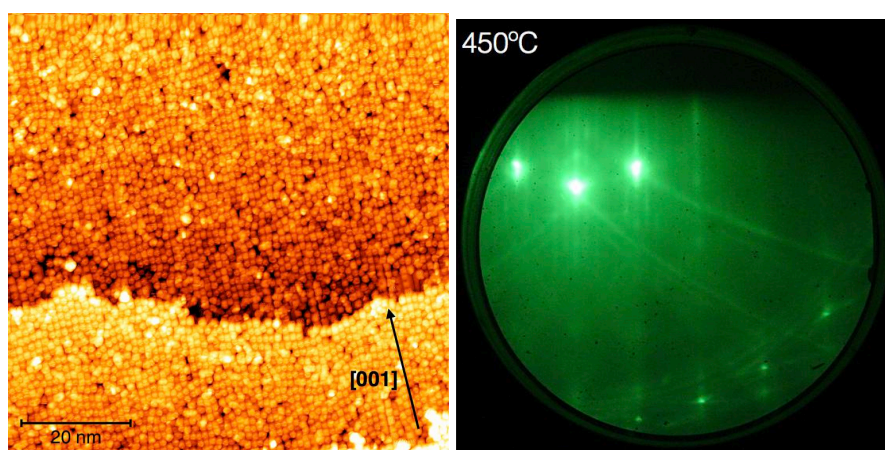


Fig. 4.26. (Left) Annealing above 400°C. Bias= -1.5V Tunneling Current = 8pA, 80x80nm. (Right) The RHEED was taken in a 0.9ML annealed at 450°C along the [001] direction, to highlight the r-(2x6) phase.

The molecules preserve a clear nodal plane transverse to the molecular rows, suggesting that the macrocycle is no significantly changed (Fig. 4.27). Finding the exact registry of the molecules with the substrate along the rows, they are still adsorbed atop the substrate O_{br} rows, like 2HTPP, 4HTPP and TiO_2 -TPP. Full molecular desorption would be observed on terraces where the substrate displays the characteristic (2x1) reconstruction, as originated by very high oxygen reduction. The correspondence of the molecular rows with the O_{br} rows can be determined a posteriori from the comparison with images obtained for the clean surface on adjacent terraces displaying either surface reconstruction. As shown in the i Fig. 4.27, the molecular rows are always in between the projected lines of the $Ti5f$ substrate rows. This finding suggests that also the absorption site in the (2×6) phase is the same as the o-(2×4) one that is on bridge between two O_{br} atoms. In contrast, a conformational change of the phenyl terminations is expected from the change of the molecular shape that

displays a perfect rectangular symmetry in the (2×6) phases. For comparison, the two main lobes rather display an opposite transverse displacement (asymmetry) with respect to the $[001]$ direction in the $o\text{-(}2 \times 4\text{)}$ phase

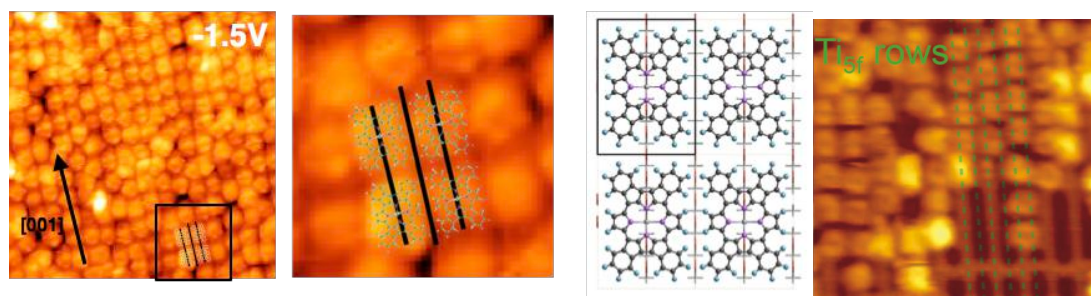


Fig. 4.27. (from left to right) STM detail image and inset including molecular model from $r\text{-(}2 \times 6\text{)}$ phase. Molecular model from $r\text{-(}2 \times 6\text{)}$ phase. STM image from (2×6) phase atop reduced TiO₂(110) surface. The Ti5f rows can be easily ascribed to the green segment lines taking the (1×2) reconstruction as reference.

4.3.3.1. COMPARISON WITH 2H-TBTPP

STM measurements shown in Fig 4.28. of 2H-tbTPP sub-monolayer deposited at room temperature, present a single squared monomer composed by multiple two-fold lobes, four around the core and eight less protruding surrounding them in pairs in a saddle-shape conformation. They can be attributed to the tert-butyl groups due to its position and distances, and the calculated rotation for the phenyl rings according with the NEXAFS analysis. The molecules adsorb above the O(2c) rows. The molecule-molecule interaction is weaker than the adsorption until the coverage forces the contact between molecules along the O(2c) rows, starting to aggregate into ordered clusters.

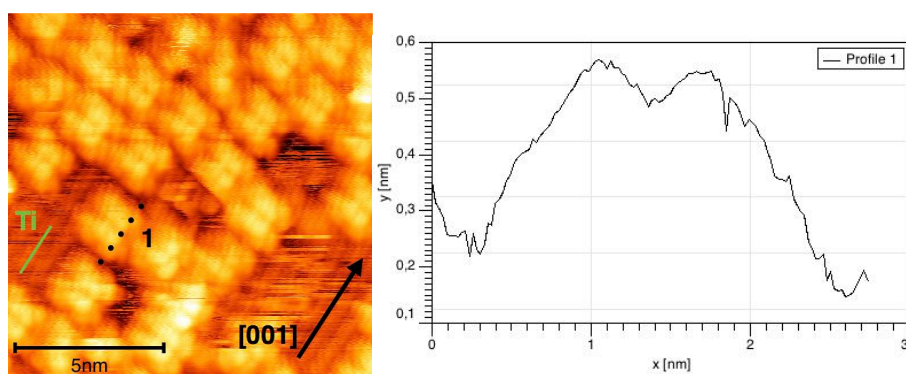


Fig. 4.28. STM image from RT submonolayer of 2H-tbTPP over rutile-TiO₂(110). Bias=1.26V, Tunneling Current= 22pA.

After thermal treatment at the metalation temperature (>250°C) the molecules adopt a characteristic rectangular shape with a well define nodal plane and still adsorb above the O(2c) rows, as seen on Fig. 4.29. This rectangular shape is not necessary ascribed to a cyclo-dehydrogenation, but the redistribution of the tert-butyl groups due to the tilt of the phenyls [62].

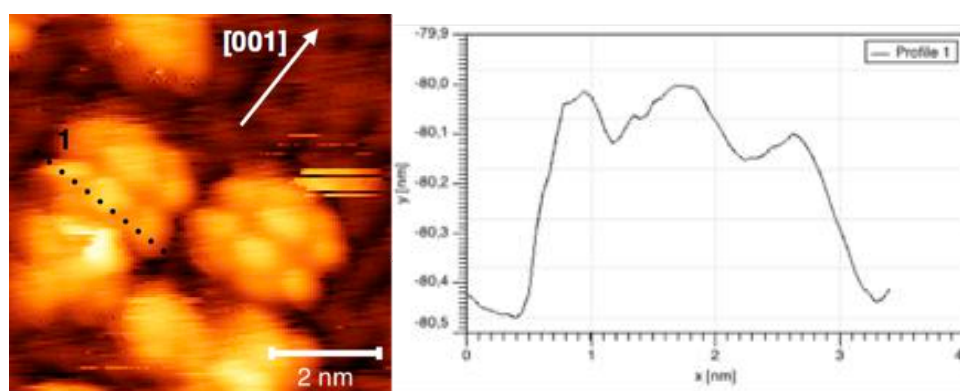


Fig. 4.29. STM image from submonolayer of 2H-tbTPP over rutile-TiO₂(110) after thermal treatment over the metalation threshold. Bias = 1,65 V Tunneling Current = 6 pA.

4.3.4. 2H-TPP THEORETICAL APPROACH

Model density functional theory (DFT) calculations were performed using the Quantum ESPRESSO package [63], using the PBE functional [645] and Grimme dispersion corrections [65, 65]. These simulations have been performed by Dr. Andrea Vitadini and Dr. Daniel Forrer from CNR-IENI (Padova).

The ion cores are described by Vanderbilt ultrasoft pseudopotentials (PPs) including C, N and O 1s orbitals, and the Ti ions by large core PPs including 1s—3p electrons or small cores including 1—2p electrons. The kinetic energy cut-off for the plane-wave expansion was 25 Ry and 200 Ry for the Vanderbilt augmentation charge.

The supercell size depends on the coverage simulated conditions, including always four TiO₂ layers, with the two bottom layers frozen in the bulk structure. Due to the large size of the supercells only the Γ point of the Brillouin zone was sampled.

To simulate low-coverage conditions an oblique $\begin{pmatrix} 3 & 3 \\ 6 & 1 \end{pmatrix}$ supercell including 21 unit cells and the PBE-D lattice constants of TiO₂ were used. To simulate high-coverage instead two oblique supercells $\begin{pmatrix} 2 & 2 \\ 4 & 1 \end{pmatrix}$, $\begin{pmatrix} 2 & \bar{2} \\ 5 & 1 \end{pmatrix}$ and two (2x6), $\begin{pmatrix} 0 & 2 \\ 6 & 0 \end{pmatrix}$, $\begin{pmatrix} 1 & 2 \\ 6 & 0 \end{pmatrix}$ were modelled.

4.3.4.1. LOW COVERAGE FILMS

Ab initio calculations predict that the gas-phase hydrogenation for the 2H-TPP is faintly exothermic at 0 K, and assuming an ideal gas behaviour for H₂, about $\Delta G \approx +0.3$ eV at RT, in agreement with the presence of 2H-TPP and not 4H-TPP and according with the possibility that the TiO₂ providing dissociated hydrogen on the surface would stabilized the 4H-TPP

species. The absorbed 2H-TPP was then simulated using periodically repeated slab models with PBE-D theoretical lattice constants of the substrate taking into account the Scanning Tunneling Microscopy (STM) measurements, to determine its absorption site. At low-coverage, STM unambiguously displays the molecules with a common azimuthal orientation atop the oxygen rows with the squared molecular edge parallel to the [001] direction and a nodal plane transverse to the Oxygen rows, due to the upward/downward tilt of the macrocycle adjacent pyrroles.

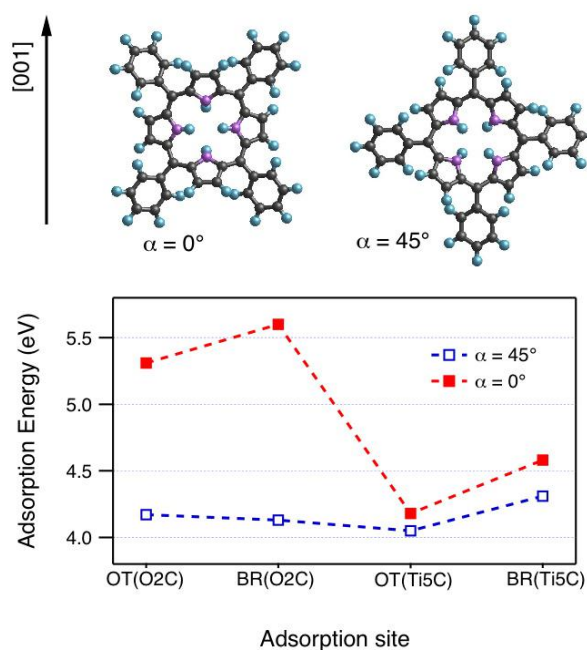


Fig. 4.30 Adsorption energy of 4H-TPP as a function of the adsorption site on the O(2c) and Ti(5c) rows. The value has been calculated for two different azimuthal orientations (0° and 45°) of the macrocycle respect to the [001] direction.

Adding the NEXAFS results and the D_{2h} symmetry of the STM molecules, only two azimuthal orientations are possible: with two opposite Nitrogen atoms along the substrate [001] direction or rotated by 45° from it. The adsorption on Ti 5-fold rows (Ti(5c)) and Oxygen

bridge 2-fold (O_{br} and $O(2c)$) on-top and on-bridge sites are considered. As computed for 3-layers slabs and large-core pseudopotentials, the most favoured adsorption site for 2H-TPP and the hydrogenated 4H-TPP one is found as shown in Fig. 4.30. on the bridge position between two adjacent O_{br} atoms along the [001] substrate direction, with the opposite Nitrogen parallel to it (azimuthal rotation 0°), which is favoured by almost 1 eV. The best estimations computed with 4 ML slabs and small-core pseudopotentials are of 5.31 eV for 4H-TPP and 3.41 eV for 2H-TPP.

As seen in Fig. 4.31, in this most favoured configuration, two equivalent $N-H\cdots O_{br}$ H-bonds are formed in agreement with the downward tilt of the corresponding pyrrolic rings whose peripheral carbon atoms protrude above the macrocycle plane, showing larger intensity in the topographic images. The other two central rings display a tilt in the opposite direction showing a dimmed contrast in the transverse direction.

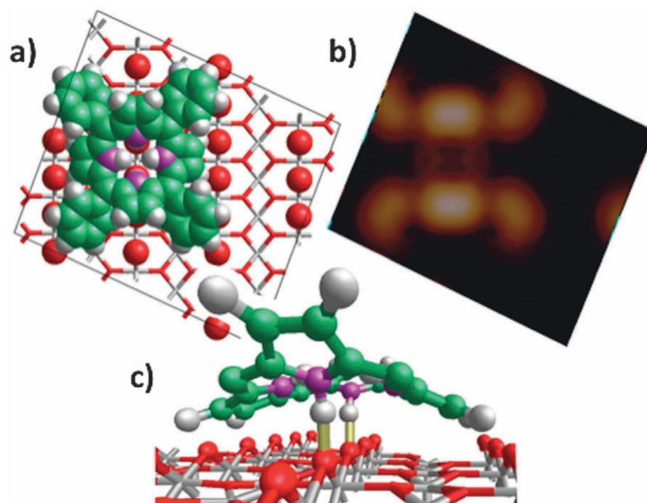


Fig. 4.31. (a) Ball and sticks model of the 4H-TPP adsorption configuration, where the adopted supercell is also sketched. (b) The simulated STM image is shown, whose saddle-shape is in agreement with the experimental images. (c) The deformation of the adsorbate can be appreciated in this perspective, with the $N-H\cdots O_{br}$ bonds are highlighted as yellow sticks.

The topographic calculated images for both species 2H-TPP and 4H-TPP are similar with a larger bending by 6° of the pyrrolic units upon hydrogen uptake. Although it cannot be observed in the STM images (which is performed at room temperature), this is consistent with the dichroism of the residual iminic component in the N K-edge compared with the pyrrolic one. Once reached this configuration, the energy reaction of hydrogen uptake from the surface is much more exothermic (-1.40 eV) with respect to the gas-phase.

The mechanism of hydrogen incorporation into the TiO₂ bulk is a controversial discussion [67, 68, 69] but there is a consensus about the interlayer H diffusion barrier calculated (about 1 eV for the TiO₂(110) planes), opening energetically taking the trapped hydrogen in the bulk as hydrogen source for the hydrogenation.

We estimated the N1s core level shifts of the isolated 2H-TPP and the adsorbed 2H-TPP and 4H-TPP by hybrid-DFT calculations with the PBE0 functional [70]. The calculations were performed with the ADF code [71]. Inner electrons of Ti (3p levels), O (1s levels) and C (1s levels) were considered frozen cores, while all the electrons of Nitrogen atoms were allowed to relax. The scalar Zero Order Regular Approximation (ZORA) to the relativistic Hamiltonian was applied [72, 73]. The surface was represented as Ti₃₁O₉₂H₆₀ cluster considering the adsorbed molecules models as a cluster cut out of the optimized slab properly saturated with H atoms.

These DFT simulations of the N1s photoemission peaks reproduce quite well the observed core level shift between the iminic and the pyrrolic nitrogen of 2H-TPP. The uptake of two hydrogen atoms instead yield a small shift of ~0.3 eV to higher binding energy (BE) with respect to the pristine pyrrolic pair coordinated with the oxygen rows. This small CLS are not resolved in the XPS measurements but is consistent with the broadening ($\Delta\text{FWHM} = +0.4\text{eV}$) of the main nitrogen component observed in the monolayer range with respect to the multilayer.

Then, Low coverage 2H-TPP layers at room temperature show that molecules are full hydrogenated, adsorbed on the O(2c) rows of the surface, and in a saddle-shape

deformation, where the pyrroles along the O(2c) rows point their NH groups towards the O neighbours forming hydrogen bonds.

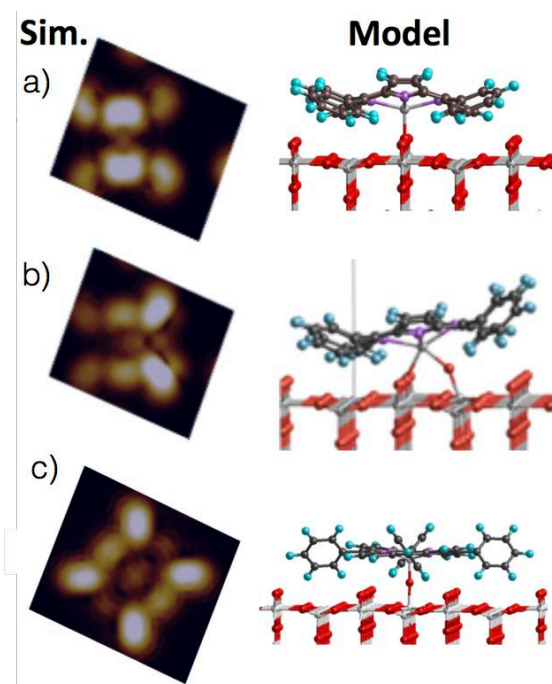


Fig. 4.32 (a) Ball and sticks model of the TiTPP adsorption configuration, and its simulated STM image that is in agreement with the experimental images. (b) Model and simulation of the TiTPP after capturing a diffusing Oxygen, (c) and simulation and model after rotated 45° and adsorbs over Ti(5c) rows as TiO-TPP.

After annealing at moderate temperature, the species for the low coverage observed are three as shown in the STM measurements. Using the same model, and comparing them, we realised that the first species are related to the same species seen at high coverage, since they present similar shape, corresponding with TiTPP on top of a O2c site. The simulations of an isolated TiTPP adsorbed at O2c site are shown in the Fig. 4.32.

Two different azimuthal rotations were taken in consideration for modelling this TiOTPP species on a Ti5c sites as for the free-base units. The 45° rotation is strongly favoured (0.66 eV). The 0° rotation is unstable (by 0.29 eV) with a lateral displacement towards the O(2c) row giving rise to the second units in the Fig. 4.32.

We propose that TiTPP species are converted by diffusing oxygens and its kinetic stabilization requires a 45° rotation of the molecule.

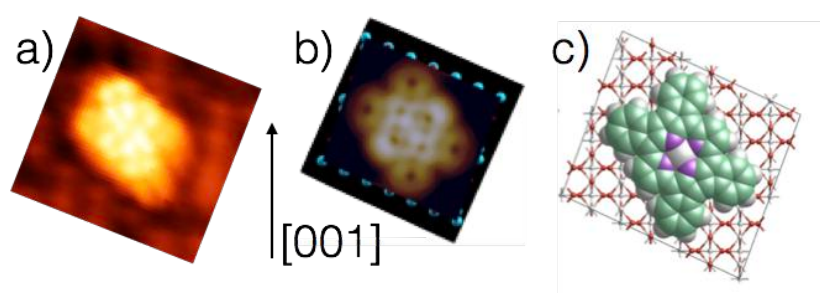


Fig. 4.33. (a) STM experimental image from cyclodehydrogenated TiOTPP molecule, (b) simulated molecule in complete agreement and (c) balls and sticks model adopted for the simulation.

Annealing to higher temperatures ($\sim 350^\circ\text{C}$) we assume that the last and more stable species are cyclodehydrogenated. Assuming the TiTPP species absorbed on O(2c) sites are progressively when annealing converted into TiOTPP species absorbed at Ti(5c) sites and considering the cyclodehydrogenation of this last units, an isolated cyclodehydrogenated TiOTPP molecule on Ti(5c) site with three different configurations was modelled, with the axis oriented along the phenyl's bounded pyrroles rotated perpendicular (90°), parallel (0°) and 30° respect to the [001] direction. The result was that the 30° orientation observed experimentally is preferential respect to the 90° by 1.01 eV and to the 0° by 0.07 eV, obtaining a remarkable similarity to the experimental STM image from the Tersoff-Hamann simulation model shown in the Fig. 4.33.

4.3.4.2. HIGH COVERAGE FILMS

The experimental STM images and RHEED suggest that as the coverage increases molecules along adjacent O_{br} rows enter in contact and the phenyls interaction starts to arrange an ordered scheme corresponding to a commensurate $\begin{pmatrix} 2 & 2 \\ 4 & 1 \end{pmatrix}$ symmetry (oblique-(2x4)) close to the completion of the monolayer, which displays the highest density packing observed ($\rho=0.52$ mol/mm²). This oblique-(2x4) symmetry phase is reached by multilayer desorption or calibrated MBE deposition in the monolayer regime (from 0.8 to 1.0 ML). During the growth, eventually domains with $\begin{pmatrix} 2 & \bar{2} \\ 5 & 1 \end{pmatrix}$ symmetry (oblique-(2x5)) are locally formed with a lower density packing ($\rho=0.43$ mol/mm²).

Opposite to low density films, at high density films only a single species is present after annealing. This most favoured molecular configuration corresponds with TiTPP@O(2c) that remains on the bridge site on the O_{br} rows with minor changes of the molecular arrangement.

The adsorption energy for the three possible chemical states, 2H-TPP, 4H-TPP and Ti(O_{2c})-TPP is calculated starting from the isolated molecule configuration on both supercells and leads minor azimuthal reorientations due to phenyl coupling until the equilibrium. The results shown in Fig. 4.34. for both symmetries oblique-(2x4) and oblique-(2x5) corresponding with the two recognized densities display a small azimuthal reorientation of 8° for the oblique-(2x4) phase and a perfect alignment respect to the high symmetry direction for the oblique-(2x5) for all three chemical states. The absorption energy decreases slightly when passing from low density to high density model, which favours the formation of high density films. This difference is minimum for the 2H-TPP and maximum for the Ti(O_{2c})-TPP. If we take instead in count the specific absorption energy ϵ_{ads} as the adsorption energy and the film density direct correlation ($\epsilon_{ads} = E_{ads} \cdot \rho$), increasing the film density is

convenient and the energy gain maximum for the 4H-TPP and minimum for the Ti(O2c)-TPP, but the oblique-(2x4) phase is favoured in this case for any chemical species in agreement with the experimental evidence from RT to 300°C.

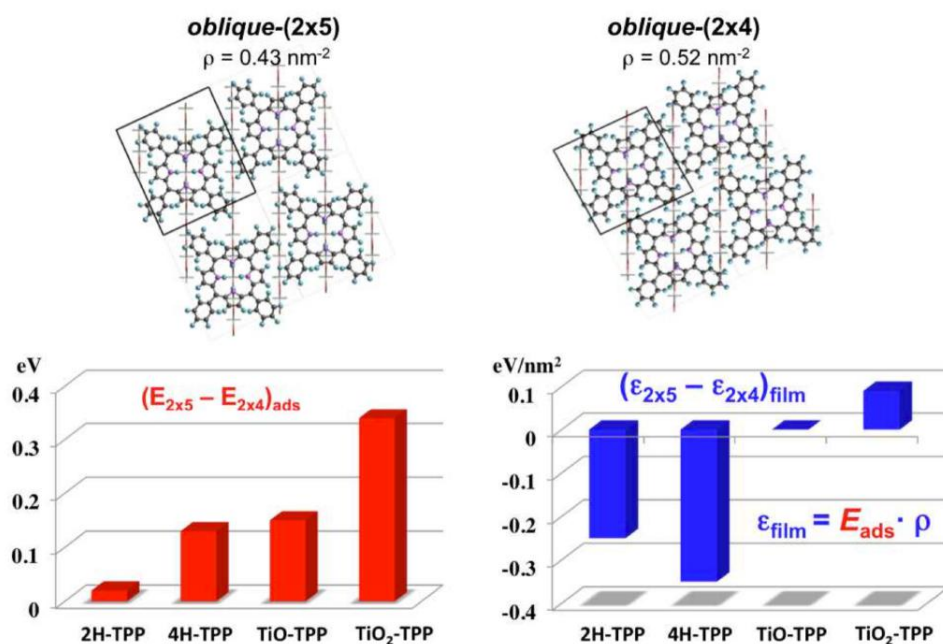


Fig. 4.34. (Up) Top view of the relaxed structure obtained for the o-(2x4) and o-(2x5) phases, the corresponding superlattice unit cell are indicated. All the molecules adsorb on the O_{br} rows on bridge sites for 2H-, 4H and TiO₂-TPP and on top for TiO-TPP. (Down) Comparison of the molecular E_{ads} and film ϵ_{ads} adsorption energies for the four porphyrin species in the two different phases. (Down left) Positive E_{ads} difference favours molecular adhesion in the o-(2x5); (down right) negative ϵ_{ads} difference favours the overall stability of the o-(2x4) phase.

Some of the most ordered domains seen when the thermal treatment reach 400°C can be ascribed to a $\begin{pmatrix} 0 & 2 \\ 6 & 0 \end{pmatrix}$ supercell, (r-(2x6)), choose as model. The density is about 0.452 nm^{-2} pretty like the one observed in the oblique-(2x5) phase. Considering that metalation occurs by a dehydrogenation of the macrocycle assisted by the abstraction of a Ti(5c) atom from

the surface, two models in which the molecules are on top of the Ti vacancy or displaced on top of a O(2c) ion bring that only the position over the O(2c) is stable by 1.7 eV, since the configuration over the Ti vacancy isn't a local minimum, and the Ti atom is captured back by the surface, forming simple dehydrogenated TPP species. In the optimized model, the Ti-TPP species are on top of the O(2c) atom in a saddle-shape configuration. The length of the Ti-O(2c) bond is 1.76 Å and the molecular axis is 5° azimuthal rotated respect to the [100] direction.

According with the calculus, the (2x6) phases display the same energetic behaviour as the previous o-(2x4) as expected. The absorption on-top an Obr atom is very close in energy to the adsorption between two adjacent Obr atoms, and bridge site is favored by 0.1-0.15 eV, because the optimal matching of the peripheral C-H terminations with the bridge sites at adjacent Obr rows (Fig- 4.35), being slightly favored the on-top site in the o-(2x6) phase.

The rectangular molecular configuration ascribed to the TiO₂TPP cyclo dehydrogenated is not compatible with the o-(2x4) phase because of the steric repulsion of the phenyls that overlaps for any azimuthal orientation of the molecules due to the molecular density. In order to complete the calculus, we performed some test on the o-(2x5) phase, that was reportedly observed for ZnTPP on TiO₂ (110) [X]. Even its density, the o-(2x5) phase can bear rectangularly flattened porphyrins azimuthal rotated by 30°, with 1 eV extra cost due to interactions with the surface. Such an azimuthal orientation would also be compatible with the oblique-(2 × 6) symmetry, but not with the rect-(2 × 6) one because of the head-to-tail overlap of consecutive molecules. However, at the monolayer saturation coverage, we have not observed any azimuthal deviation of the long molecular axis from a perfect parallelism to the substrate rows, not even beyond 450 °C, where local defects start to be formed either due to desorption or molecular decomposition. This confirms that the (2x4)→(2x6) transition is indeed triggered by the modified steric properties and binding capabilities acquired by the molecule upon cyclo dehydrogenation.

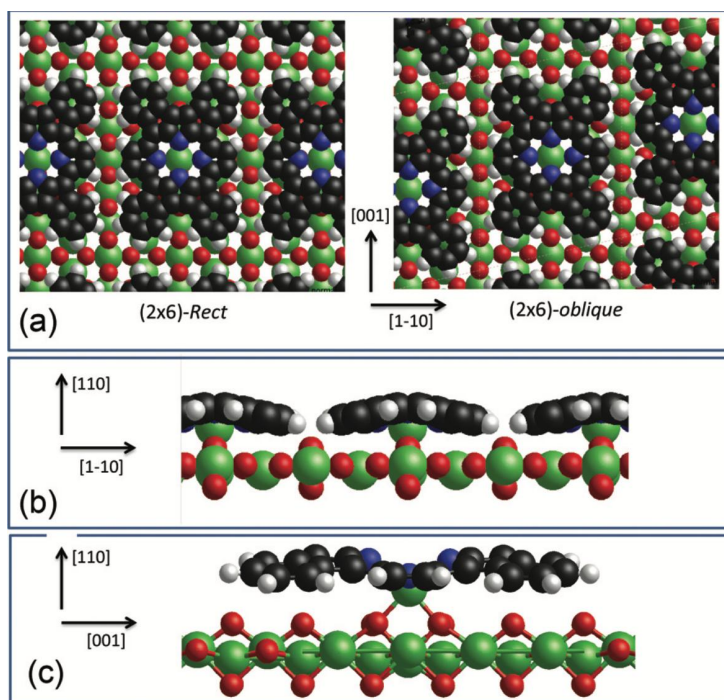


Fig. 4.35 DFT calculated adsorption configuration of cyclo-dehydrogenated TiO_2 -TPP. A) top view of the r -(2x6) and o -(2x6) phases. b) and c) side view of the molecule in the r -(2x6) highlighting the coordination between the porphyrin Ti and the surface Obr atoms.

The few calculations reported so far for metal-porphyrins on $\text{TiO}_2(110)$ have solely considered the adsorption of the central metal, either Ni(II) [74] or Cu(II) [75], on top of an Obr atom, thus preventing a direct comparison. Notably, the bridge site has been predicted to be largely favored by ~ 0.8 eV with respect to the on-top one for Co-porphyrin. Also in this tetra-pyridyl complex the adsorption configuration is mostly driven by its peripheral terminations, namely by the direct interaction of its two cyano ends with the Ti5f atoms of the adjacent rows[76]. Most importantly, none of the previous studies took into consideration steric constraints and intermolecular interaction, which cannot however be neglected since they determine the molecular arrangement and orientation within compact domains as demonstrated.

The comparison between calculated DOS profile and STM measurements of individual

molecules for the two absorption sites (on bridge and on top O_{br} rows), that cannot be simply discriminated from the analysis of topographic images, shown that rectangular shape of the molecules can be clearly appreciated in STM (Fig. 4.36) for positive and negative bias, with four circular spots can be appreciated at the molecular corners, displaying a characteristic “X” appearance. Looking in detail, both adsorption sites yield very similar DOS profiles, with less pronounced nodal plane of the inner macrocycle in the on top site. The on top site yields a larger lateral extent of the fine structure with respect to the on bridge one.

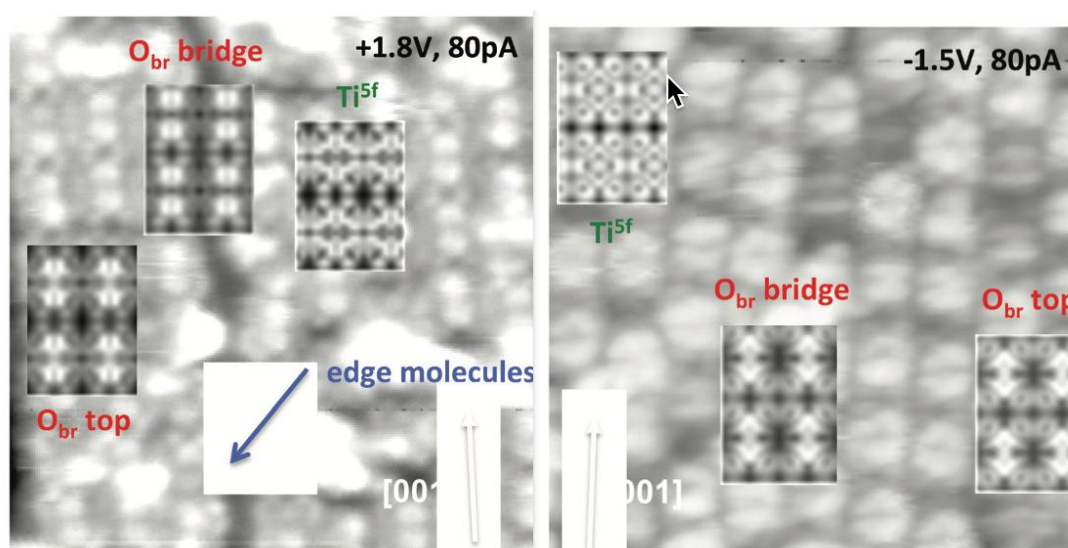


Fig. 4.36 Comparison between DOS cuts (4 molecules in a 4×12 cell size) at constant energy and STM topographic images at positive (top) and negative (bottom) sample bias. In the simulation, we considered dehydrogenated titanium(IV)-porphyrin at both on-bridge and on-top O_{br} atoms, as well as atop Ti^{5f} atoms. For better comparison, we spatially average the DOS cuts over a mean radius of 1 Å.

The profile for the TiOTPP cyclo dehydrogenated adsorbed with its oxygen atom atop a Ti^{5f} atom, resulting in a vertically stacked Ti-O-Ti^{5f} geometry was also calculated. The molecular

backbone has the same rectangular flat structure and azimuthal orientation of those adsorbed atop the O_{br} rows. This configuration (Fig. 4.36) yields a completely different DOS profile. There is a complete mismatch of the main features associated with the inner macrocycle, from which we can safely discard these model.

The different appearance of the lateral structure (associated with the aromatic carbon backbone) in the calculated DOS profiles atop the O_{br} rows is due to the molecular conformation being flatter in the on-top site than in the on-bridge one.

The last case presents its backbone symmetrically bent towards the surface with respect to the O_{br} rows, due to the network of peripheral $C-H\cdots O$ bonds, thus resulting in an overall fainter and narrower extent of the lateral structure. In this regard, we remark that molecules adsorbed at the edge of deep troughs clearly display a larger extension of the lateral structure spreading above the trough. These edge molecules closely resemble the DOS profile of the on-top fully flat molecule (Fig. 4.36), whereas the lateral spread is much more limited in between adjacent molecules within a (2×6) domain. This is in full agreement with the predicted structural origin (hogback bending) of the molecular contrast outside the macrocycle.

Unfortunately, we achieved a reasonable intramolecular resolution only on images taken after annealing to 450–500 °C, where the surface displays the coexistence of misaligned (2×6) rows and multiple defects due to the onset of film degradation, thus hampering a deeper topographic analysis of the fine structure at the molecular edges.

However, (i) the pronounced nodal plane, which is ubiquitously observed at any STM contrast and length scale in the (2×6) phase domains, and (ii) the closer resemblance of the corresponding inner macrocycle features at positive bias (Fig. 4.36) favor the on-bridge adsorption site atop the with the proposed TiO_2TPP cyclo-dehydrogenated molecular structure.

Finally, considering the models a sketch of the temperature evolution of the monolayer saturation phase of 2HTPP on the rutile TiO₂(110) can be drawn (Fig. 4.37). While the same molecular ordering is preserved across the self-metalation reaction, partial molecular desorption takes place upon cyclo-dehydrogenation decreasing the molecular density of the saturated monolayer from 0.52 to 0.43mm⁻². The invariance of azimuthal orientation and molecular absorption site across the two chemical reactions and in the four different chemical states is remarkable.

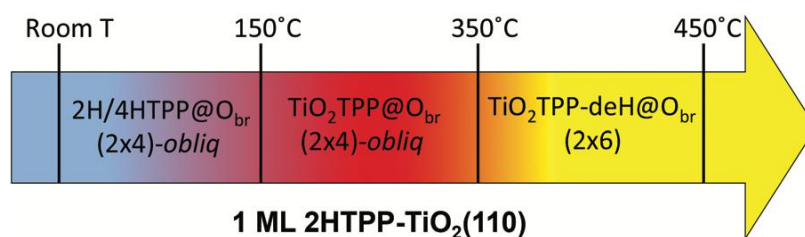


Fig. 4.37. Phase diagram of free-base TPP on TiO₂ (110) at 1ML saturation coverage. No molecular ordering on a long range length scale takes place below RT due to limited surface mobility.

4.4. PHTHALOCYANINES: 2H-PC AND TiO-PC

This molecule is composed by four pyrrole subunits, held together by nitrogen meso- linkers, forming the macrocycle. The pyrroles are modified by cleavage of two C-H bonds, followed by the addition of four sp² carbon atoms to give four coplanar isoindole groups. The molecular flexibility is enhanced by the additional degree of freedom available due to the isoindole moieties rotation capability about the outer C-N bonds.

Due to its similarity and differences with the porphyrins base molecules the study of Phthalocyanines is interesting for comparison.

4.4.1. SPECTROSCOPY CHARACTERIZATION: XPS AND NEXAFS

The molecule presents three chemical inequivalent N species, meso nitrogen, welding the four isoindole moieties, and the aza and pyrrolic nitrogens located at the internal part of the macrocycle. The pyrrolic nitrogen is bound to one hydrogen atom, while the aza and the meso are bounded to two carbon atoms each.

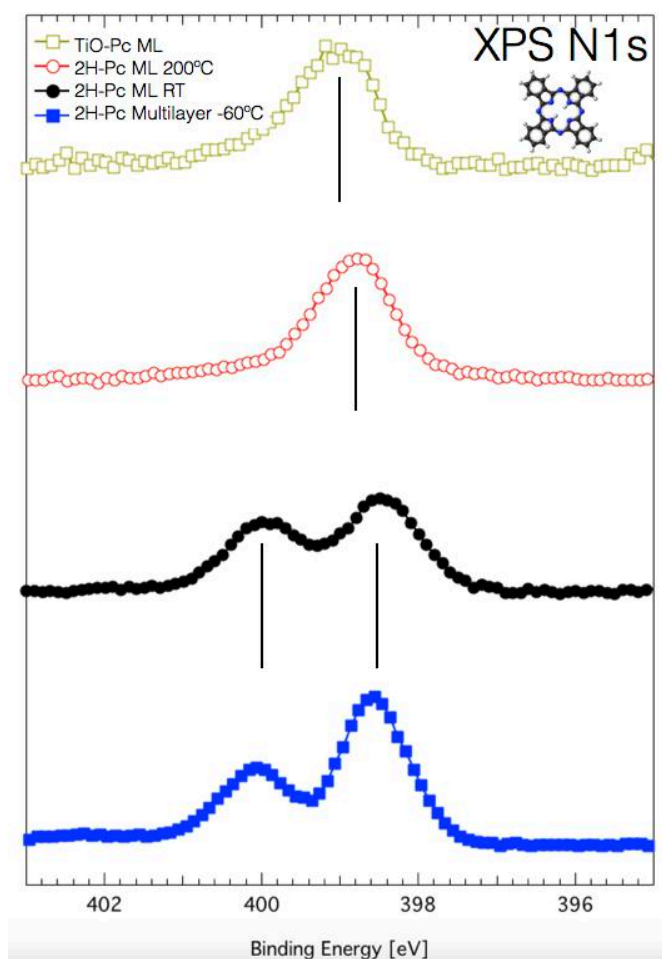


Fig. 4.38 XPS from N1s comparison between multilayer, monolayer, and monolayer annealed for 2H-Pc and monolayer of TiO-Pc.

The Fig. 4.38 shows the N1s spectrum of three different films of free-base phthalocyanines evaporated in UHV on rutile-TiO₂(110). The evaporation of a multilayer shows two separated peaks at 398.6 eV and 400.0 eV from the meso- and aza- nitrogen atoms and the pyrrolic nitrogen atoms respectively. The intensity ratio is 1:3, according with the stoichiometry of pristine free-base porphyrins, where the 4 meso- nitrogens have a binding energy almost coincident with that of the two aza-nitrogens.

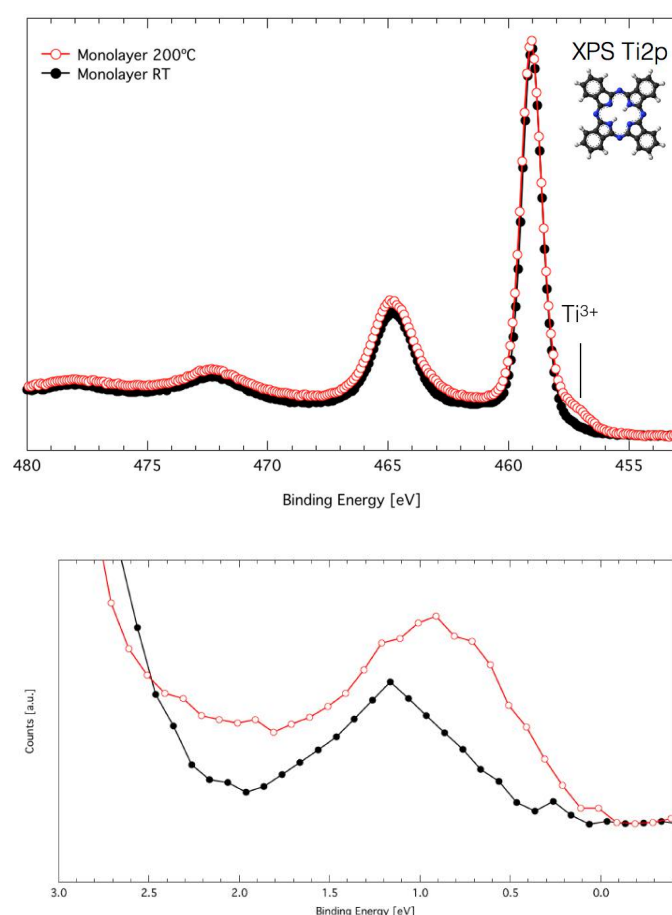


Fig. 4.39. (up) Ti 2p XPS peaks measured with 650 eV photon energy from a monolayer of 2H-Pc as deposited and after thermal treatment. Spectres aligned to the Ti 2p_{3/2} (~459.1 eV). (down) valence band defect state detail XPS spectra at 140 eV. Spectres aligned and normalized to the Ti 3p (~37.5 eV).

The evaporation of a monolayer instead give us a different behaviour, where the stoichiometric ratio at room temperature rather approaches the value of 1:1 only observed by deposition at low temperature ($<30^{\circ}\text{C}$), since at room temperature the ratio is in the range of 1:1.5 or 1:2, either because the molecule starts metalation or because they start to lose hydrogen at meso- atoms. The thermal treatment of the monolayer at 200° causes the disappearance of the pyrrolic component, with an increase in the remaining component that shifts to 398.8 eV. This conversion is almost completed at lower temperature ($\sim 90^{\circ}\text{C}$). As seen the deposition of a monolayer of metal porphyrins (i.e. TiO-Pc) shows a single peak at similar B.E. (399.0eV) suggesting the self-metalation with Ti substrate atoms as direct explanation of this change.

In Fig. 4.39. the behaviour of Ti2p is shown during the thermal treatment and the consequent metalation. The oxidation state of titanyl-phthalocyanine is Ti^{4+} like the TiO_2 , but the increase of the Ti^{3+} shoulder suggest some impaired titanium atoms in the substrate after metalation. This hypothesis is supported by the increase of the defect state.

The pyrrolization of nitrogen on free-base phthalocyanines on rutile- $\text{TiO}_2(110)$ has already been reported in the literature [77], without conclusive explanation.

Performing NEXAFS measurements on the experiment, as seen in the Fig. 4.40. the spectrum at RT replicates the multilayer one [77], confirming that the molecule monomer adsorbs intact. The most intense peak 2 is assigned to excitation of the 1s electrons on the phenyl rings into a π^* unoccupied orbital, LUMO+1 [77], and the π -symmetry contributions from multiple C sites distributed on the macrocycle originate the lowest energy peak 1, LUMO. Their intensity ratio is similar to the multilayer, suggesting a weak coupling with the substrate. There is a pronounced dichroism in the main π -symmetry resonances. Fitting peaks 1 and 2 the molecular tilt angle can be estimated, being about 18° at LT ($\sim 100^{\circ}\text{C}$) and 28° at RT from the $[1\bar{1}0]$ direction. This decrease in the π dichroism that is also seen in the annealed layer that shows similar behaviour than the RT (also the calculated tilt angle is about 28°), is according with the metalation hypothesis since the metalloporphyrins show little dependence on the type of chelated metal ion [78, 79]. This homogeneous dichroism is

likely due to a distortion not limited to specific subunits but affecting the four isoindoles since the pocket incorporates the Ti atom, rather than a tilt of the whole molecule. Since no functional groups prone to making chemical bonds with the surface are present in the external edge of the molecule, it can adsorb tilted. At LT instead the dichroism is ascribed to some second layer molecules deposited over the already covered 2H-Pc, favoured by the temperature, or to the adoption of a close-packed structure [80] where the tendency of the molecules to maximize the hybridization of the extended π system with the substrate is opposed by the high surface corrugation, leading a small molecular tilt angle about the protruding oxygen rows.

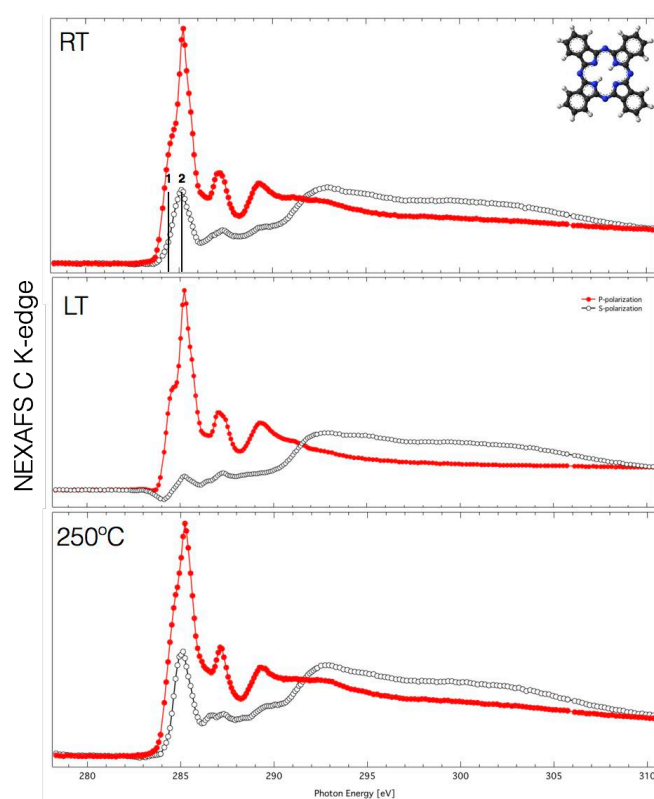


Fig. 4.40. 2H-Pc sub-monolayer over rutile-TiO₂(110) (1x1) Carbon K-edge polarized NEXAFS. The spectra have been normalized to the absorption measured on the clean TiO₂(110) surface.

4.4.2. FILM STRUCTURE DETERMINATION: STM

The phthalocyanine sub-monolayer deposition STM measurements are shown in the Fig. 4.41. At room temperature, the molecules present a four lobes contrast with intensities, that are adsorbed over the Ti(5c) or O(2c) depending on the azimuthal orientation of the lobes. When the molecules adsorb on the Ti(5c) rows it seems to align two opposite phenyls along them. When the molecule adsorbs at the O(2c) rows, they are azimuthally rotated by 45°. The tip is changing during the measurements due to the interaction with diffusing molecules that present weak substrate coupling and prefer to attach to the tip, changing its behaviour.

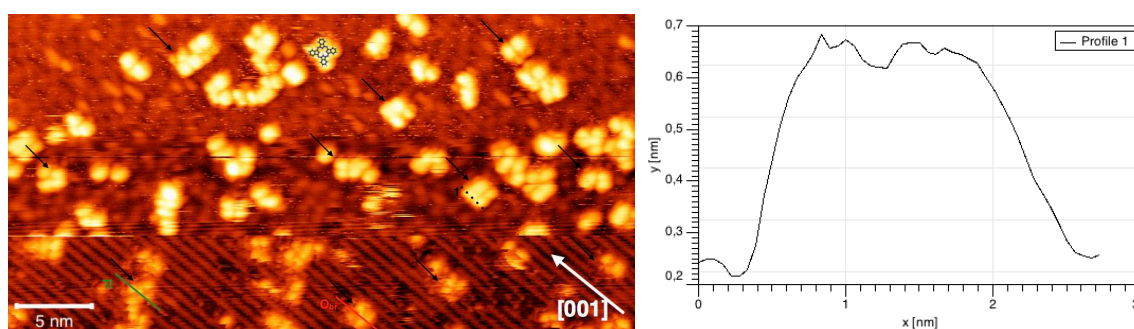


Fig. 4.41. (up) 2H-Pc submonolayer deposited at RT over rutile-TiO₂(110) (1x1). (down) molecule profile along 1.

After thermal treatment at the metalation temperature, the molecules are less reactive with respect to the tip, and even if it's not too obvious what is a molecule due to the clusters formed by their aggregates, again the four lobes structure can be recognized as seen on Fig. 4.42.

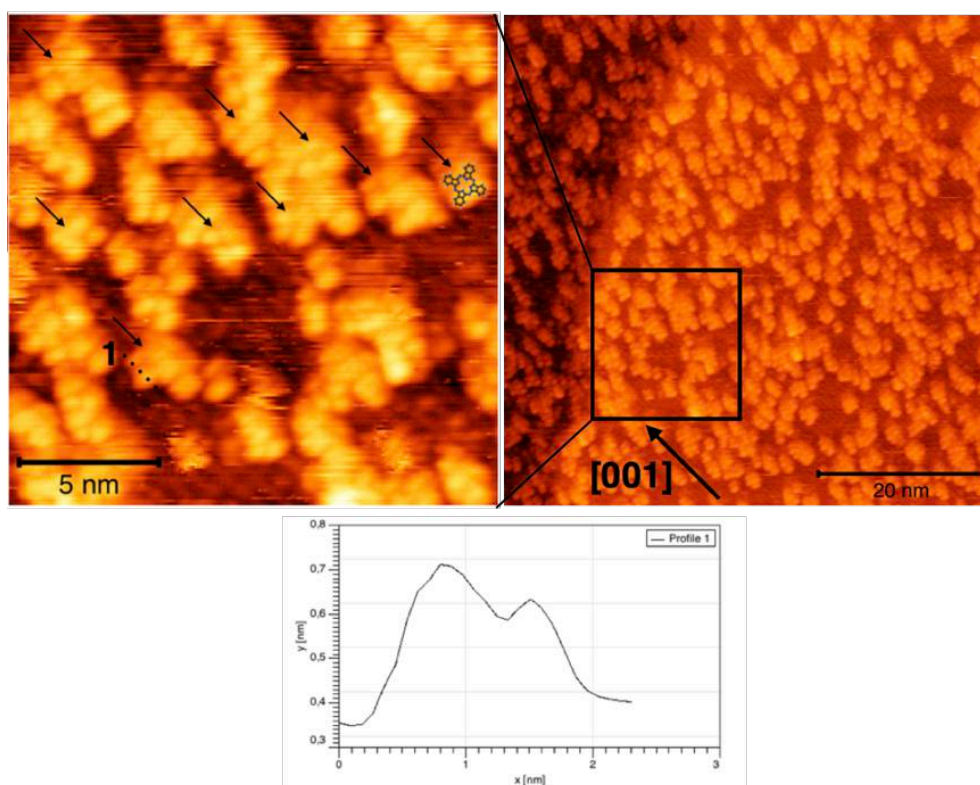


Fig. 4.42. (up-right) Annealed 2H-Pc submonolayer over rutile-TiO₂(110) (1x1). (up-left) detail from the black squared region. (down) profile along 1 from a single molecule. Bias=1.96V, Tunneling Current= 7.5pA.

For comparison TiO-Pc molecules were evaporated over TiO₂(110) in Fig 4.43., showing the characteristic four lobes structure without any special feature or intensity inside the pocket, and oriented according with the annealed ones, even if the lines cannot be distinguished on the measurements.

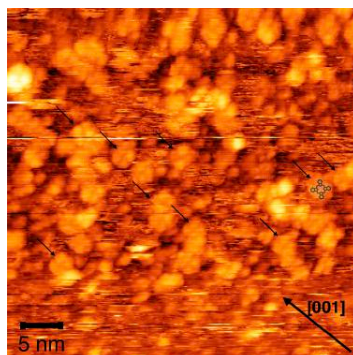


Fig. 4.43. TiOPc sub-monolayer over rutile-TiO₂(110) (1x1). Bias=-1.55V Tunneling Current=17pA

4.4.3. 2H-PC THEORETICAL APPROACH

Eight adsorption configurations were studied using a supercell for a single phthalocyanine molecule with three and four TiO₂ layer slabs, each containing 120 atoms in a c(10x4) area. Four adsorption sites (i.e. on top on a bridging O or a five-fold Ti atom, and bridge between two bridging O or two five-fold Ti atoms, and two azimuthal orientations following the symmetry of the surface and the molecule, with the virtual line crossing the opposite phenyls at 0° and 45° respect to the [001] direction).

The adsorption energy is estimated as

$$E_{ads} = E(ads) + E(slab) - E(ads + slab) \quad (4.1)$$

The results demonstrate that the molecule doesn't display a strongly preferential adsorption site, with a very low difference about 0.06eV between the two most stable configurations: i) adsorbed above Ti rows on "bridge" with the phenyls line aligned along the [001], or ii) on

top of the O rows azimuthal rotated 45°, as seen on the Tab. 4.2. The other six configurations present lower adsorption energies by about 0.2eV. The distance between the molecular plane and the substrate plane (i.e. average value of z between five-fold Ti and bridging O ions) is about 3.65 Å on the Ti(5c) rows and 3.61 Å on O(2c) rows.

Two type of hydrogenations have been also considered in the two most stable configurations: the aza-N hydrogenation and the meso-N hydrogenation. In both cases the Hydrogen prefer the meso-N atoms, with the minimum energy corresponding to the 4H-Pc rotated by 45° adsorbed on top of O(2c). The energy of the hydrogenation formation was also calculated, considering the conversion of two meso-N atoms into pyrrolic-N atoms by uptaking two H atoms from OH surface defects, giving an energy gain of 0.49eV. This process is exothermic, so free-base phthalocyanine can easily remove two H atoms on the surface, according with the hydrogenation hypothesis.

Molecule	Configuration	E _{ads} [eV]
2H-Pc	0°, Ti row, bridge	2.25
2H-Pc	45°, O row, on-top	2.19
4H-Pc	45°, O row, on-top	3.95

Table. 4.2. Adsorption energy of phthalocyanine on rutile-TiO₂(110) surface.

5. INTERMOLECULAR COUPLING. DONOR/ACCEPTOR STACKING ON TiO₂

5.1. FULLERENE: C₆₀

Fullerenes are an allotropic carbon form and C₆₀ is one of the most representative ones composed by 60 carbon atoms in a spherical shape with a van der Waals diameter of 11Å formed by 20 hexagons and 12 pentagons, surrounding an empty cavity, as seen on Fig 5.1. Each carbon atom has three first neighbour carbon atoms forming two single bonds and one double bond. The consequent hybridization is like the graphite one, three sp² orbitals on the surface and one π -symmetry perpendicular. This hybridization has a minimum energy in a planar configuration, so fullerenes are subdued to an angular stress due to its curvature being stable but not inert. This molecule satisfies the Euler theorem, where twelve pentagons are necessary to close a curve structure form by n hexagons. Moreover, the pentagons are not neighbours, satisfying the isolated pentagons rule [81]. The C₆₀ is the smallest molecule that satisfies both conditions.

Its ionization energy of an isolated C₆₀ molecule is 7.6 eV, and the electron affinity is 2.65 eV; thus, the molecule is expected to be an electron acceptor [82]. The combination of donor polymers with acceptor fullerenes has been exploding in solar cells for light harvesting [83] as one of the most viable exploitation. When deposited on metals, C₆₀ molecules form a well-ordered structure, where molecules are physisorbed on the surface with a mean separation corresponding to the van der Waals diameter [84]. This means that the interaction with the surface is small, but substrate still lock the molecular orientation.



Fig. 5.1. Molecular model for fullerene C₆₀ purpose by Kroto et al. in 1985 [85].

The deposition over rutile-TiO₂(110) 1x1 gives rise to compact islands growing from the step edges, indicating a weak interaction with substrate atoms on terraces. The molecules adsorb on top of the five-fold Ti rows, in a p-(5x2) phase, seen in the STM topography, and LEED pattern [86].

The deposition of C₆₀ can be easily tuned by He diffraction, shown in Fig. 5.2., where the specular intensity linearly drops to a minimum steady value that remains invariant by further deposition, indicating an increase of the disorder (i.e. static or dynamic) when the surface is fully covered by C₆₀. In absence of oscillation of the reflectivity, the formation of a single layer when the minimum reflectivity is reached can be assumed.

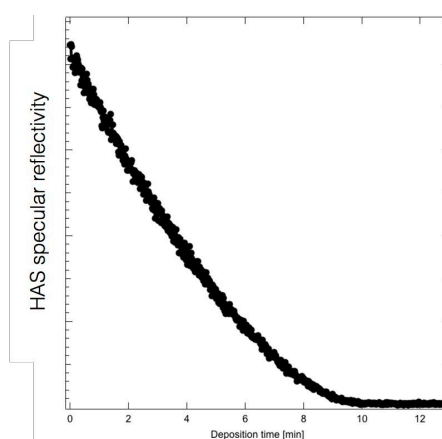


Fig. 5.2. He atom specular intensity during C₆₀ deposition over rutile-TiO₂ at RT.

5.2. TiO-Pc, 2H-TbTPP AND C60 INTERACTION

All the experiments performed aim at modelling archetypal hybrid interfaces for optimal charge transport or intermolecular coupling via templated growth or direct molecular self-assembly into hierarchically ordered networks. With this purpose, the molecular order at the interface with the electrode is important and, if perturbed, contact resistance would increase according with a poor energy level alignment attenuating the charge transport properties of the system. Several progresses in the 2D D/A supramolecular architecture have been achieved, demonstrating that the lateral interaction between complementary molecules modifies the coupling with the substrate, shifting the HOMO and LUMO states, and the height of the molecule over the surface that affects the local charge transfer properties [87, 88]

To understand the interaction between layers of different species and with the substrate, a well-known fullerene as C60 and a self-metalated porphyrin with a TiO metallic core have been deposited in two different conformations, Donor/Acceptor and Acceptor/Donor, to disentangle the molecule-molecule or molecule-substrate behaviour and their strength. UPS measurements have been done for electronic characterization of this bilayer systems, using a He discharge UV-lamp in the He I range (Photon energy of 21.2 eV). The ultraviolet radiation has high photo-electron cross-section in the valence band region, and its photoelectron energy has very low photoelectron escape depth, becoming surface sensitive and convenient if the systems are contaminants absent.

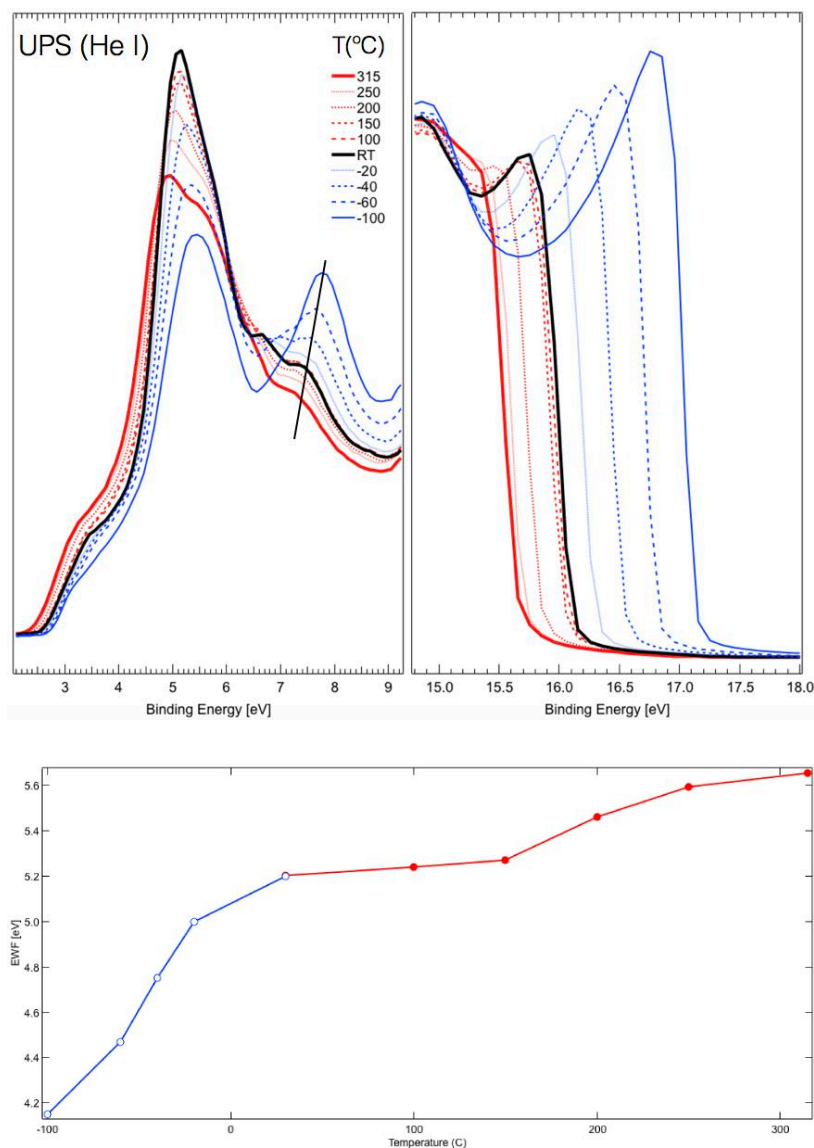


Fig. 5.3. (left) UPS valence band spectra from rutile-TiO₂(110) under thermal treatment. (right) Detail of the secondary cut-off. (down) Surface work function evolution.

In the Fig. 5.3. the valence band on the clean rutile-TiO₂(110) under thermal treatment is shown. The surface work function (EWF) present a non linear behaviour in contrast with that predicted for metallic surfaces [89].

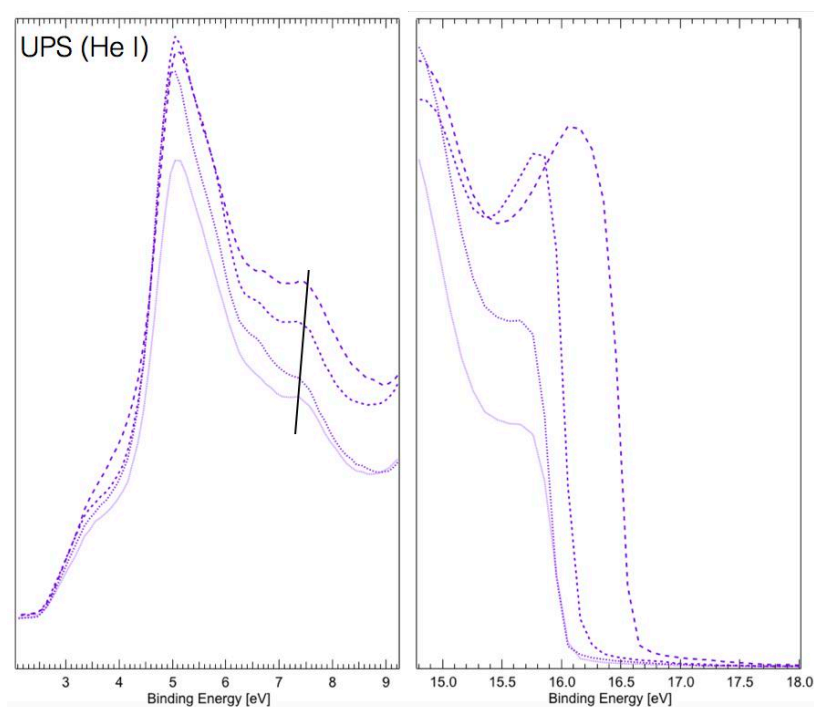


Fig. 5.4. UPS valence band spectra for different clean rutile-TiO₂ surface preparations during the experiments. The defects evolution is not chronological.

The measurements performed in the clean rutile-TiO₂ surfaces prepared by sputtering and annealing cycles as described in 5.4., give us a similar behaviour, that looks to depend strongly on the contaminants over the surface, mainly water, since the defects state remain mostly constant and doesn't evolve parallel.

The valence band spectroscopy from the monolayers of the three species shown in the Fig. 5.5. comparison with the multilayers, demonstrate that the all of them present small substrate interaction by themselves, with all the features that can be ascribe to the different HOMO levels, at similar energies with negligible shifts [90]. In the table 5.1. the shifts in the energy for the secondary cut-off from the different species in monolayer and multilayer depositions refer to the respective clean surface in which the deposition took place are summarized. All the spectres have been aligned with respect to the defect state from the clean surface according with literature [91].

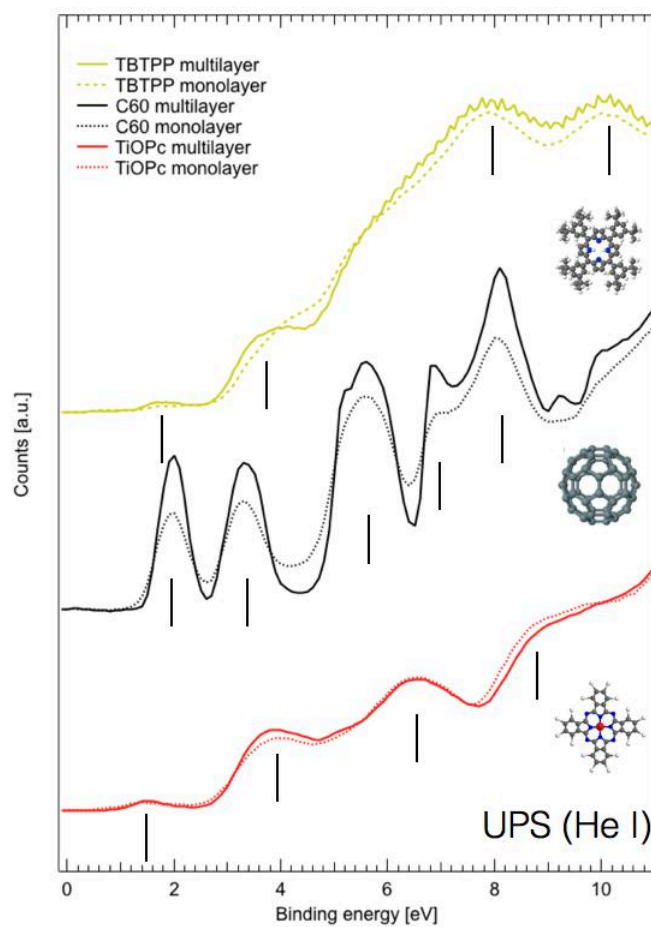


Fig. 5.5. UPS valence band for C60, 2H-tbTPP and TiO-Pc, deposited over rutile-TiO₂ in the monolayer and the multilayer conditions. The TiO-Pc monolayer condition was achieved by thermal desorption of the multilayer.

Molecule	Monolayer	Multilayer
2H-tbTPP	-0,42 eV	-1,10 eV
TiO-Pc	-0,78 eV	-0,67 eV
C60	+0,11 eV	-1,02 eV

Table. 5.1. EWF shifts for the different coverage of the three studied species over rutile-TiO₂(110).

Focusing on the Fig 5.6. from the co-deposition of TiO-Pc over C60, a shift about 0.2 eV is seen on the HOMO and HOMO+1 from the molecule. In the defect states region, the signal from the defects (peak 1) is completely quenched by C60 deposition with the appearance of a new peak at about 3 eV (peak 3) present also in the C60 multilayer that completely disappears under TiO-Pc deposition, where the TiO-Pc HOMO is predominantly seen (peak 2), that corresponds to the HOMO of C60 originated by the component of He I_B line at 23.09 eV. This is an expected behaviour due to the signal screening for the electrons mean free path, where each layer is deposited intact over the previous.

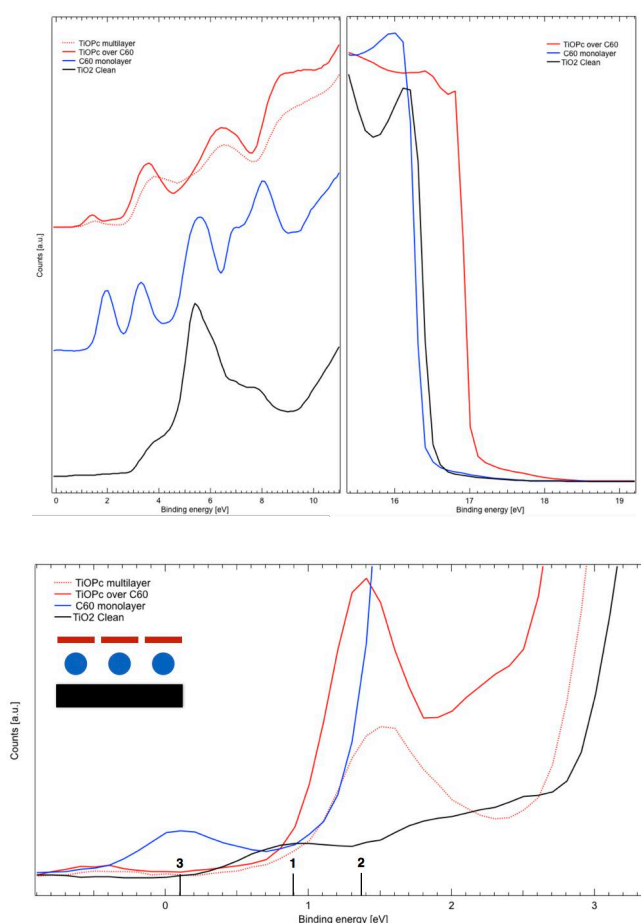


Fig. 5.6. UPS valence band spectroscopies (He I) from a deposition of C60 monolayer over clean rutile-TiO₂ at RT followed by deposition of TiO-Pc monolayer.

In the Fig. 5.7. from the co-deposition of C60 over TiO-Pc, a big shift about 0,66 eV in the C60 HOMOs is seen. The defect state region, shows the quenched HOMO from TiO-Pc (peak 2) under C60 deposition, and the reappearance of the defect state (peak 1) with higher intensity. The origin of this peak would be checked by RESPES at the C, N and Ti edges. Under annealing at 200°C the profile turns to the TiO-Pc deposition conditions unambiguously, due to the desorption of the C60 layer (results not shown). On this vertical stacking conditions, the interaction of the first layer with the substrate is larger than the molecule-molecule interaction, dominated by the donor coupling to the substrate.

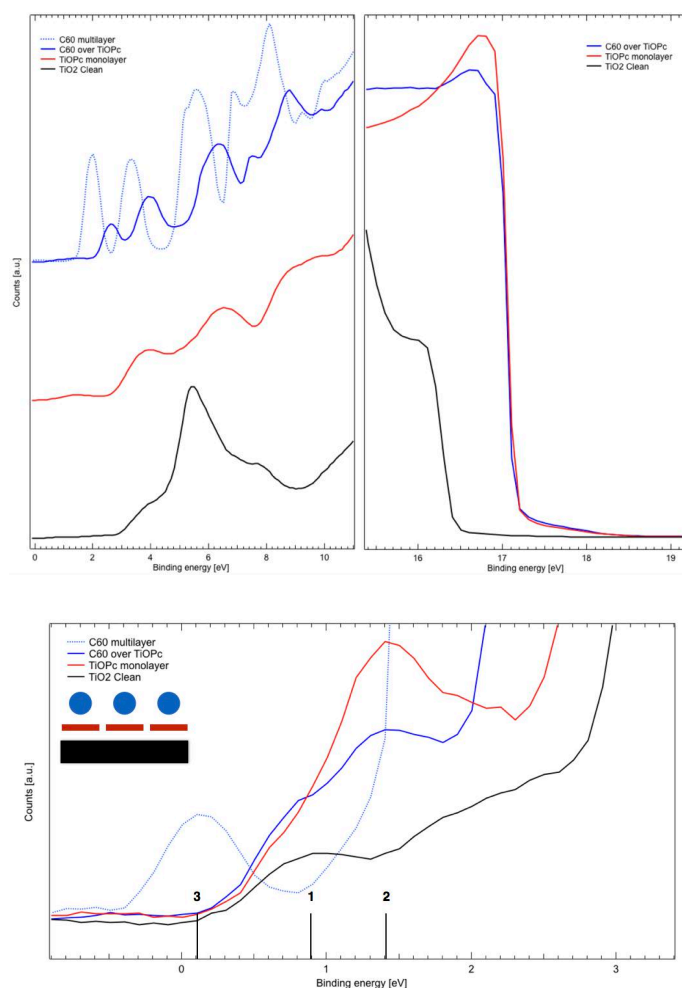


Fig. 5.7. UPS valence band spectroscopies (He I) from a TiO-Pc monolayer form by multilayer desorption over clean rutile-TiO₂ followed by deposition of C60 monolayer.

The co-deposition layer by layer of TiO-Pc and C60, in two opposite sequences, shows that the effect on the secondary cut-off produce by the C60 deposition is negligible since the TiO-Pc reduces the work function by 0.55 eV when deposited over C60 monolayer as seen on Fig. 5.6. and 0.78 eV when direct deposited over the clean substrate shown on Fig. 5.7. The alignment according with the photon energy (i.e. He I $h\nu = 21.22$ eV) and the applied bias (-20 eV) was selected for these representations.

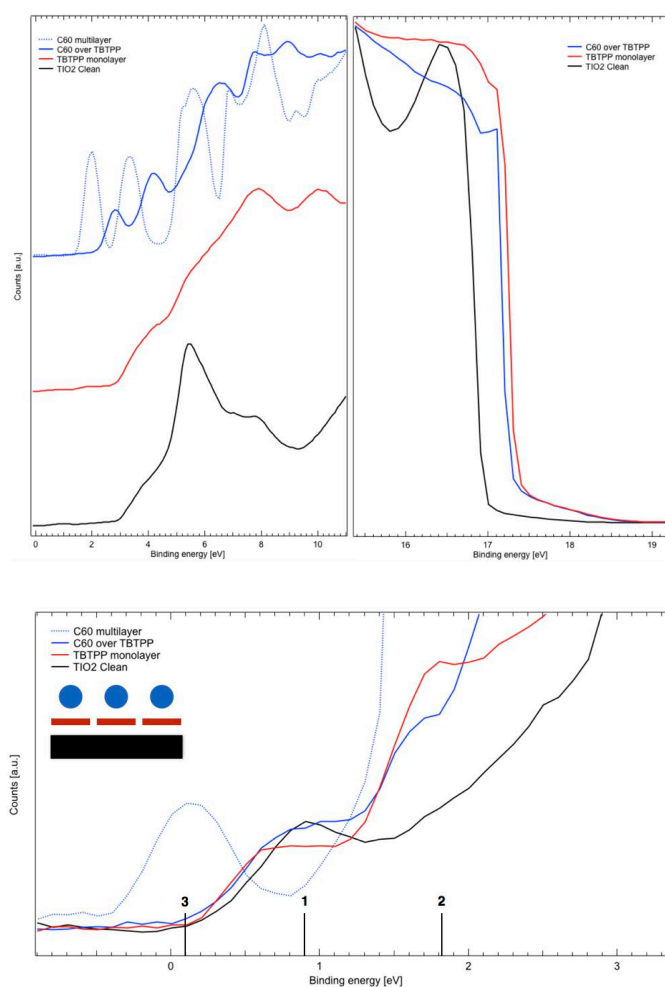


Fig. 5.8. UPS valence band spectroscopies (He I) from a deposition of 2H-tbTPP monolayer over clean rutile-TiO₂ at RT followed by deposition of C60 monolayer

In the Fig. 5.8. the co-deposition of C60 over 2H-tbTPP is shown. A decreasing about 0.42 eV in the work function ascribed to the 2H-tbTPP deposition remains invariable under C60 deposition, where the entire HOMOs peaks are shifted by 0,86 eV.

In the defect states region, the deposition of 2h-tbTPP smooths the defect states signal (peak 1) that shifts -0.1 eV and the intensity is recovered under C60 deposition, keeping the shifted position. These changes might be due to the formation of clusters and the consequent exhibit of the surface, respectively.

The shift of the HOMOs from the C60 as second layer added to the negligibly influence in the secondary cut-off open the possibility to use this technique to tune the energy level alignment, at organic/semiconductor interfaces [92]

6. CONCLUSIONS

We dealt with the issues of self-assembly and on-surface chemistry of organic semiconductors on the metal oxide surface rutile-TiO₂(110), considering the following molecular species: i) four free-base heterocyclic molecules: tetraphenyl-porphyrin (2H-TPP), octaethyl-porphyrin (2H-OEP) and tert-butyl tetraphenyl-porphyrin (2H-tbTPP), and ii) one carbon allotrope: the fullerene C₆₀.

XPS measurements performed on the free-base heterocyclic molecules, where twice the suggested stoichiometry for the pyrrolic- N atoms in 2H-Pc monolayer evaporated on rutile-TiO₂, and a single N1s peak was probed corresponding to the pyrrolic binding energy for the free-base porphyrins (2H-TPP, 2H-tbTPP and 2H-OEP), putting in evidence a common hydrogenation of their meso- or aza-nitrogen atoms in the macrocycle. The quenching of the OH valence band peak, the simulations and the energetic barrier for the hydrogen uptaking from the bulk is in complete agreement with this hypothesis. The peripheral substituents and macrocycle nature in the different heterocyclic molecules, affects instead the energy barrier for self-metalation, with the predominance of the 2H-Pc since its absorption is almost planar, favouring the self-metalation even at room temperature.

Focusing our research into tetraphenyl-porphyrins, the observed phase formed with high density coverage (about the monolayer) presents a oblique(2x4) symmetry, that correspond with the densest monolayer porphyrin packing according with DFT simulations, formed by molecules adsorbed on a bridge site between two Obr atoms on its three chemical states, 2H-TPP, 4H-TPP, TiO₂-TPP below 350°C. This phase is irreversible transform into a (2x6) symmetry phase beyond 350°C, driven by partial dehydrogenation of the phenyl terminations and formation of new aryl-aryl carbon bonds, which flatten the molecule in rectangular structure, preserving the aromaticity of the tetrapyrrolic macrocycle. This phase transition supposes the partial desorption of about 20% molecules, maintaining the adsorption site and molecular orientation of the original free-base porphyrins and simply metalated ones, on bridge site between two Obr atoms parallel to the substrate [001] direction. The central Ti atoms preserve the same oxidation state as the substrate Ti atoms. Calculus predict that in the bare self-metalation is slightly intrinsic stable (70meV) the on top site adsorption,

but molecules remain in the on-bridge site because the steric constraint due to the intercalation of tilted phenyl rings among adjacent molecules. In the monolayer self-metalation, calculations unambiguously predict a larger stability of the on-bridge site (0.10-0.15eV) respect to the on top one. Consequently, even if molecular displacement is allowed, the molecules does not move to the now lesser stable on top site.

The very high thermal stability of the ordered contact layer of self-metalated porphyrins on rutile-TiO₂(110), quite unexpected, can be rationalized not only in comparison with the instability of the porphyrin monolayer on metals but also for the general properties of the substrate, that might be regarded as a catalytic surface favouring molecular decomposition and as a dielectric favouring molecular desorption. This stabilization take profit of both properties. The molecular anchoring is driven by a strong bonding of the tetrapyrrolic macrocycle to the Obr rows in whatever chemical state (2H-TPP, 4H-TPP, TiO₂-TPP and TiO₂-TPP cyclo-dehydrogenated), keeping the molecules in registry with the substrate and preserving the long order across chemical transformations. The phenyl terminations by itself manifest a purely vdW interaction with the substrate without any significant charge transfer into the π^* unoccupied orbitals. Consequently, despites the molecular rigidity after the self-metalation, temperature can be increased as high as the dynamical rotation of the phenyl rings can bring them down with a frequency large enough to trigger the cyclo-dehydrogenation reaction and the aryl-aryl carbon bond, without polymerization or decomposition.

Last issue was the layer-by-layer deposition of donors and acceptors vertical mixed layers on rutile-TiO₂ as inert template. The interaction between molecular layers is weaker than with the substrate, desorbing eventually the topmost layers by thermal treatment as in the C60 monolayer over TiO-Pc monolayer. The donor layer (TiO-Pc and 2H-tbTPP) affects the behaviour of the acceptor HOMOs, shifting them to larger binding energies, and opening a new channel to tune the energy level alignment at the organic/dielectric interfaces.

REFERENCES

1. A. Safiei, J. Henzl, and K. Morgenstern. *Isomerization of an azobenzene derivative on a thin insulating layer by inelastically tunneling electrons*. Phys. Rev. Lett., 104:216102, 2010.
2. J. Repp, G. Meyer, F. E. Olsson, and M. Persson. *Controlling the charge state of individual gold adatoms*. Science, 305(5683):493–495, 2004.
3. C. Reese, M. Roberts, M. Ling, and Z. Bao. *Organic thin film transistors*. Materials today, 7(9):20–27, 2004.
4. F. Mohn, L. Gross, N. Moll, and G. Meyer. *Imaging the charge distribution within a single molecule*. Nature nanotechnology, 7(4):227–231, 2012.
5. J. Repp, G. Meyer, S. Paavilainen, F. E. Olsson, and M. Persson. *Imaging bond formation between a gold atom and pentacene on an insulating surface*. Science, 312(5777):1196–1199, 2006.
6. C. Klauber. *UHV Basics*. In D. J. O'Connor, B. A. Sexton, and R. S.C. Smart, *Surface Analysis Methods in Materials Science*. Springer, 2003.
7. C. J. Chen. *Introduction to Scanning Tunneling Microscopy*. Oxford University Press, 1993.
8. G. Binnig and H. Rohrer. *Scanning tunneling microscopy*. Surface Science, 126(1-3):236–244, 1983.
9. J. Bardeen. *Tunneling from a Many-Particle Point of View*. Phys. Rev. Lett., 6(2):57, 1961.

10. A. Gottlieb and L. Wesoloski. *Bardeen's tunneling theory as applied to scanning tunneling microscopy: a technical guide to the traditional interpretation*. Nanotechnology, 17(8):R57, 2006.
11. S. Hüfner. *Photoelectron Spectroscopy, Principles and Applications*. Springer, 2003.
12. K. Oura, M. Katayama, A. V. Zotov, V. G. Lifshits, and A. A. Saranin. *Surface Science: An Introduction*. Springer, 2003.
13. J. Stöhr. *NEXAFS spectroscopy*. Springer-Verlag, 1992.
14. J. Stöhr and D. A. Outka. *Determination of molecular orientations on surfaces from the angular dependence of near-edge x-ray-absorption fine-structure spectra*. Phys. Rev. B 36(15) 7891, 1987.
15. J. Klein, *Epitaktische Heterostrukturen aus dotierten Manganaten*, PhD Thesis, University of Cologne, 2001
16. T. Sakamoto, N.J. Kawai, T. Nakagawa, K. Ohta, T. Kojima, G. Hashiguchi, *Rheed intensity oscillations during silicon MBE growth*, 174 (1–3), 651-657, 1986.
17. J. Fassbender, U. May, B. Schirmer, R. M. Jungblut, B. Hillebrands, and G. Güntherodt, *Oscillatory Surface In-Plane Lattice Spacing during Growth of Co and of Cu on a Cu(001) Single Crystal*, Phys. Rev. Lett. 75, 4476, 1995
18. P.K. Larsen and P. J. Dobson, *Reflection High-Energy Electron Diffraction and Reflection Electron Imaging of Surfaces*, Series B: Physics 188, 1987
19. P.A. Maksym, J.L. Beeby, *A theory of rheed*, Surface Science, 110 (2), 423-438, 1981.
20. L. Floreano, G. Naletto, D. Cvetko, et al., *Performance of the grating-crystal monochromator of the ALOISA beamline at the Elettra Synchrotron*. Review of Scientific Instruments 70, 3855, 1999.
21. P. Gregory, *J. Porphyr. and Phthalocyanines*, 4, 432–437, 2000.

- 22 B. O'Regan and M. Grätzel. *A low-cost, high-efficiency solar cell based on dye-sensitized colloidal TiO₂ films*. Nature, 353(6346):737–740, 1991
- 23 W. Auwärter, D. Eciya, F. Klappenberger and J.V. Barth, *Porphyrins at interfaces*. Nat. Chem., 7, 105-120, 2015.
- 24 C. Wang, Q. Fan, S. Hu, H. Ju, X. Feng, Y. Han, H. Pan, J. Zhu and J. M. Gottfried, *Coordination reaction between tetraphenylporphyrin and nickel on a TiO₂ (110) surface*, Chem. Commun, 50, 8291, 2014
- 25 G. Mattioli, F. Filippone, P. Giannozzi, R. Caminiti and A. A. Bonapasta, *Ab initio Theoretical Investigation of Phtalocyanine-Semiconductor Hybrid Systems*, Chem. Mater., 21, 4555, 2009.
- 26 L. Kavan, M. Grätzel, S.E. Gilbert, C. Klemenz, H.J. Scheel, *Electrochemical and Photoelectrochemical Investigation of Single-Crystal Anatase*, J. Am. Chem. Soc. 118, 6716, 1996.
- 27 B. O'Regan and M. Grätzel. *A low-cost, high-efficiency solar cell based on dye-sensitized colloidal TiO₂ films*. Nature, 353(6346):737–740, 1991.
- 28 U. Diebold, M. Li, O. Dulub, E.L.D. Hebenstreit, W. Hebenstreit, *The relationship between bulk and surface properties of rutile TiO₂(110)*, Surf. Rev. Lett. 7, 613, 2000.
- 29 K. Hashimoto, H. Irie, and A. Fujishima. *TiO₂ photo-catalysis: a historical overview and future prospects*. Japanese journal of applied physics, 44(12R):8269, 2005.
- 30 U. Diebold. *The surface science of titanium dioxide*. Surface science reports, 48(5):53–229, 2003.
- 31 M. Lazzeri, A. Vittadini, A. Selloni. *Effect of Isotopic Substitution on Elementary Processes in Dye-Sensitized Solar Cells: Deuterated Amino-Phenyl Acid Dyes on TiO₂*, Phys. Rev. B 63, 155409/1, 2001.

- 32 R. Lindsay, A. Wander, A. Ernst, B. Montanari, G. Thornton, and N.M. Harrison. *Revisiting the surface structure of TiO_2 (110): a quantitative low-energy electron diffraction study*. Physical review letters, 94(24):246102, 2005.
- 33 H. Onishi and Y. Iwasawa. *Reconstruction of TiO_2 (110) surface: STM study with atomic-scale resolution*. Surface science, 313(1):L783–L789, 1994.
- 34 R. L. Kurtz, R. Stock Bauer, T. E. Msdey, E. Román, and J. L. de Segovia. *Synchrotron radiation studies of H_2O adsorption on TiO_2 (110)*. Surface Science, 218(1):178–200, 1989.
- 35 R.A. Bennett, P. Stone, N.J. Price, and M. Bowker. *Two (1×2) reconstructions of TiO_2 (110): surface rearrangement and reactivity studied using elevated temperature scanning tunneling microscopy*. Physical review letters, 82(19):3831, 1999.
- 36 C. L. Pang, R. Lindsay, and G. Thornton. *Chemical reactions on rutile TiO_2 (110)*. Chemical Society Reviews, 37(10):2328–2353, 2008.
- 37 Mo, L.-B.; Wang, Y.; Bai, Y.; Xiang, Q.-Y.; Li, Q.; Yao, W.-Q.; Wang, J.-O.; Ibrahim, K.; Wang, H.-H.; Wan, C.-H.; Cao, J.-L. *Hydrogen impurity defects in rutile TiO_2* . Sci. Rep. 5, 17634, 2015.
- 38 C. Wang, Q. Fan, S. Hu, H. Ju, X. Feng, Y. Han, H. Pan, J. Zhu, J.M. Gottfried, *Coordination reaction between tetraphenylporphyrin and nickel on a TiO_2 (110) surface*. Chem. Commun. 50, 8291-8294, 2014.
- 39 T. Matsushima, H. Murata, *Enhanced charge-carrier injection caused by molecular orientation*, Appl. Phys. Lett., 98, 253307, 2011.
- 40 R. Gonzalez-Moreno, C. Sanchez-Sanchez, M. Trelka, R. Otero, A. Cossaro, A. Verdini, L. Floreano, M. Ruiz-Bermejo, A. Garcia-Lekue, J. A. Martin-Gago and C. Rogero, *Following the metalation process of protoporphyrin IX with metal substrate atoms at room temperature*, J. Phys. Chem. C, 115, 6849, 2011.

- 41 M. Röckert; M. Franke; Q. Tariq; S. Ditze; M. Stark; P. Uffinger; D. Wechsler; U. Singh; J. Xiao; H. Marbach; H.P. Steinrück; O. Lytken. *Coverage and temperature dependent metalation and dehydrogenation of tetraphenyl porphyrin on Cu(111)*. Chem. Eur. J., 20, 8948–8953, 2014.
- 42 G. Lovat, D. Forrer, M. Abadia, M. Dominguez, M. Casarin, C. Rogero, A. Vittadini and L. Floreano, *Hydrogen capture by porphyrins at the TiO₂(110) surface*, Phys. Chem. Chem. Phys., 17, 30119, 2015.
43. J. Nowakowski, J.;Wäckerlin,C.;Girovsky,J.;Siewert,D.;Jung,657 T. A.; Ballav, N. *Porphyrin metalation providing an example of a redox reaction facilitated by a surface reconstruction*. Chem. Commun. 49, 2347–2349, 2013.
44. A. Verdini; P. Shinde; G.L. Montanari; S.T. Suran-Brunelli; M. Caputo; G. Di Santo; C.A. Pignedoli; L. Floreano; D. Passerone; A. Goldoni. *Water formation for the metalation of porphyrin molecules on oxidized Cu(111)*. Chem. Eur. J., 22, 14672–14677, 2016.
45. W. Auwärter, K. Seufert, F. Bischoff, D. Eciija, S. Vijayaraghavan, S. Joshi, F. Klappenberger, N. Samudrala and J. V. Barth, *A surface-anchored molecular four-level conductance switch based on single proton transfer*, Nat. Nanotechnol., 7, 41, 2012.
- 46 M. Röckert, M. Franke, Q. Tariq, D. Lungerich, N. Jux, M. Stark, A. Kaftan, S. Ditze, H. Marbach, M. Laurin, J. Libuda, H.-P. Steinrück, and O. Lytken, *Insights in Reaction Mechanistics: Isotopic Exchange during the Metalation of Deuterated Tetraphenyl-21,23D-porphyrin on Cu(111)*. J. Phys. Chem. C, 118, 26729-26736, 2014.
- 47 K. Yang, L. Liu, L. Zhang, W. Xiao, X. Fei, H. Chen, S. Du, K.-H. Ernst and H.-J. Gao, *Reversible Achiral-to-chiral switching of single Mn-Phthalocyanine molecules by thermal Hydrogenation and Inelastic Electron Tunneling Dehydrogenation*, ACS Nano, 8, 2246, 2014.
49. J. Schneider, M. Franke, M. Gurrath, M. Röckert, T. Berger, J. Bernardi, B. Meyer, H.-P. Steinrück, O. Lytken, O. Diwald, *Porphyrin Metalation at MgO Surfaces: A Spectroscopic*

and Quantum Mechanical Study on Complementary Model Systems. Chem. Eur. J., 22, 1744, 2016.

50 P. Borghetti, G. Di Santo, C. Castellarin-Cudia, M. Fanetti, L. Sangaletti, E. Magnano, F. Bondino and A. Goldoni, *Adsorption geometry, conformation, and electronic structure of 2H-octaethylporphyrin on Ag (111) and Fe metalation in ultra high vacuum*, J. Chem. Phys., 138, 144702, 2013.

51. P. Palmgren, Baskar Rao Priya, NPP Niraj, and Mats Göthelid. *Bonding of metal-free phthalocyanine to TiO₂ (110) single crystal*. Solar energy materials and solar cells, 90(20):3602–3613, 2006.

52. O. W. Johnson, J. DeFord and J. W. Shaner, J. Appl. Phys., 44, 3008, 1973; (b) O. W. Johnson, S.-H. Paek and J. DeFord, J. Appl. Phys., 46, 1026, 1975; (c) Y. Chen, R. Gonzalez and K. L. Tsang, Phys. Rev. Lett., 53, 1077, 1984; (d) P. M. Kowalski, B. Meyer and D. Marx, Phys. Rev. B: Condens. Matter Mater. Phys., 79, 115410, 2009.

53 X.-L. Yin, M. Calatayud, H. Qiu, Y. Wang, A. Birkner, C. Minot and Ch. Wöll, *Diffusion versus Desorption: Complex behaviour of H atoms on an Oxide Surface*, ChemPhysChem, 9, 253, 2008.

54 L. E. Walle, A. Borg, P. Uvdal and A. Sandell, *Experimental evidence for mixed dissociative and molecular adsorption of water on a rutile TiO₂ (110) surface without oxygen vacancies*, Phys. Rev. B: Condens. Matter Mater. Phys., 80, 235436, 2009.

55 J. Stoehr and D. A. Outka. *Determination of molecular orientations on surfaces from the angular dependence of near-edge x-ray- absorption fine-structure spectra*. Phys. Rev. B, 36:7891–7905, 1987.

56 C. Castellarin Cudia, P. Vilmercati, R. Larciprete, C. Cepek, G. Zampieri, L. Sangaletti, S. Pagliara, A. Verdini, A. Cossaro, L. Floreano, et al. *Electronic structure and molecular orientation of a zn-tetra-phenyl porphyrin multilayer on Si (111)*. Surface science, 600(18):4013–4017, 2006.

- 57 W. Auwaerter, K. Seufert, F. Klappenberger, J. Reichert, A. Weber- Bargioni, A. Verdini, D. Cvetko, M. Dell'Angela, L. Floreano, A. Cossaro, G. Bavdek, A. Morgante, A. P. Seitsonen, and J. V. Barth. *Site-specific electronic and geometric interface structure of co-tetraphenyl-porphyrin layers on Ag(111)*. Phys. Rev. B, 81:245403, 2010.
58. S. J. Silvers and A. Tulinsky. *The crystal and molecular structure of triclinic tetraphenylporphyrin*. Journal of the American Chemical Society, 89(13):3331–3337, 1967.
- 59 P. Borghetti, G. Di Santo, C. Castellarin-Cudia, M. Fanetti, L. Sangaletti, E. Magnano, F. Bondino and A. Goldoni, *Adsorption geometry, conformation, and electronic structure of 2H-octaethylporphyrin on Ag (111) and Fe metalation in ultra high vacuum*, J. Chem. Phys., 138, 144702, 2013.
60. W. Auwärter, K. Seufert, F. Bischoff, D. Eciija, S. Vijayaraghavan, S. Joshi, F. Klappenberger, N. Samudrala, and J. V. Barth. *A surface-anchored molecular fourlevel conductance switch based on single proton transfer*. Nature nanotechnology, 7(1):41–46, 2012.
61. G. Di Santo, S. Blankenburg, C. Castellarin Cudia, M. Fanetti, P. Borghetti, L. Sangaletti, L. Floreano, A. Verdini, E. Magnano, F. Bondino, et al. *Supramolecular engineering through temperature-induced chemical modification of 2H-Tetraphenylporphyrin on Ag (111): Flat phenyl conformation and possible dehydrogenation reactions*. Chemistry-A European Journal, 17(51):14354–14359, 2011.
- 62 F. Buchner, K. Comanici, N. Jux, H.-P. Steinrück, H. Marbach, *Polymorphism of Porphyrin Molecules on Ag(111) and How to Weave a rigid monolayer*, J. Phys. Chem. C, 111, 13531–13538, 2007.
63. P. Giannozzi, et al., *QUANTUM ESPRESSO: a modular and open-source software project for quantum simulations of materials*, J. Phys.: Condens. Matter, 21, 395502, 2009.
64. J. Perdew, K. Burke and M. Enzerhof, *Generalized gradient approximation made simple*, Phys. Rev. Lett., 77, 3865, 1996.

65. S. Grimme, *Semiempirical GGA-type density functional constructed with a long-range dispersion correction*, J. Comput. Chem., 27, 1787, 2006.
66. V. Barone, M. Casarin, D. Forrer, M. Pavone, M. Sami and A. Vittadini, *Role and effective treatment of dispersive forces in materials: Polyethylene and graphite crystals as test cases*, J. Comput. Chem., 30, 934, 2009.
67. P. Palmgren, B. R. Priya, N. P. P. Niraj and M. Gothelid, *Bonding of metal-free phthalocyanine to TiO₂ (110) single crystal*, Sol. Energy Mater. Sol. Cells, 90, 3602, 2006.
68. P. Palmgren, K. Nilson, S. Yu, F. Hennies, T. Angot, C. I. Nlebedim, J.-M. Layet, G. Le Lay and M. Gothelid, *Strong interactions in dye-sensitized interfaces*, J. Phys. Chem. C, 112, 5972, 2008.
69. A. Rienzo, L. C. Mayor, G. Magnano, C. J. Satterley, E. Ataman, J. Schnadt, K. Schulte and J. N. O'Shea, *X-ray absorption and photoemission spectroscopy of zinc protoporphyrin adsorbed on rutile TiO₂ (110) prepared by in situ electrospray deposition*, J. Chem. Phys., 132, 084703, 2010.
70. C. Adamo and V. Barone, *Toward reliable density functional methods without adjustable parameters: The PBE0 model*, J. Chem. Phys., 110, 6158, 1999.
71. Amsterdam Density Functional v. 2014 <http://www.scm.com/ADF>.
72. E. van Lenthe, E. J. Baerends and J. G. Snijders, *Relativistic regular two-component Hamiltonians*, J. Chem. Phys., 99, 4597, 1993.
73. E. van Lenthe, E. J. Baerends and J. G. Snijders, *Relativistic total energy using approximations*, J. Chem. Phys., 101, 9783, 1994.
74. C. Wang, Q. Fan, Y. Han, J. I. Martinez, J. A. Martin-Gago, W. Wang, H. Ju, J. M. Gottfried and J. Zhu, *Metalation of tetraphenylporphyrin with nickel on a TiO₂ (110)-1x2 surface*, Nanoscale, 8, 1123–1132, 2016.

- 75 R. Pawlak, A. Sadeghi, R. Jöhr, A. Hinaut, T. Meier, S. Kawai, L. Zajac, P. Olszowski, S. Godlewski, B. Such, T. Glatzel, S. Goedecker, M. Szymonśki and E. Meyer, *Hydroxyl-induced partial charge states of single porphyrins on Titania Rutile*, J. Phys. Chem. C, 121, 3607–3614, 2017.
- 76 Y. Gurdal, S. Lubner, J. Hutter and M. Iannuzzi, *Non-innocent adsorption of Co-Porphyrin on rutile (110)*, Phys. Chem. Chem. Phys., 17, 22846–22854, 2015.
- 77 S Kera, MB Casu, A Schödl, Th Schmidt, D Batchelor, E Rühl, and E Umbach. *High-resolution inner-shell excitation spectroscopy of H2-phthalocyanine*. The Journal of chemical physics, 125(1):014705, 2006.
78. M. V. Nardi, F. Detto, L. Aversa, R. Verucchi, G. Salviati, S. Iannotta, and M. Casarin. *Electronic properties of Cupc and H2pc: an experimental and theoretical study*. Physical Chemistry Chemical Physics, 15(31):12864–12881, 2013.
79. O. V. Molodtsova, M. Knupfer, Yu. A. Ossipyan, and V. Yu. Aristov. *Molecular orientation and ordering in copc and fepc thin films grown on Au(001)-5x20*. Journal of Applied Physics, 104(8), 2008.
80. M. Fanetti, A. Calzolari, P. Vilmercati, C. Castellarin-Cudia, P. Borghetti, G. Di Santo, L. Floreano, A. Verdini, A. Cossaro, I. Vobornik, E. Annese, F. Bondino, S. Fabris, and A. Goldoni. *Structure and molecule–substrate interaction in a Co-octaethyl porphyrin monolayer on the Ag(110) surface*. The Journal of Physical Chemistry C, 115(23):11560–11568, 2011.
81. T. C. Dinadayalane and G. N. Sastry, *Isolated pentagon rule in buckybowls: a computational study on thermodynamic stabilities and bowl-to-bowl inversion barriers*. Tetrahedron 59, 8347–8351, 2003.
82. Q. Xie, E. Perez-Cordero, L. Echegoyen, *Electrochemical detection of C606- and C706- : Enhanced stability of fullerides in solution*, J. Am. Chem. Soc., 114(10), 3978–3980, 1992.

83. H. W. Kroto, J.R. Heath, S. C. O'Brien, R.F. Curl, and R. E. Smalley, *C₆₀: Buckminsterfullerene*. Nature 318, 162–163, 1985.
84. D. Chirvase, Z. Chiguvare, M. Knipper, J. Parisi, V. Dyakonov, and J.C. Hummelen, *Temperature dependent characteristics of poly(3 hexylthiophene)-fullerene based heterojunction organic solar cells*. J. Appl. Phys. 93, 3376–3383, 2003.
85. N. S. Sariciftci, *Role of Buckminsterfullerene, C₆₀, in organic photoelectric devices*, Prog. Quantum Electron. 19, 131 1995
86. E. I. Altman and R. J. Colton. *Nucleation, growth, and structure of fullerene films on Au (111)*. Surface Science, 279(1-2):49–67, 1992.
87. D.G. de Oteyza, J.M. Garcia-Lastra, M. Corso, B.P. Doyle, L. Floreano, A. Morgante, Y. Wakayama, A. Rubio, J.E. Ortega, *Customized electronic coupling in self-assembled Donor-Acceptor Nanostructures*, Adv. Func. Mat. 19, 3567, 2009.
88. A. El-Sayed, D.J. Mowbray, J.M. Garcia-Lastra, C. Rogero, E. Goiri, P. Borghetti, A. Turak, B.P. Doyle, M. Dell'Angela, L. Floreano, Y. Wakayama, A. Rubio, J.E. Ortega, D.G. de Oteyza, *Supramolecular environment-dependent electronic properties of metal-organic interfaces*, J. Phys. Chem. C 116, 4780, 2012.
89. C. Herring and M. H. Nichols, *Thermionic emission*, Rev. Mod. Phys. 21, 185, 1949.
90. M. G. Helander, M. T. Greiner, Z. B. Wang, and Z. H. Lu, *Effect of electrostatic screening on apparent shifts in photoemission spectra near metal/organic interfaces* Phys. Rev. B, 81, 153308, 2010
91. V. Lanzilotto, G. Lovat, G. Fratesi, G. Bavdek, G. P. Brivio, and Luca Floreano, *TiO₂(110) Charge Donation to an Extended π -Conjugated Molecule*, J. Phys. Chem. Lett., 6 (2), 308–313, 2015.

92. S. Rangan, A. Batarseh, K. P. Chitre, A. Kopecky, E. Galoppini, and R. A. Bartynski *Tuning Energy Level Alignment at Organic/Semiconductor Interfaces Using a Built-In Dipole in Chromophore–Bridge–Anchor Compounds*, J. Phys. Chem C 118(24):12923–12928, 2014.

ACKNOWLEDGMENTS

I wish to thank my tutor Dr. Luca Floreano for his constant support, helpful advises and patience and the nice running moments together. I am also grateful to the University of Trieste, specially to my supervisor Prof. Alberto Morgante and doctorate school director Prof. Lucia Pasquato for the opportunity to work on this field and academic guidance.

I thank all the people in the lab and around at ELETTRA, Dr. Albano Cossaro, Dr. Alberto Verdini, Prof. Dean Cvetko, Dr Gregor Kaldnik, Dr. Gregor Bavdek, Dr. Carla Castellarin Cudia, Dr. Giovanni Di Santo and Dr. Martina Dell'Angela, for their direct support to my work and helpful attention.

I am indebted with Dr. Celia Rogero and her coworkers who made available their STM facilities and knowledge about the technique that represented an invaluable resource, and with Prof. José Angel Martín-Gago who made all this possible, for his support and friendship.

I'm especially grateful with my colleges and friends, Dr. Giacomo Lovat and Dr. Shital Vaidya, that have become part of my personal life more than professional and with all my "running friends" Marco, Ivan, Luppieri, Penco and Zupancic.

I wish to mention all the people from Elettra and Trieste that embraced me at Italy and enriched my life, Martina, Jacopo, Christina, Diego, Mirta, Lorenzo, Giacomo, Lyubo, Flavio, Barbara, Eric, Andrea, Stefano, , Cristiano, Feng, May, Nishant, Rafaqat, Valeria, Roberto, Matus, et al.

And last but not least, I would like to dedicate my work to my family and couple, that have been the best support during this period and the pillar of my life.